An atomic marble run to unity phase-space density

Chun-Chia Chen

An atomic marble run to
unity phase-space density

ACADEMISCH PROEFSCHRIFT

ter verkrijging van de graad van doctor
aan de Universiteit van Amsterdam
op gezag van de Rector Magnificus
prof. dr. ir. K. I. J. Maex
ten overstaan van een door het College voor Promoties
ingestelde commissie, in het openbaar te verdedigen in de
Agnietenkapel
op vrijdag 26 April 2019, te 12:00 uur

door

Chun-Chia Chen

geboren te Taichung

Promotion committee

Promotor	prof. dr.	F. E. Schreck	Universiteit van Amsterdam
Co-promotor	dr.	B. B. Pasquiou	Universiteit van Amsterdam
Other members	prof. dr.	J. W. Thomsen	University of Copenhagen
	dr.	M. Zawada	Nicolaus Copernicus University
	prof. dr.	M. S. Golden	Universiteit van Amsterdam
	prof. dr.	D. Bonn	Universiteit van Amsterdam
	dr.	R. Gerritsma	Universiteit van Amsterdam

Faculteit der Natuurwetenschappen, Wiskunde en Informatica (FNWI)

The author can be reached at:
chenchunchia@gmail.com

Contents

iv

Chapter 1

Introduction - An Atomic Marble Run

1.1   Our challenge

In 1960 Maiman invented the first laser [1] and produced for the first time coherent stimulated optical radiation. This laser used a ruby crystal as active medium and operated in pulsed mode. Just a few months later, Donald Herriott, Ali Javan and William Bennett from Bell lab reported a very different kind of laser [2]. They used a mixture of helium and neon as the active medium and produced a "continuous" beam rather than pulses, realizing a continuous-wave (CW) laser. However, even four years after Maiman's experiment, there were still few applications reported using a laser. Some argued that the laser was a "solution searching for a problem". Nowadays we do not need to argue that laser technology has a significant impact on our daily lives because there are plenty of examples for this fact, such as telecommunication through optical fibers and optical clocks. Many ground-breaking works relevant to lasers, including gravitational wave detection, optical tweezers, and intense short bursts of laser light [3, 4, 5], have later been acknowledged by the Nobel committee for their contribution to the scientific research spectrum ranging from very fundamental science to applications. Many of these laser applications arise from the long coherence length of the electromagnetic waves produced by CW lasers.

A fundamental principle of quantum physics is the duality of waves and particles. Therefore an interesting question is to ask if other particles, beyond the photons of electromagnetic waves, can be described by coherent waves. Is it for example possible to create a beam of atoms for which the motion is described by one quantum mechanical matter wave with long coherence length? To what extend can we see the wave nature of matter waves? This question was effectively answered seven decades ago when Satyendra Nath Bose and Albert Einstein predicted that a gas of noninteracting integer-spin particles would condense into a macroscopic

quantum state when cooled below a critical temperature, realizing a Bose-Einstein condensate (BEC). A BEC has similarities to optical laser radiation enclosed in an optical cavity.   Just as in a single-mode optical laser where one mode of the electromagnetic field is populated by photons, a BEC is one matter wave that describes the position and motion of many atoms. By contrast a thermal gas of atoms corresponds in this analogy to the photons emitted by an incandescent light source. Just as a laser beam can be outcoupled from the electromagnetic wave in a laser cavity, coherent outcoupling of atoms from a BEC leads to a coherent propagating matter wave. Such a wave is called an "atom laser".

A BEC of ultracold atoms was first achieved in 1995 [6], which marked a new era for atomic physics. Because of the precision and flexibility with which a condensate can be manipulated, a vast interest in BECs has grown in the communities of atomic physics, quantum optics, and many-body physics [7]. Two years after the first BEC of ultracold atoms, the first out-coupling of atoms from a condensate was demonstrated, forming an atom laser.   However, even 20 years after its birth, no BEC has been realized in the steady state, nor was a CW atom laser created. Overcoming these related challenges is the main goal of our research and the work presented in this thesis makes a large step towards that goal.

1.2   State of the art

For a gas of bosonic atoms with number density n and temperature T, the phase transition to quantum-degeneracy occurs if its phase-space density (PSD) $\rho = n\lambda_{\mathrm{dB}}^3$ exceeds a value of 2.612.   Here $\lambda_{\mathrm{dB}} = h/(2\pi m k_B T)^{1/2}$ is the thermal de Broglie wavelength, which represents the position uncertainty associated with the thermal momentum distribution, where h is Planck's constant, m is atomic mass and k_B Boltzmann's constant. From the perspective of energy eigenstates, Bose-condensed atoms would all occupy the same single-particle ground-state wavefunction. From a wave nature of particles perspective, it is a state where the thermal de-Broglie wavelength is comparable to the interatomic separation and matter needs to be described by one wave function. The atoms become indistinguishable and behave macroscopically in the same way.

Today, most atomic Bose-Einstein condensates are routinely realized with one, standard experimental method. This method consists of two cooling stages that are executed time-sequentially.   First laser cooling, then evaporative cooling.   Laser
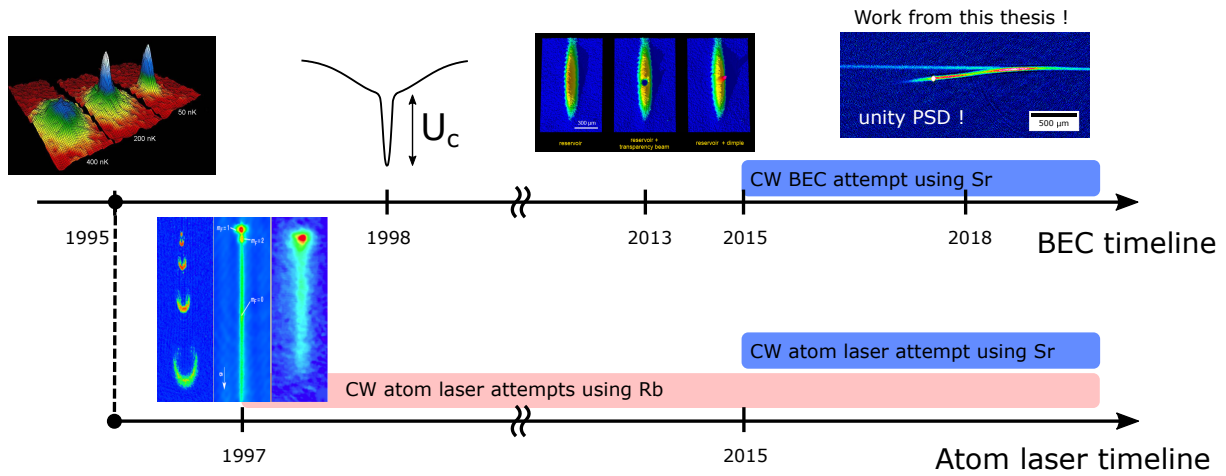
FIGURE 1.1: **Laser cooling to Bose-Einstein condensation (BEC) timeline.** The first BEC experiment succeeded at JILA back in 1995 [6]. The first atom laser is demonstrated in 1997 [8, 9]. One year after, it had been shown that formation of a BEC can be achieved by trap deformation [10]. In 2013, almost two decades after the first BEC, a Sr BEC is produced by using only laser cooling to remove the entropy of the gas [11]. The experiment relies on the advantages of the narrow-linewidth laser cooling transition of Sr and the spatial protection of atoms from the near resonant photons. All previously demonstrated experiments mark the critical ingredients leading towards the goal of this project, a steady-state BEC. In 2017 an alternative approach for laser cooling to a condensate was implemented for Rb, using repeated optical lattice compression followed by Raman sideband cooling (not shown in figure) [12].

cooling can bring the atom's temperature down via exchange of momentum with laser cooling photons. Various laser cooling schemes have been developed [13, 14, 15] to lower the temperature even below the momentum of one photon. Evaporative cooling relies on removing the high energy fraction of the atoms from the atomic sample and letting the atoms re-thermalize through elastic collisions. This method can achieve temperatures that are even lower than the ones achievable by laser cooling. Both steps are often time-consuming and the latter typically leads to substantial atom loss.

Thirteen elements were cooled to quantum degeneracy by a laser cooling stage followed by an evaporative cooling stage. This method is executed every day many times in hundreds of labs around the world and has proven robust. However, the two cooling steps favor different experimental conditions and are incompatible with each other. The reason is that during evaporative cooling, any near-resonant photons that scatter with the atoms will heat them and prevent evaporative cooling to achieve low temperatures. Therefore, these two cooling steps are incompatible and are usually performed one after the other in time. Many scientists have for many years continued

to try to answer whether it is possible to produce a quantum gas by only using laser cooling to remove the entropy from the gas [16, 17, 18, 19, 20]. From the experimental point of view, bypassing the time consuming evaporative cooling step can vastly expedite the quantum gas experiment and also avoid the atom losses due to the inefficient cooling process, thus making quantum gas production faster and delivering higher flux. From the point of view of practical laser applications, the incompatibility of the two cooling steps makes it hard to produce quantum gases in a continuous fashion. Limited to pulsed operation, the sacrifice of matter-wave coherence is of immediate concern.

Removing all entropy from the gas by laser cooling alone in order to reach quantum degeneracy remained a long-awaited holy grail within the atomic physics community ever since the early days, when achieving a Bose-Einstein condensate was still a heated competition among many different groups [6, 21, 22, 23]. This goal has been elusive, and the question remained open until 2013, when our group firstly demonstrated a laser cooling to BEC scheme when we were still in Innsbruck [11]. This experiment is based on the fact that the Doppler temperature is very low in elements with narrow-linewidth transitions [24, 25, 26, 27]. In strontium, the $^1S_0$ - $^3P_1$ transition has a linewidth of 7.4 kHz, which translates to a Doppler temperature of 180 nK and a recoil temperature of 460 nK. This is in contrast to the usual MHz-linewidth cooling transitions for which the Doppler temperature is around 100 μK. A kHz-linewidth transition sits at a sweet spot for laser cooling. After pre-cooling to the mK regime on a MHz-linewidth transition, it can continue to cool a cloud to the sub-μK regime. Its Doppler temperature is also comparable to the phase transition temperature at cloud densities that are not too high, i.e. not limiting the experiments by three-body loss. This allows us to achieve ultra-low temperatures and high phase-space density. Narrow-linewidth cooling in Sr has first shown its power in the work of Katori's group [24]. By employing a far-off resonance optical dipole trap (FORT) that allows in-trap Doppler cooling, the group demonstrated laser cooling to a PSD exceeding 0.1 and a temperature of $\sim$ 500 nK. This means cooling an atomic cloud to a temperature below the critical temperature can be achieved by removing the entropy using solely laser cooling instead of combining laser and evaporative cooling.

Apart from the method demonstrated with Sr, Raman sideband cooling is another approach to high PSD pursued within Steven Chu's academic tree for years [13, 28]. In 2002, the group at the University of California, Berkeley, led by David Weiss already

demonstrated a time-sequential laser cooling experiment and attained a phase-space density of ∼1/30, ultimately limited by three-body decay. After David Weiss's work, using Raman sideband cooling to attain BEC was further pursued and finally brought to success in 2018 by a group of researchers led by Vladan Vuletic at MIT [12], showing another laser cooling to BEC scheme different from the Sr work.

1.3   Laser cooling to BEC scheme using Sr

In order to produce a CW atom laser we need new methods to get around the incompatibility of laser cooling and evaporative cooling, beyond the standard method of executing one cooling stage after the other in time. In Innsbruck's laser cooling to BEC experiment, see Fig. 1.2, a Sr sample is pre-cooled on a 30 MHz linewidth laser cooling transition, further cooled on a 7.4 kHz linewidth transition and transferred into the dipole trap. Most atoms reside in the large-volume "reservoir" part of the dipole trap, where they are continuously laser cooled on the narrow-linewidth transition, reaching a temperature of 900 nK and a phase-space density of 0.1. In the center of the reservoir a deep and narrow dimple dipole trap is added. The dimple locally increases the cloud density. The temperature of the cloud however stays the same everywhere because of thermalization by elastic collisions. BEC can be reached when switching all laser cooling light off. If it remains on, the fluorescence light from laser cooled atoms will scatter off BEC atoms, quickly leading to loss of the BEC.

In order to achieve a BEC in presence of laser cooling, a transparency beam introduces a light shift on the $5s5p\,^3\mathrm{P}_1$ state , the optically excited state of the laser cooling transition, see Fig. 1.2(a). By shifting the excited state energy level of the atoms within the volume of the transparency beam, we can engineer a cooling scheme where narrow-linewidth laser cooling light only interacts with the atoms in the reservoir outside of the transparency region. Atoms within the transparency beam covered region become off-resonant to the fluorescence photons, thus overcoming the unfavorable photon scattering effect on the high density, ultracold atoms in the dimple trap. Atoms within the transparency beam region are thermalized by elastic collisions with atoms outside of that region. Under these conditions, the entropy removal from the gas is done using only laser cooling and atoms within the dimple trap are in thermal contact with the laser cooled cloud during the entropy removal process. The thermalization between the atoms in the dimple and those in the reservoir leads to cooling of atoms inside the dimple, and leads to condensation. It

(a)   (b)
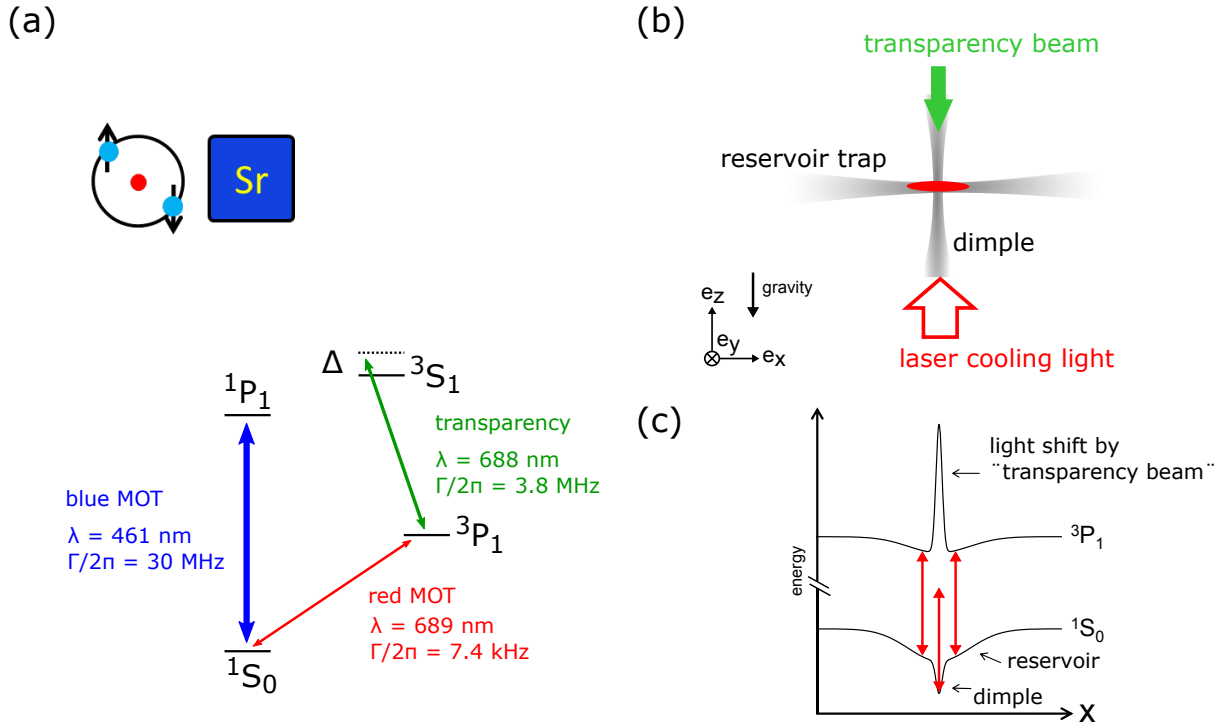
FIGURE 1.2: **Laser cooling to BEC scheme [11].** (a) Scheme of relevant Sr terms and transitions. The blue-MOT transition is $30\,$MHz wide and can efficiently slow atomic beams and cool atoms to $1\,$mK. The red-MOT transition is an intercombination transition between singlet and triplet states. It has a linewidth of only $7.4\,$kHz, which allows laser cooling to temperatures below $1\,\mu$K. The Doppler cooling limit for this transition is $180\,$nK. Such narrow-linewidth cooling easily bridges the mK cold cloud temperature of the "blue MOT" to the μK regime. Combining both the broad-linewidth and kHz-linewidth transition, it allows us to achieve sub-μK temperatures in a two-step cooling process. A laser beam that is blue detuned to the $^3P_1$ - $^3S_1$ "transparancy" transition causes a light shift of the $^3P_1$ state. (b) A reservoir trap in the horizontal plane is crossed by a vertically oriented, smaller dimple beam. A laser beam blue detuned to the transparency transition, called "transparency beam", is overlapped with the dimple and acts like an invisibility cloak, protecting atoms from the unfavorable scattering of near-resonant photons. (c) Potential landscape experienced by ground state atoms ($^1S_0$) and atoms in the optically excited state of the laser cooling transition ($^3P_1$). The ground state is light shifted due to the reservoir and dimple dipole traps. The excited state is light shifted by those beams and the transparency laser, see Sec. 2.3.4. Laser cooling light is able to excite atoms in the reservoir region whereas atoms in the dimple are shifted out of resonance with laser cooling photons by the transparency beam light shift.

TABLE 1.1: **Atomic cloud characteristics at different stages in a typical BEC experiment [29].** Values given here are only indicative and can differ by orders of magnitude in dependence of the atomic species used. In each cooling stage, the ground state population increases by typically 10^6, see phase-space density column.

Step	Temperature	Density (cm^{-3})	Phase-space density
Oven	500 K	10^{14}	10^{-13}
Laser cooling	50 μK	10^{11}	10^{-6}
Evaporative cooling	500 nK	10^{14}	> 1

was shown that the time scale of condensate formation is just $\sim 100\,\text{ms}$. It was also shown that a repeated condensation process, triggered by repeatedly removing the BEC from the dimple, lasted for multiple cycles, mainly limited by the atom number available within the reservoir.

1.4 Extension towards a steady-state BEC

For a pulsed experiment, the advantages provided by the properties of Sr can be exploited sequentially in time, and can thus achieve the desired conditions, i.e., low temperature and high PSD. This method is also the usual recipe in many quantum gas experiments. However, in pursuit of a steady-state quantum gas machine, a stream of atoms exiting an oven at a temperature of a few hundred Kelvin starts with a phase-space density of $\sim 10^{-13}$, see Tab. 1.1. All cooling steps now need to take place at the same time, and there is a 13 orders of magnitude gap between the starting condition (oven) and the targeted phase-space density ($\sim$2.6) where the phase transition occur. An important aspect of our laser cooling to BEC experiment is that it changed people's perception of what is required to achieve BEC. The evaporative cooling step that is usually time-sequentially implemented after the laser cooling step is no longer regarded as a necessary step. Using our new technique as a stepping stone, we can now envision the possibility of realizing a truly perpetual BEC and atom laser.

Continuous atom laser attempts so far only have been pursued using Rb and Cr. For Rb, the main laser cooling transition at $780\,\text{nm}$ has a Doppler temperature of $146\,\mu$K. Due to the incompatibility of a BEC with near-resonant photons, further entropy reduction relies on an evaporative cooling process, which was carried out within a magnetic guide [30]. After the laser cooling stage and loading of atoms into
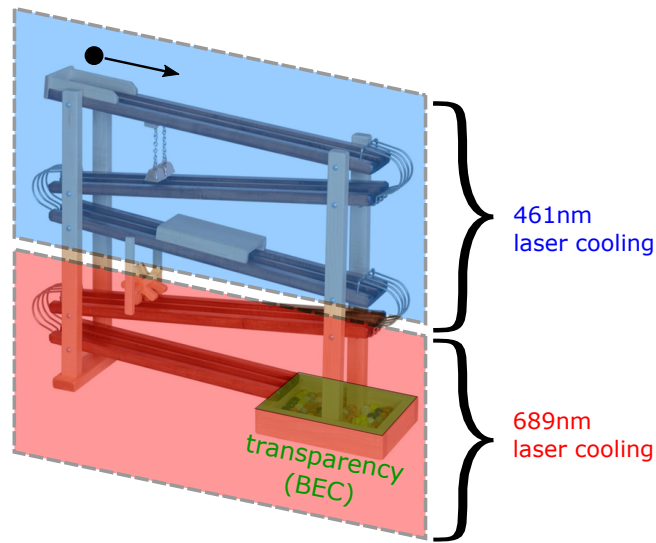
FIGURE 1.3: **Atomic marble run machine: expanding the Sr laser cooling to BEC experiment into a steady-state system.** Philosophy of the atomic marble run experiment. Cooling steps using transitions with different cooling temperature limits are implemented sequentially in space.

the magnetic guide, the atomic cloud still has 8 orders of magnitude lower phase-space density than needed for reaching quantum degeneracy. Therefore, experimentally we benefit little from the laser cooling properties of Rb. Unlike the 6-MHz wide Rb laser cooling transition, the Sr narrow-linewidth laser cooling transition has great laser cooling properties, with a Doppler temperature of 180 nK. For Cr, it has been shown that a magnetically guided atomic beam continuously loaded into a dipole trap at the end of the magnetic guide can reach a PSD of 10^{-4} [31, 32], ultimately establishing the highest steady-state PSD ever achieved before this thesis.

In the 2013 laser cooling to BEC experiment, we show that the transparency beam protects the BEC from the near-resonant fluorescence photons while the BEC is in thermal contact with the laser cooled reservoir. To make a continuous atom laser by outcoupling atoms from the BEC within the transparency beam protection region, eventually we will encounter BEC atom depletion. However, refilling atoms is possible since the BEC is in contact with the laser cooled reservoir. Since this is a dissipative reservoir, new atoms can be inserted by sending an atomic beam on it.

The 2013 laser cooling to BEC experiment has shown a method to get around the incompatibility of laser cooling and evaporative cooling. Refilling atoms into the

reservoir trap is also possible. It makes us hopeful to achieve an atom laser using Sr except for the fact that to realize a truly continuous cooling scheme for a steady-state quantum gas experiment, the narrow-linewidth transition photons are not the only near-resonant photons to appear in our laser cooling scheme, see Fig. 1.2 (a). The dipole-allowed $^1S_0 - {}^1P_1$ transition has a wavelength of 461 nm and a linewidth of 30 MHz. A MHz-linewidth transition is required to slow the fast atoms effusing from the oven and to magneto-optically trap those atoms. It also helps us to collect lots of atoms.

In order to prepare the cloud of atoms in the reservoir, an ultracold ^{84}Sr sample of 9×10^6 atoms at a temperature of 900 nK, it is crucial to pre-cool the atoms on the blue transition before continuing with the red MOT cooling steps.

For the transparency trick, the transparency beam is addressing the excited state involved in the $^1S_0 - {}^3P_1$ narrow-linewidth transition. Therefore this near-resonant light protection mechanism only applies to the red MOT cooling transition, as shown in Fig.1.2. In an ideal continuous cooling scheme for a steady-state quantum gas experiment, all the cooling steps take place at the same time. Therefore we need to protect the quantum gas not only from red MOT photons, but also from blue MOT photons. The transparency beam trick requires us to shift the optically excited state of the cooling transition by many hundred linewidths, which is hardly achievable for the 30-MHz wide blue MOT transition. Our solution to this challenge is to spatially separate the section where we apply cooling steps using the blue MOT transition from the region in which we apply the narrow-linewidth cooling light. Each crucial cooling step is implemented sequentially in space, just like an "atomic marble run", so that atoms are cooled down while they travel along a trajectory starting from the oven towards a destination where a steady-state BEC will exist, see Fig. 1.3.

We now have all the crucial ingredients in hand to achieve the ultimate goals, a steady-state BEC and a steady-state atom laser. The main challenge we have to solve is to continuously refill ultracold atoms into the laser cooled reservoir of the "laser cooling to BEC" experiment. In order to meet this challenge and then to reach our goals we started a new project, called "Sr Perpetual Atom Laser (SrPAL)".

1.5 Scope of this thesis

In this thesis we describe an experimental setup designed for a steady-state BEC and atom laser, realized by preparing a steady-state ultrahigh phase-space density Sr

atomic sample that is protected from near-resonant laser cooling photons by a transparency beam. Within this thesis, we focus on answering the following main research questions.

- Can we implement the two-step laser cooling process sequentially in space instead of sequentially in time, and still achieve a competitive atom source performance?

- Are there new and better laser cooling methods enabled by the electronic level structure of Sr?

- Can we expand the laser cooling to BEC experiment into a steady-state experiment?

This thesis is organized as follows:

In Chapter 2 we present the experimental setup, mainly covering the light sources and the implementation of the experiment. We describe the laser setup of the two main laser cooling wavelengths, 461 nm and 689 nm. We introduce repump laser systems to improve the atomic source flux and to close a loss channel occurring because of the combined action of red MOT cooling light and transparency beam. Repumping removes atoms from the metastable $^3P_0$ and $^3P_2$ states, which are long-lived and dark for laser cooling light, and brings them back into the laser cooling cycle. Furthermore we present the dipole trap and transport guide setup, as an instrumental part of the atomic marble run machine.

In Chapter 3 we present the first step of the atomic marble run machine, the realization of two-step laser cooling (red and blue) sequentially in space. An important ingredient are the techniques used to decelerate an atomic beam and trap the atoms using the 7.4-kHz transition. Finally we benchmark the performance of a steady-state narrow-linewidth magneto-optical trap (MOT), which has a 100-fold better PSD than what has been previously achieved in a MOT.

In Chapter 4 we complete the steady-state architecture for the "laser cooling to BEC" experiment. An ultracold atomic beam source is constructed and a reservoir refilling scheme is developed and characterized. We present results including all steps necessary to continuously load ultracold atoms into a reservoir trap and report a steady-state Sr sample with unity phase-space density, which is a 10000-fold improvement compared to previous work and only a factor of 2.6 away from quantum degeneracy.

In Chapter 5 we get inspired by the cooling scheme theoretically studied by Zoller et al. in 1994 [33] and a similar idea that was proposed for (anti)hydrogen cooling [34], to implement Sisyphus cooling of Sr for the first time. The result points towards a deceleration scheme that may complement the ultracold beam deceleration method already implemented in our machine before the loading of the reservoir trap.

We conclude in Chapter 6 and point out possible future steps with which we hope to obtain a steady-state BEC and an atom laser.

Chapter 2

The steady-state machine

2.1   System overview: atomic marble run architecture

During the planning stage of the SrPAL project, a critical issue on the list of challenges was how to cloak a steady-state BEC from any detrimental near-resonant "blue MOT" laser cooling photons. As was mentioned in the introduction, the reason that we did not implement a "transparency beam" technique to protect the atoms from blue laser cooling photons is that the optically excited state of a laser cooling transition needs to be shifted by many hundred linewidths. This is easily achievable for the 7.4 kHz wide transition, but hardly possible for the 30 MHz wide blue laser cooling transition. We came up with a solution that is different from the transparency beam method. The solution is to spatially separate the blue and red laser cooling stages. The blue laser cooling stage is implemented in the top half section of the vacuum chamber and spatially separated from the rest of the cooling steps that don't involve blue laser cooling light. Therefore the blue laser cooling photons do not disturb the quantum gas. By separating the two cooling processes into two sections of the experiment, we can also have more freedom to optimize our system for high flux, low temperature and high PSD. We use blue laser cooling in the top part to decelerate an atomic beam that is created by the oven. Laser slowing and cooling on the blue transition is crucial to bring the atomic beam of the oven, which has a velocity of hundreds of meters per second to the capture velocity of the narrow-linewidth transition, which is only a few meters per second. To implement this solution we developed a new type of Sr laser cooling apparatus, shown in Fig. 2.1.

My colleague Shayne Bennetts and I have constructed the vacuum setup together. Shayne did most of the vacuum chamber design work. Due to the great overlap of our experimental work, we did split the large amount of material onto our two thesis. Whereas Shayne will describe the details of the vacuum design, I will describe the

details of the laser system. In Sec. 2.2 I only briefly summarize the most crucial points of the vacuum chamber design. Section 2.3 then continues with an extensive description of the laser system.

2.2 Vacuum setup

The path of the Sr atoms through our machine starts in an oven, in which a chunk of Sr metal is heated to about $550\,°C$ to sublimate Sr atoms. The oven section contains the actual oven and differential pumping stages to provide a high pressure gradient. The UHV chamber contains the high-PSD sction and the "blue" laser cooling section excluding the transverse cooling. When designing the experiment, one emphasis is to attain a high-flux atomic beam, because for an atom laser, an important benchmark will be the atom flux available for practical applications. Among all Sr isotopes, ^{84}Sr is of particular interest for realizing a BEC because of the favorable scattering length, $+124\,a_0$. For quantum gas experiments, the scattering properties of the atomic species play an important role because they govern the performance of thermalization, which is crucial to create a BEC. Ironically, ^{84}Sr has the lowest natural abundance of all isotopes, 0.5%. Bearing this emphasis on flux in mind, we choose a large oven nozzle composed of multiple tubes[1] and a 14 mm diameter differential pumping tube.

"Blue" laser cooling section — Sr atoms in the atomic beam are transversally cooled, Zeeman-slowed, and captured in a 2D "blue" magneto-optical trap (MOT) with $461\,nm$ blue light that addresses the $^1S_0$ - $^1P_1$ transition. In contrast to a typical quantum gas machine, we implement a 2D blue MOT instead of a 3D blue MOT. Atoms are radially confined by the 2D blue MOT beams and then continue the journey of cooling and deceleration along the un-confined axis of the 2D blue MOT towards the next cooling stage. Within the blue laser cooling section, unavoidably there will be lots of scattered blue cooling photons. However, since we restrict ourselves to use blue laser cooling only in this section, ideally blue cooling photons are well-confined within the top half section of the chamber. In order to reduce the flux of blue photons to the lower chamber a baffle made of neutral density filters[2] is installed. This baffle acts as a differential pumping section and scattered blue photon dump. In this way we minimize the number of blue photons entering the bottom half section and manage to reduce the residual harmful blue photon scattering events. We thus turn the final

---

[1] An array of ~ 2500 8 mm long microtubes, with $100\,\mu$m inner diameter and $200\,\mu$m outer diameter.
[2] Thorlabs, NE60B-A.
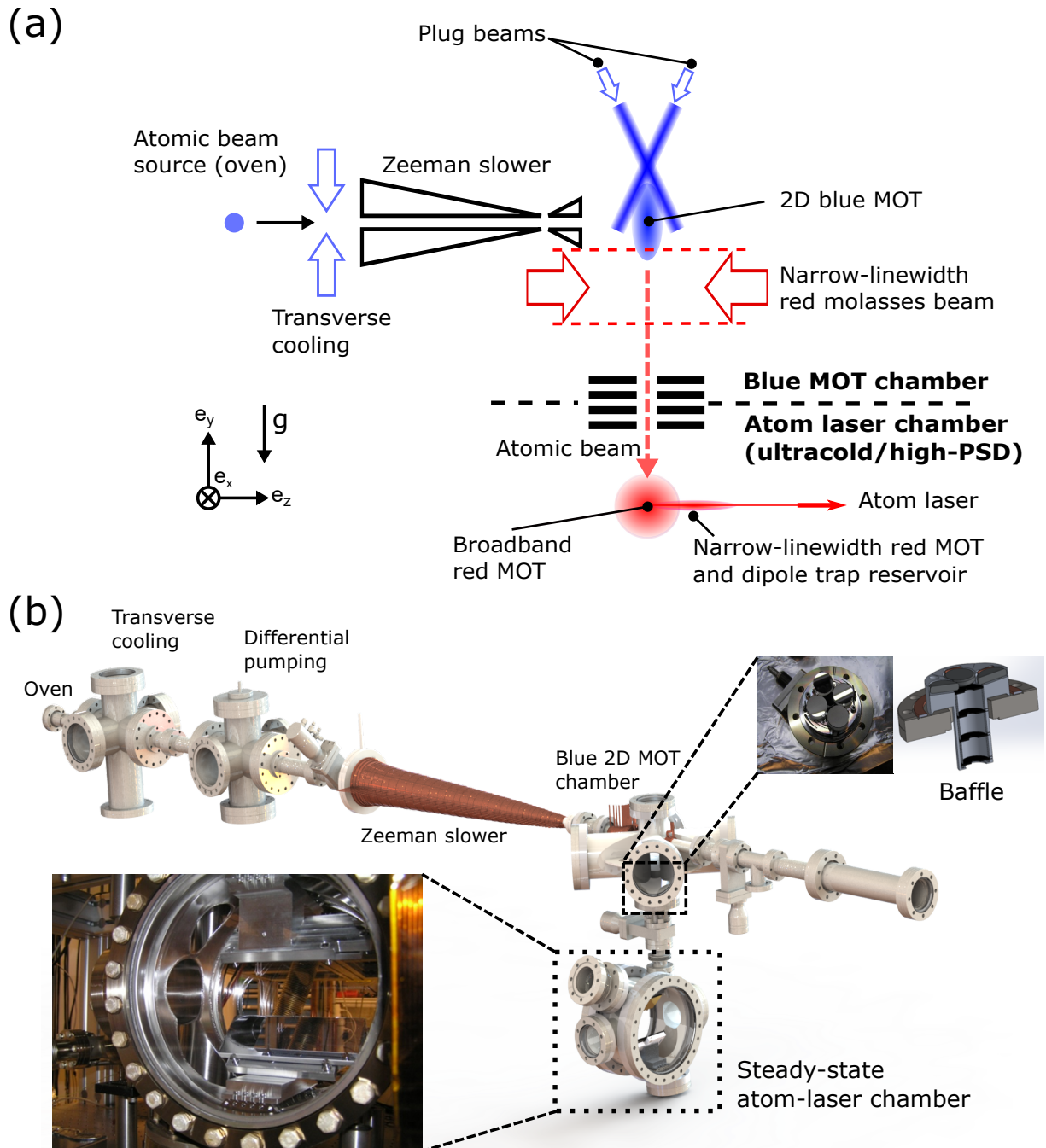
FIGURE 2.1: **Sr perpetual atom laser machine.** (a) Concept of the perpetual atom laser experiment. Different laser cooling steps are implemented sequentially in space. The blue arrows indicate the section where we apply $^1S_0$ - $^1P_1$ cooling light. Atoms exit the high temperature oven, slow down in the Zeeman slower and get captured by a blue 2D MOT. Atoms are then ejected downwards along the unconfined axis. (b) CAD schematic of the vacuum chamber setup.
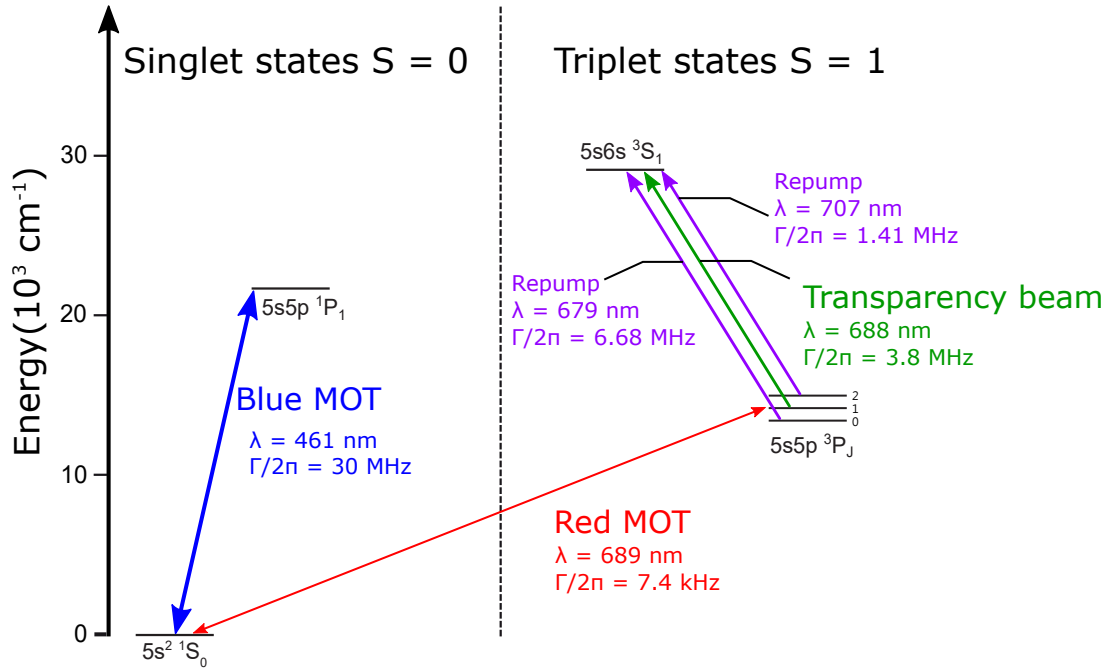
FIGURE 2.2: **Characteristics of different transitions used in the SrPAL experiment.** Schematic of the Sr terms and transitions used for cooling, repumping and the transparency beam of Sr atoms. The blue MOT is operated on the strong $5s^2\,^1\mathrm{S}_0 - 5s5p\,^1\mathrm{P}_1$ transition. The red MOT laser addresses the $5s^2\,^1\mathrm{S}_0$ - $5s5p\,^3\mathrm{P}_1$ intercombination line, used for narrow-line cooling. Three different laser wavelengths addressing transitions from the $5s5p\,^3\mathrm{P}$ manifold to $5s6s\,^3\mathrm{S}_1$ are used for the transparency beam and repumping, repectively.

steady-state atom laser chamber (ultracold, high-PSD section) into a "blue photon free" region, except when taking the absortion imaging pictures.

Ultracold, high-PSD section — Within this section, we exclude the usage of "Blue MOT" laser cooling light. A reservoir dipole trap will be implemented in this chamber. By adding a transparency beam, we can engineer an environment where atoms don't see the 689-nm "red" light, and thus enabling the condensate to exist with the near-resonant light nearby.

2.3 Laser systems

In this section, we describe the SrPAL laser systems we have developed for the experiment. The system is designed to meet the requirements of the SrPAL experiment while also keeping in mind ease of maintenance and flexibility for future experiment upgrades. First, two laser systems generating light addressing the Sr $5s^2\,^1\mathrm{S}_0 - 5s5p\,^1\mathrm{P}_1$ singlet-singlet and $5s^2\,^1\mathrm{S}_0 - 5s5p\,^3\mathrm{P}_1$ singlet-triplet transitions are

described. Secondly, three laser systems addressing transitions from the $5s5p\,^3$P manifold to $5s6s\,^3$S$_1$ are described for applications including repumping of metastable state atoms and implementation of transparency beams.   Both cooling and re-pumping laser wavelengths are depicted in Fig. 2.2. Thirdly, an infrared laser setup used for dipole traps including the atom transport guide, the reservoir trap, and the dimple trap is described.

2.3.1   Blue, 461-nm laser system

We will first discuss the 461-nm laser sources and then describe the experimental implementation of the 461-nm laser setup.

There are two commonly used methods for producing a 461-nm light source for laser cooling Sr on the $5s^2\,^1$S$_0 - 5s5p\,^1$P$_1$ transition. The first is to frequency double 922-nm light and the second is to use 461-nm diode lasers. To obtain the 922-nm light for the first method, two types of laser sources can be used. The first type is $922\,\mathrm{nm}$ light generated by an external cavity diode laser (ECDL) system. The second source of 922-nm light is the semiconductor disk laser (SDL) [35], which has become competitive lately.   This laser technology uses InGaAs/AlGaAs as gain medium whose spectral range is 920$\sim$ 1100 nm, the most mature fabrication range for gain mirror technology. Pumping it with 532 nm light, it emits light at 922 nm.   The advantage of this type of laser is its relatively high power (> 100 mW) without using an additional amplifier, its clean beam profile and its tunability. However this light source is still in the developing phase and not generally used in the cold atom community. Because of the fast-growing interest in quantum technology, especially for atomic optical clocks, this technology will become commercially available and economically competitive regarding price per photon and compactness. The 922-nm light is then frequency doubled to 461 nm by second-harmonic generation (SHG) using a doubling crystal such as KNbO$_3$ [36], BIBO [37], or PPKTP [38]. Single-pass PPLN waveguides can also be used for frequency doubling [39]. Another method is direct generation of 461 nm light using diode lasers. A Nichia laser diode emits 100 mW of light when operating at the nominal current. However, this light is not emitted in a perfect TEM$_{00}$ mode at all [40]. After careful beamshaping and cleaning of the mode with a fiber we are typically left with only $\sim$60 mW. Taking into account that about half of the light will be lost in further optical elements before reaching the atoms, we see that we need about seven Nichia diodes to operate our machine.

When we started the project, we already had a SHG laser system available in the RbSr project of our group [41]. By then, a single frequency diode laser at 461 nm already became commercially available. We decided to build our laser system based on laser diodes purchased from NICHIA[3], and to use the injection locking technique to frequency stabilize these lasers in order to essentially use them as amplifiers. We can choose between two different sources for our reference frequency seeding. The first source is the reference light that is delivered via fiber from the RbSr lab. The second source is a home-made external-cavity diode laser (ECDL) frequency stablized to the strontium atomic transition using a saturated absorption spectroscopy technique. At the beginning we used a light source from the SHG laser system in the RbSr laser setup. We noticed our injection-locked laser system becoming unstable while the SHG laser is being frequency shifted when switching from one Sr isotope to another. In order to avoid this problem we use the frequency stablized ECDL as our reference frequency.

A schematic of the blue laser system is depicted in Fig 2.4 and listed in Tab. 2.1. As explained in the figure legend, different colors are used to highlight different subsections for ease of comparing with the real setup. The different subsections are described in the following.

Master slave branch — This is the first slave laser in the blue laser setup, see Fig. 2.4. It is injection-locked using the reference light that is delivered via fiber from the RbSr lab. There, the reference light source is locked to the abundant ^{88}Sr isotope spectroscopy signal. After reference light is amplified by the first slave, laser light passes through a 350-MHz acousto-optic modulator (AOM) in a double-pass configuration and is coupled into a fiber to clean up its spatial mode[4] before sending the light to the next distributing stage for different applications. This 350-MHz double-pass AOM enables us to tune the light emitted by the master slave for the purpose of isotope selection, see Fig. 2.3.

Seed frequency shifting AOMs — After the isotope selection AOM the light is fiber coupled and sent to a distribution setup where the laser frequency is shifted through various AOM paths in order to seed several slave lasers with different frequencies. The frequency shifts values are depicted in Fig. 2.3. Applications include the seeding source for the 2D MOT lasers, a slave laser for seeding a Zeeman slower

---

[3]NICHIA, http://www.nichia.co.jp/en/about_nichia/index.html

[4]We observe that by adding this cleaning stage between the master slave laser and the following distribution system, we benefit from the better laser spatial mode and achieve better AOM diffraction efficiencies in the following stages.
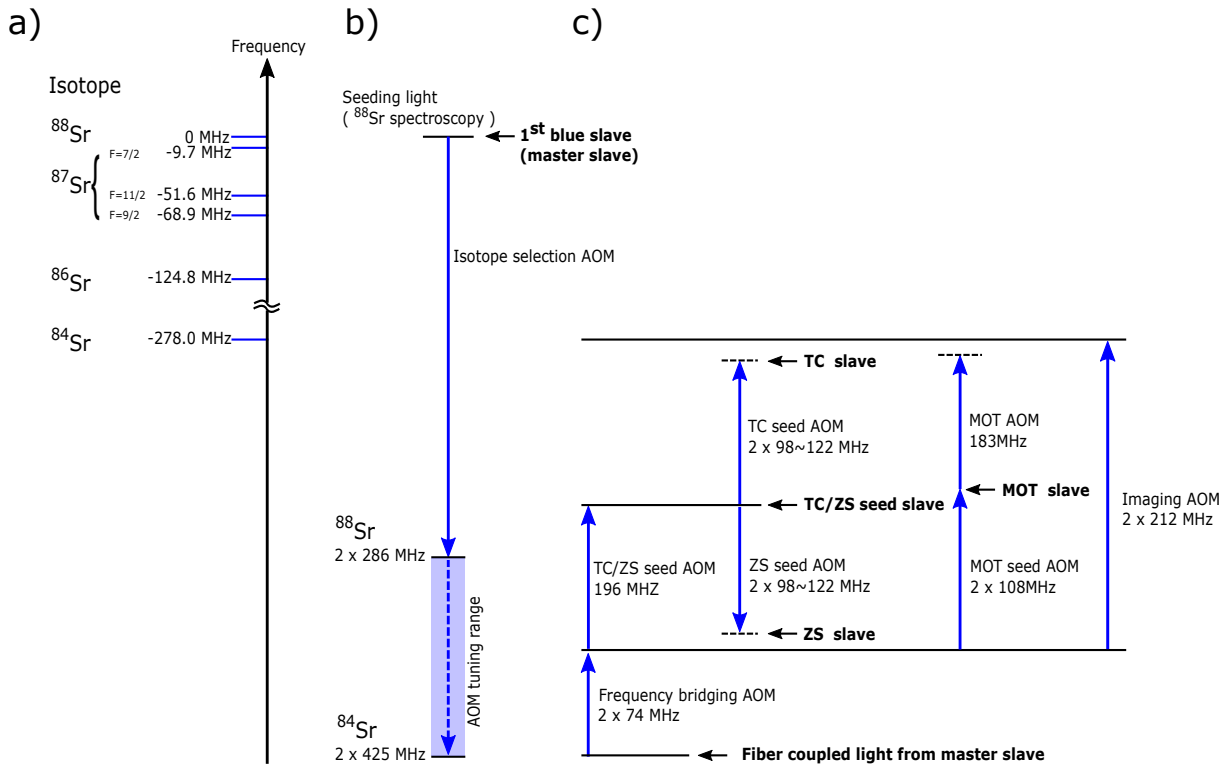
FIGURE 2.3: **Frequency scheme of the blue laser system used to address all stable Sr isotopes.** (a) The isotope and hyperfine shifts of the $^1S_0$ - $^1P_1$ transition, referenced to the ^{88}Sr line. (b) The "master" slave laser is the first seeded 461-nm laser in the setup, and it is seeded using light from a home-made ECDL referenced to a ^{88}Sr spectroscopy signal. Through the isotope-selection AOM, the master laser light is frequency shifted, and fiber coupled to the following stage AOMs for additional frequency shifts in order to seed different slave lasers with different frequencies. (c) The frequencies used for the MOT, ZS, TC, and imaging laser beams, shown here for the case of ^{84}Sr. The frequency of all slave lasers except the master slave will simply follow the center frequency determined by the isotope-selection AOM shift. By only configuring the isotope-selection AOM, we can choose which Sr isotope to work with.

laser, transverse cooling lasers, and imaging beam. The saturation intensity of the Sr $^1S_0$ - $^1P_1$ singlet transition is $40.7\,\text{MHz/cm}^2$. To achieve sufficient power for specific applications (e.g. 2D MOT and transverse cooling), we set up dedicated slave lasers for each application. In the following we will describe the slave laser system for each of these applications.

2D MOT, transverse cooling (TC) — We have an individual slave laser for each axis of the 2D MOT beams and the two orthogonal axes of the transverse cooling. We add AOMs after the 2D MOT slaves for fast beam switching despite the goal of the experiment being steady-state operation, because only fast switching allows us to properly characterize the atomic beam. The light is guided from the AOMs to the

(a)

FIGURE 2.4: **Blue laser setup.** (a) The figure shows the optics layout on two 750mm × 750mm solid aluminum optical breadboards. Different color shading regions are sub-modules for different applications. (The purposes of individual sub-module are addressed in the main text). (b) Transverse cooling section. Cooling beam is passed four times side by side. (c) Laser beam from injection-locked Zeeman slower slave laser is guided to the atoms through free space.

vacuum chamber through optical fibers. See Fig. 3.1 for illustration of the vacuum apparatus and 2D MOT beams. Albeit we typically loose 40% of laser power by doing that we still prefer it since it guarantees a nice spatial mode, facilitates power balancing of counter-propagating beams and decouples the laser source alignment from the alignment of the beams onto the atoms. Another reason to implement these fibers is that they allow us to easily enclose all laser sources in boxes, which, in combination with mechanical shutters in front of the input fiber couplers, prevents detrimental stray light from reaching the location of the steady-state BEC. This is particularly important since the laser sources are located on the same optical table on which we want to make the steady-state BEC.

Zeeman slower (ZS) — For the Zeeman slower, we choose to guide the laser beam from the slave to the atoms through free space, and not through a fiber, in order to maximize power. The Zeeman slower performance is limited by the power available from its single NICHIA diode (70 mW after the isolator). Therefore this part of the setup will be the first thing to upgrade once a high power laser source is available.

2D blue MOT plug beams — We originally implemented two pairs of moving molasses beams aligned near-vertically along the un-confined axis of the 2D blue MOT. Later this setup was adapted for serving as 2D blue MOT plug beams, prohibiting atoms from propagating upwards. By including plug beams, we can on average improve the flux by 30%.

Injection lock monitoring — The implemented blue laser setup can stop functioning like a chain of dominoes tipping over because it relies on up to 3 stages of injection-lock staying locked simultaneously. Therefore, a failing lock, especially the one of the master slave, can trigger a chain reaction, with all sub-sequent lasers loosing their lock. It turned out to be a critical task to simultaneously monitor each injection lock. To be able to monitor the laser locks with minimum effort, we choose to combine light from the master slave laser, TC/ZS seed slave, and Zeeman slower slave and send it to a Fabry-Pérot interferometer. We also create beat signals from leakage light of the TC/ZS seed laser and the two 2D MOT lasers. We monitor both beat signals using an oscilloscope. For the transverse cooling lasers, we monitor the lock by looking at the fluorescence signal from the transverse cooling section.

TABLE 2.1: **Properties of 461nm laser beams used in the SrPAL apparatus.** Under "detuning" (start, stop) refers to the covered laser light detuning range relative to the resonant frequency that is accessible in the experimental setup. The normal operation value is also stated.

| Beam name	Detuning range capability [MHz]	Power [mW]	$1/e^2$ diameter [mm]	Comments
2D MOT	(-45, 3) -25 (-0.8Γ_{blue})	10.5	22.8	4 beams with centers at the same height as the Zeeman slower axis.
Zeeman slower	(-424, -472) 450	70	25.4	Focused to 12 mm diameter at the oven exit.
Transverse cooling	(-38, 12) -18 (-0.6Γ_{blue})	30	23×9.6	Beam is passed 4 times side by side giving a 90 mm long cooling region. Same for both horizontal and vertical axes.
Imaging X, Y	(-74, 26) ($-2.5\Gamma_{blue}$, $0.86\Gamma_{blue}$)	1.14	48	
Plug beams	(-53, -3) -13 ($-0.4\Gamma_{blue}$)	0.017	9.6	2 symmetric beams inclined at 8° to the vertical (y axis) and aimed at the top half of the blue 2D MOT.
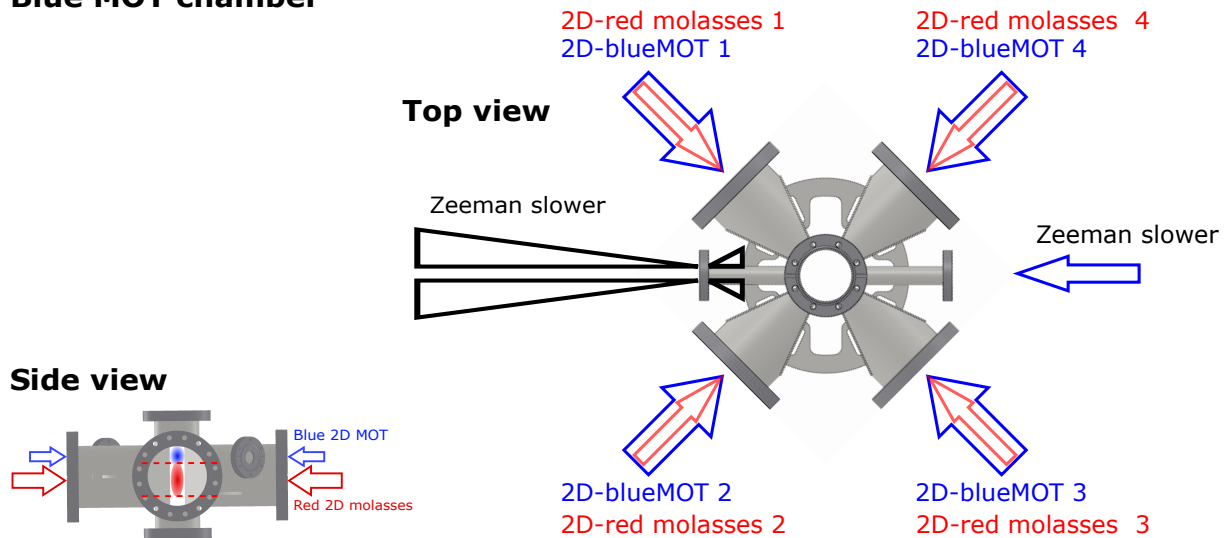
FIGURE 2.5: **Sr perpetual 2D MOT setup.** (a) Optical setup for 2D MOT laser cooling. The 461 nm transverse 2D MOT cooling beams and 689-nm 2D-molasses cooling beams. Relative beam sizes are listed in Tab. 2.1 for the 2D blue MOT and in Tab. 2.2 for the 2D red molasses.

2.3.2   Red, 689-nm laser system

The ^{1}S$_0$ - ^{3}P$_1$ intercombination transition has a natural linewidth of 7.4 kHz and therefore the laser used to address this transition needs to have a linewidth and long-term stability smaller than this value. The 689-nm master laser setup has been built for the RbSr project of our group. A master laser (Toptica) is locked to a cavity with a finesse of about 15 000, to reduce the laser linewidth. Details of the setup, including cavity construction, are given in Simon Stellmer's thesis [41]. A primary difference between the RbSr machine and a standard ultracold atom machine is that we implement the laser cooling steps sequentially in space whereas in the usual cold atom experiment, several different cooling steps are accomplished sequentially in time. Thus instead of having a single AOM configuring the intensity sequentially in time, we need to have multiple AOMs controlling multiple beams for the different cooling stages that require different intensities and are sequential in the space domain. In total, we need many individually controlled light sources for our experiment. A further design requirement for the red laser system is that we want to operate the machine with any Sr isotope. The isotope shifts and hyperfine splittings are well known [41], and allowed us to design a laser system with the desired flexibility, see Fig. 2.6.

Red slave lasers — Our slave lasers are constructed in the usual way and the following description is representative of most injection lock assemblies. A single red slave laser is composed of a laser diode (LD, Opnext, HITACHI, HL6738MG, 30 mW) collimated by an aspherical lens (Thorlabs, C330TMD-B). A pair of telescope lenses[5] is used for beam shaping. An optical isolator (LINOS, FI-680-5SV) is placed after the beam shaping optics and injection lock light is seeded into the diode as usual, through the side port of the isolator's polarizing beam cube that is away from the diode.

Our red laser setup comprises multiple beam paths, as shown in Fig. 2.6 and listed in Tab. 2.2. We use the light transmitted through the RbSr master laser lock cavity as the light source to seed the first slave laser, see Fig. 2.6 (b). Its light is then fiber-coupled to seed another slave laser to amplify the power level. Laser light is then distributed into different beam paths, each of which can be independently frequency shifted. The ^{88}Sr path requires no frequency shifting, whereas laser light for other isotopes (^{84}Sr, ^{86}Sr, ^{87}Sr) is shifted by AOMs according to the isotope shift shown in Fig. 2.6 (a). Laser light is then distributed into four different fiber coupler paths for seeding next stage

---

[5]Thorlabs, 1st lens: LJ1402L1 (40 mm), 2nd lens: LK1426L1(-25 mm)

slave lasers. The distribution setup is designed such that the fiber coupler paths are multiplexed. Different isotope shifted light shares the same coupler that goes to the next stage slave lasers as depicted in Fig. 2.6. Mechanical shutters are integrated into the distribution beam paths to enable isotope selection.
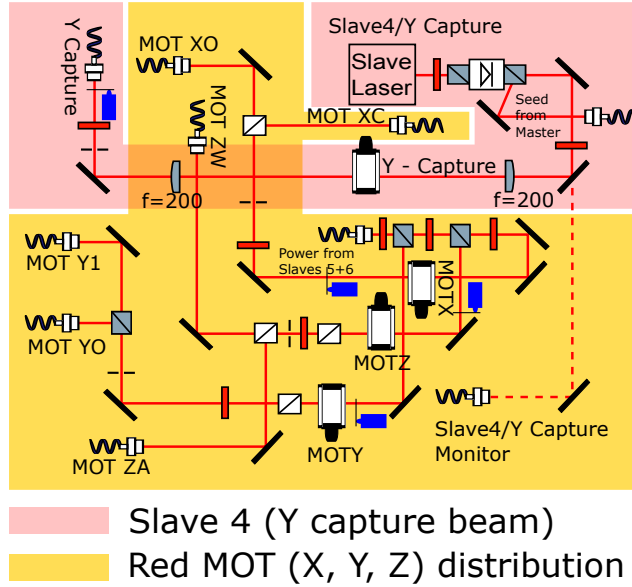
Laser frequency noise - servo bumps

The red laser seeding light from the primary master laser has a noticeable spectral noise, see Fig. 2.8. After injection-locking, this noise gets amplified together with the carrier by the slave laser diode. We were not aware of this undesired spectral property of the red laser until we encountered an instability problem in the SrPAL machine: the performance of the steady-state red MOT was sensitive to the electronic settings of the RbSr master laser lock. Interestingly, these settings did not influence the RbSr or Sr quantum gas microscope machines in our lab, which are also slaved to this master laser. The reason is that these machines are operated in a time-sequential manner. The laser is ramped from a frequency-broadened narrow-line red MOT stage to a single frequency narrow-line red MOT used for dipole trap loading. During these ramps, the laser power is reduced to intensities of just a few I_{sat}, where $I_{sat} = 3\,\mu\,W/cm^2$ for ${}^1S_0$ - ${}^3P_1$ transition. Since the unwanted frequency noise components have an intensity that is 20 dB lower than the carrier frequency, compared to the carrier laser frequency component of only few I_{sat} in the final state, the sidebands are too weak to have any effect on the atoms. On the contrary, in the steady-state capture red MOT case, see red MOT I configuration in Fig. 3.1, we show slowing of an atomic beam with a velocity of 6 m/s and trapping of that beam in a MOT using the 689-nm intercombination transition, where the vertical Y capture red MOT beam operates at high power (10.8 mW) and uses a detuning range of -0.95 to -5 MHz. Its frequency and power-broadened operating condition makes the residual spectral components not negligible, especially for those photons that are blue-detuned can heat the atoms in the steady-state MOT. We notice that the MOT is sensitive to the blue-detuned spectral component, which leads to the atomic cloud position changing in the vertical direction and becoming unreliable.

We characterized the spectrum of the master laser by superimposing its light with another ECDL that is offset-locked to the master laser by 80 MHz. The beat signal is recorded on a photodetector with 125 MHz bandwidth. The spectrum is analyzed with a resolution bandwidth (RBW) of 100 kHz and shows servo bumps 1.3 MHz away from

---

[6]Note that due to nonlinearities in the amplifiers and AOMs, it is not possible to separately measure the optical power in each component of the spectrum.

FIGURE 2.6: **Red laser setup I.** (a) Frequency shift scheme of the red laser system. Through isotope-selection AOMs the laser center frequency from the main master laser is shifted to seed multiple slave lasers for different applications. (b) The figure shows a "filter slave" laser that is seeded by cavity filtered light from the main master laser. We drive the slave laser at its lowest current injection-locked mode in order to be able to seed it with the small amount of light power transmitted through the cavity. (c) Multiple slave lasers are injection-locked using the light derived from the "master slave" amplification stage and laser frequencies. Their frequency is configured for different experimental applications, see main text. Acronyms following the fiber annotation indicate the fiber output locations (W: wall, A: aisle, C: computer, O: oven, coordinates referenced to the optics table of the experiment).

(a)

Slave 4 (Y capture beam)
Red MOT (X, Y, Z) distribution

(b)

Slave 5 Z-capture MOT, MOT beam distribution
Slave 6 ^{87}Sr isotope shift, Sisyphus optical lattice

FIGURE 2.7: **Red laser setup II.** (a) **Red MOT distribution.** Slave 4 is mainly used for the Y-capture MOT beam. Laser light coupled from slave 5 and 6 is distributed among Red MOT X,Y, and Z beam paths. (b) **Red MOT power, Sisyphus optical lattice and frequency shift AOM for the fermionic isotope.** Slave laser is seeded using light from the master slave laser, and frequency shifted for the fermionic ^{87}Sr isotope. The light is then sent to the seed light source distribution setup.

the carrier with a full-width-half-maximum (FWHM) of ~ 1.5 MHz, see Fig. 2.8. These bumps are suppressed by 20 dB compared to the carrier. We suspect that these servo bumps are also present on the slave laser light used for laser cooling. An indication that this is indeed the case is obtained by atom loss spectroscopy using BECs as samples, see Fig. 2.9. We record the number of Sr atoms in the BEC after exposure with the red MOT light for 100 ms at an intensity of $3\,\mu$ W/cm^2, corresponding to a saturation parameter of 1. The shape of the spectral feature matches the shape of the sidebands of the master laser, see Fig. 2.8. The light in the servo bumps of the capture MOT beams is therefore resonant with atoms in the steady-state red MOT and powerful enough to disturb its operation. Removal of this light is mandatory to reach stable operation.

Filter cavity

In order to remove the servo bump component from the master laser light we use the cavity to which the master laser is locked as a narrow band filter (finesse 15000, FWHM linewidth 100 kHz) [42, 43]. Sending the master laser light through this cavity can theoretically reduce the servo bumps by eight orders of magnitude. Of the 130 μW we couple into the cavity only 30 μW are transmitted. We cannot further increase the power coupled into the cavity because we worry about the substantial thermal effects that this could have on the cavity mirrors, which would lead to unwanted thermal-induced resonance drift. Fortunately this power level is already enough to injection lock one slave diode laser, as long as this slave is operated at its lowest current seeded lasing mode. In this case the power of the seed can as desired overcome the power that is back reflected from the output diode facet into the diode in unseeded operation. A further detail of our setup is that we installed a Faraday isolator after the cavity to avoid light from the slave laser to be sent back into the cavity, disturbing the master laser lock.

TABLE 2.2: Properties of laser beams used for a specific laser cooling configuration, Red MOT II(a), see Chapter 3. Under "detuning" $\Delta_1 : \delta : \Delta_2$ refers to a modulated comb of lines from Δ_1 to Δ_2 with a spacing of δ.

| Beam name	Detuning [MHz]	Power [mW]	$1/e^2$ diameter [mm]	Comments
2D Red molasses	-0.03 : 0.025 : -0.75	4.6	45.6×18.2	2 sets of 2 counter-propagating beams, centered 38 mm below Zeeman slower plane.
Red MOT I Y	-0.5 : 0.017 : -4	10.8	68	Waist given 22 cm below the quadrupole center. Beam focused on the bottom baffle 22 cm above the quadrupole center at $z = +10$ mm from the central axis of the falling atomic beam.
Red MOT I X	-0.7 : 0.015 : -3	3.3	47	2 counter-propagating beams
Red MOT I Z Outer	-0.7 : 0.016 : -4	1.14	48	2 counter-propagating beams with an 8mm hole to allow Red MOT II Z Inner beams to pass.
Red MOT II Z Inner	-0.1 : 0.017 : -0.25 -0.26 : 0.015 : -2.85	0.063[6]	8	2 counter-propagating beams
Red MOT II Y	-0.1 : 0.016 : -0.25 -0.26 : 0.014 : -2.85	0.43[6]	36	1 upward-propagating beam
Red MOT II X	-0.1 : 0.017 : -0.25 -0.26 : 0.013 : -2.85	0.099[6]	28.8	2 counter-propagating beams
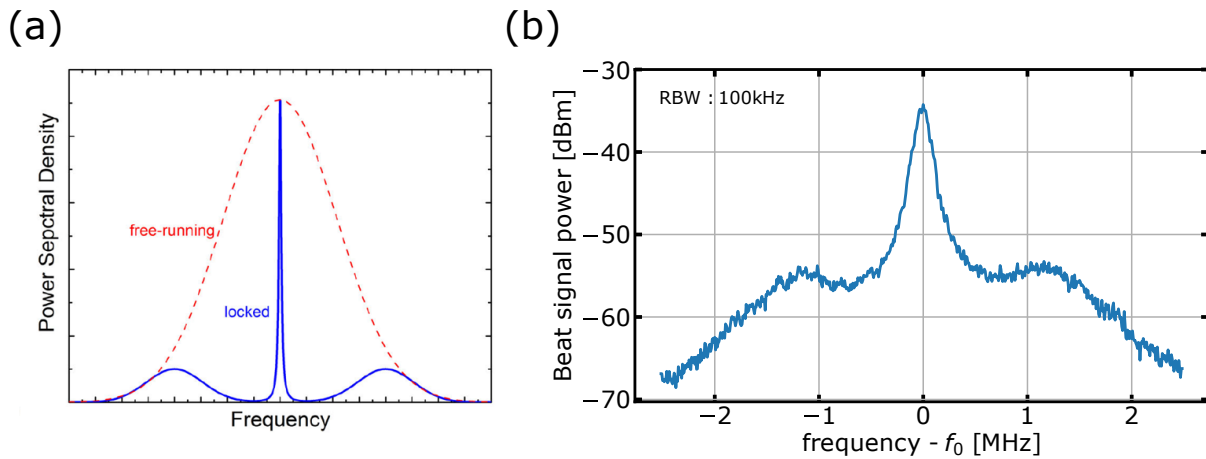
FIGURE 2.8: **Red laser frequency noise: servo bumps.** (a) Comparison between the power spectral densities of a free-running and a locked laser. The frequency lock reduces the low frequency noise, technically limited by the detector noise level. A narrow central carrier in the power spectral density appears, surrounded by two high-frequency noise peaks, the "servo bumps". Figure taken from [44]. (b) Beatnote signal between two laser beams that are independently frequency stabilized. The beatnote appears at $f_0 = 80$ MHz, which is the frequency offset of the two lasers, and clearly shows servo bumps 1.3 MHz away from the carrier.
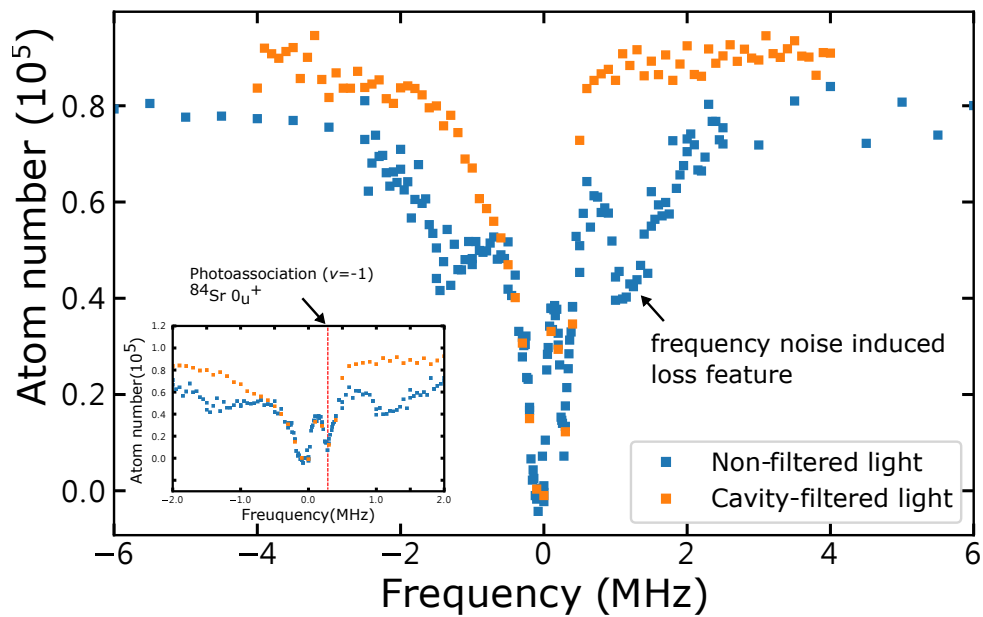
FIGURE 2.9: **BEC loss spectroscopy.** The atom number of a ^{84}Sr BEC exposed to light from the red laser system is plotted versus the detuning of that laser from the $^1S_0$ - $^3P_1$ transition. The blue data points are recorded using light from a slave that is directly seeded by master laser light, whereas the orange data points use a slave that is seeded by cavity-filtered master laser light. The servo bumps are clearly suppressed when using the filter. The inset is a zoom in on the central part of the loss feature and shows more clearly a Sr_2 photoassociation resonance corresponding to the least bound vibrational level of the $^{84}Sr_2$ $^1S_0$ + $^3P_1$ molecule [45, 46].

2.3.3 $^3P_0 - {}^3S_1$ and $^3P_2 - {}^3S_1$ repumpers

The atomic beam flux plays a critical role for the SrPAL machine performance, since a high flux is crucial to reach the critical PSD for the BEC phase transition. Repumping lasers for the 2D blue MOT are essential to obtain a high enough flux. As shown in Fig. 2.10, the nonzero branching ratio between the $^1P_1$ and $^1D_2$ states opens a decay channel out of the otherwise cycling blue MOT laser cooling transition. Atoms that escape the MOT cycle to $^1D_2$ further decay into the $^3P_{1,2}$ metastable triplet states with a branching ratio of $2:1$. From the $^3P_1$ state atoms decay on a timescale of $21\,\mu s$ back into the ground state, but atoms in $^3P_2$ stay there for minutes and are no longer available for the experiment. In order to minimize this loss of atoms and thereby increase the atomic flux, we need a method to transfer atoms back from the $^3P_2$ state into the ground state. Alternatively we can quickly pump atoms from the $^1D_2$ state into a state that decays with high probability to the ground state, so that the long-lived $^3P_2$ state is never populated [47]. Some of these schemes are shown in Fig. 2.10 and described in the following.

Five repumping schemes pump atoms from the $^3P_2$ state to a higher lying state that leads to decay into the ground state. They are labeled in the following with the state into which $5s5p\,^3P_2$ atoms are pumped.

- $5s6s\,^3S_1$ — Atoms decay from the $^3S_1$ state with a branching ratio of approximately $1:3:5$ to the $5s5p\,^3P_{0,1,2}$ states. Atoms that decay into $^3P_2$ can absorb another repumping photon, eventually decaying to $^3P_{0,1}$. Atoms in the $^3P_1$ state quickly decay to the ground state as desired. By contrast the $^3P_0$ state is also a long-lived state ($160\,s$ lifetime) and would lead to loss of atoms if no further measure is taken. We therefore implement a second repumping laser from $5s5p\,^3P_0$ to $5s6s\,^3S_1$ to close this loss channel. The strongly allowed $^3P_0 - {}^3S_1$ and $^3P_2 - {}^3S_1$ transitions are conveniently accessible by diode lasers (wavelength $679\,nm$ and $707\,nm$, respectively) and broad ($\Gamma_{679\,nm}/2\pi = 1.41\,MHz$, $\Gamma_{707\,nm}/2\pi = 6.68\,MHz$). They are therefore well suited for repumping and used in many Sr experiments.

- $5s4d\,^3D_2$ — Being the lowest level of the $^3D_2$ states, $5s4d\,^3D_2$ has a branching ratio of approximately $3:1$ to the $^3P_{1,2}$ states and does not decay to $^3P_0$. The $5s5p\,^3P_2$ - $5s4d\,^3D_2$ transition has a mid-infrared (MIR) wavelength ($3012\,nm$), which was historically technologically challenging to produce. Lasers of this frequency range have recently become available using optical parametric

oscillators (OPOs). However, this laser technology is more involved than diode lasers and also more expensive [48].

- $5s5d\,^3D_2$ — The second lowest $^3D_2$ state has a branching ratio of approximately $3:1$ to the $^3P_{1,2}$ states and does not decay to $^3P_0$. It is addressed by lasers at a wavelength of 497 nm. There are no laser diodes available at 497 nm and the simplest method to produce this light is frequency doubling an IR laser at 994 nm [41]. This repumping transition is used in our group and implemented in the RbSr and quantum gas microscope experiments.

- $5s6d\,^3D_2$ — The third lowest $^3D_2$ state also decays only to $^3P_2$ and $^3P_1$. It is addressed by lasers at a wavelength of 403.5 nm, which is very convenient owing to the availablity of laser diodes with Blu-ray technology. This repumping scheme was explored by us and is well documented in [49].

- $5p^2\,^3P_2$ — In this repumping scheme, using 481 nm light, atoms are excited from the $5s5p\,^3P_2$ state to the doubly-excited $5p^2\,^3P_2$ state. That state decays to the $5s5p\,^3P_2$ state with $\Gamma_{481}/2\pi = 14$ MHz and to the $5s5p\,^3P_1$ state with $\Gamma_{472}/2\pi = 5.7$ MHz [50]. These are the only two decay channels. On average each atom has to scatter $(\Gamma_{481} + \Gamma_{472})/\Gamma_{472} \sim 3.5$ repumping photons to return back to the ground state [51, 52].

The following scheme directly pumps atoms out of the $^1D_2$ state, preventing decay to $^3P_2$.

- $5s4d\,^1D_2 - 5snp\,^1P_1$ — This scheme involves repumping of strontium atoms from the $^1D_2$ state up to the $5snp\,^1P_1$ states at 717 nm [47, 53, 54], 533 nm, or 448 nm [55] for $n = 6, 7, 8$, respectively. According to Ref. [54], repumping of strontium atoms using 717-nm light was investigated and it only increases the MOT atom number by about a factor of two due to unfavorably large branching ratios. A higher principle quantum number state with $n = 8$ is currently studied in our group and will be presented in Jens Samland's master thesis [56].

As we will see in Sec. 2.3.4 the combined action of the red MOT laser and the transparency beam can pump atoms into the $^3P_0$ and $^3P_2$ states. Our original repumping scheme, relying only on a $^3P_2$ - $^3D_2$ laser, is not able to recover atoms lost to $^3P_0$. In addition the available repump laser power was very limited. To overcome these challenges we implemented the repumping scheme exploiting $5s6s\,^3S_1$. A
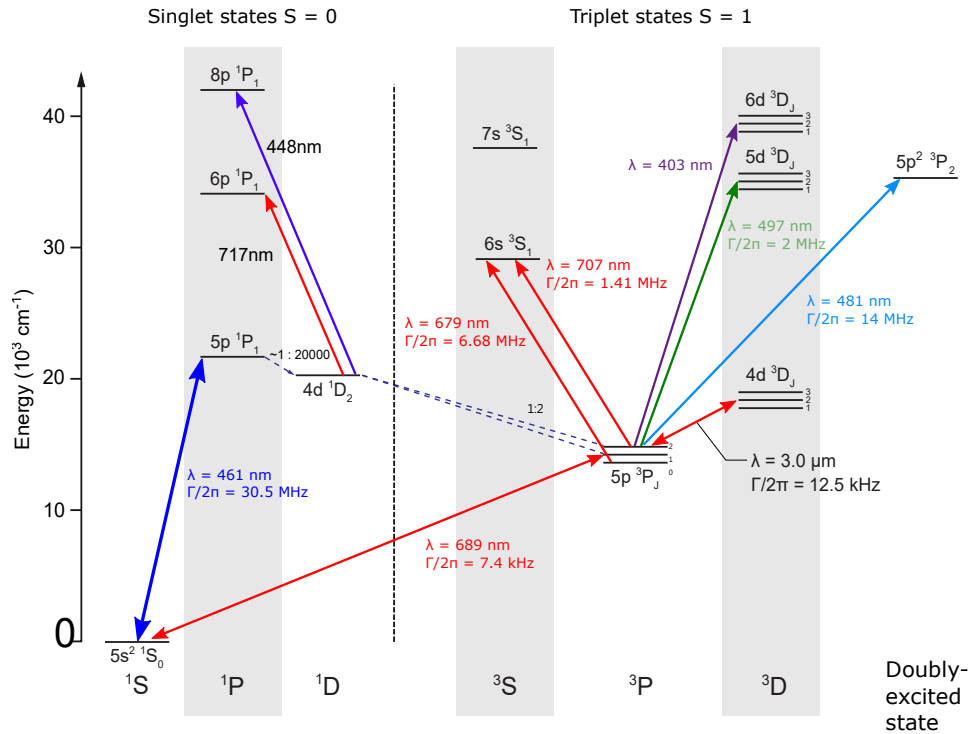
FIGURE 2.10: **Strontium repump schemes.** The broad 461-nm transition enables us to achieve efficient laser cooling. Due to the nonzero branching ratio between the $^1P_1$ and the $^1D_2$ state a decay channel out of the laser cooling cycle is opened. This branching ratio is roughly 1 : 20000 for Sr [57]. The atoms then decay further into the $^3P_{1,2}$ metastable triplet states with a branching ratio of 2 : 1. Several repumping schemes are also shown using $5sns\,^3S$, $5snd\,^3D$, $5s^2$, or $^3P_2$ as intermediate levels for pumping atoms to the $^3P_1$ state, before the further decay to $^1S_0$. Another repumping scheme avoids decay to $^3P_2$ by quickly pumping atoms out of the $^1D_2$ state via the $5s6p\,^1P_1$ or $5s8p\,^1P_1$ state.

schematic of the repump laser setup is depicted in Fig. 2.11. The optical power is distributed on three paths and fiber-coupled to the SrPAL vacuum chamber. One beam is dedicated for repumping the Sr 2D blue MOT section. The two other beams are for applications in the Sr red MOT chamber; one is combined with the transparency beam, and the other is used for ^3P manifold state transfer. Both lasers are locked onto the same cavity using the PDH technique [58, 59].

Two homemade ECDLs are built for $^3P_0 - {}^3S_1$ and $^3P_2 - {}^3S_1$ repumping. We operate the 679-nm ECDL[7] at 38 mA and the diode is operating at a temperature of 19 °C, obtaining 6 mW. The 707-nm ECDL[8] is operated at 44 mA and a diode temperature of 30 °C, delivering 2 mW. Both power levels are measured at the fiber

---

[7]Using an InGaAlP laser diode (QL68J6SA) from Roithner Lasertechnik GmbH.
[8]Using an InGaAsP laser diode (HL7001MG) from Thorlabs.
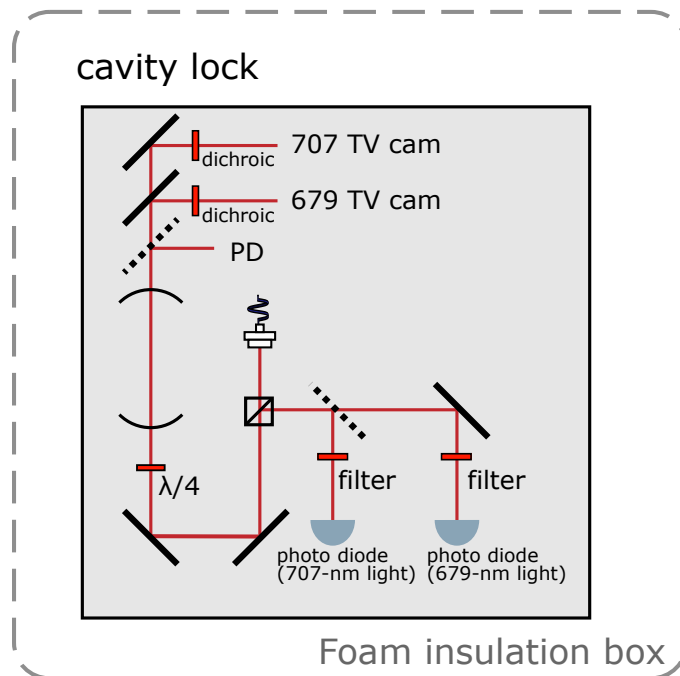
(a)
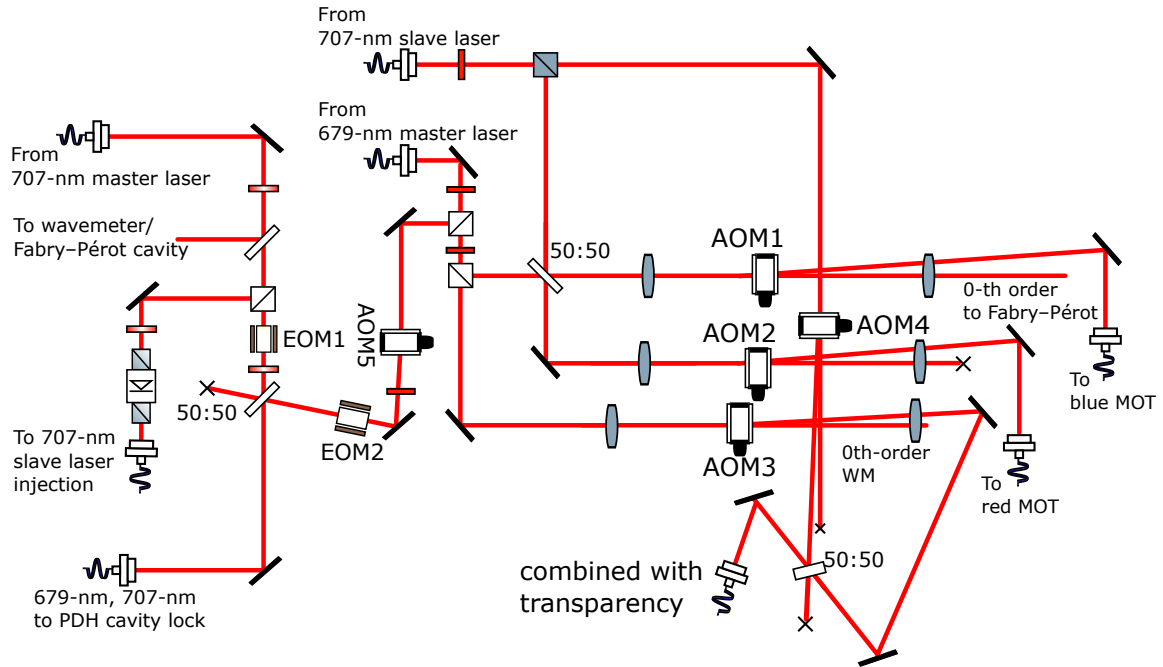
(b)

FIGURE 2.11: **679-nm and 707-nm repump laser setup.** (a) Both master lasers are fiber coupled and sent to the distribution setup, see main text for explanation of the setup. (b) Frequency stabilization for 679 nm/707 nm lasers. Both lasers are locked onto the same cavity using the PDH technique.

output of each master laser setup. We have sufficient power from the $679\,\mathrm{nm}$ ECDL for both the PDH locking and the distribution paths towards the SrPAL vacuum chamber. The power level of the 707-nm ECDL was chosen because we observe that the power degrades fast if we try to operate at higher current. To meet the power level required for our experiment, we built a slave laser[9], see Fig. 2.11.

To lock both lasers onto the same cavity, which has a finesse of 5000, $80\,\mathrm{\mu W}$ optical power from each ECDL is coupled into the same polarization maintaining fiber and sent onto the cavity. In our PDH locking scheme, the two different wavelength lasers sent to the cavity are frequency modulated with different modulation frequencies via home-made electro-optic modulators (EOM). The cavity reflection is then split on a 50:50 beam splitter before being sent to two photo detectors, one for each wavelength. An optical bandpass filter, letting pass only the desired wavelength, is placed in front of each detector to avoid disturbance by the light of the undesired wavelength.

2.3.4 Transparency laser

The transparency mechanism comes from the light shift (AC-Stark shift) induced by the laser perturbing the energy level. In the "laser cooling to BEC" experiment, the transparency mechanism is implemented through a near-resonant laser beam blue-detuned to the $^3P_1$ - $^3S_1$ transition, as shown in Fig. 1.2. A dipole moment d is induced in the atom through interaction with the rapidly oscillating electromagnetic radiation (laser). The induced atomic dipole moment is proportional to the field amplitude E, $\mathbf{d} = \alpha(\omega)\mathbf{E}$, where α depends on the driving frequency ω. In turn, the induced dipole moment interacts with the electric field, leading to a time-averaged interaction potential given by [60]

$$U_{\mathrm{dip}} = -\frac{1}{2\epsilon_0 c}\mathrm{Re}(\alpha)I, \qquad (2.1)$$

where $\alpha(\omega)$ is the dynamic polarizability and $I = \frac{\epsilon_0 c}{2}|\mathrm{E}|^2$. For the calculation of the dynamic polarizability of a specific energy level, knowledge about all the dipole matrix elements of relevant transitions coupling the state is required [61, 62, 55, 63].

We here only consider the dominant term, because the transparency laser we applied is only a few tens of GHz blue-detuned to the $^3P_1$ − $^3S_1$ transition, see Fig. 1.3(a). In a two-level atom approximation, the AC-Stark shift of the lower state $|g\rangle$

---

[9]$500\,\mathrm{\mu W}$ from the 707-nm ECDL is sent to the slave laser injection lock, see Fig. 2.11.
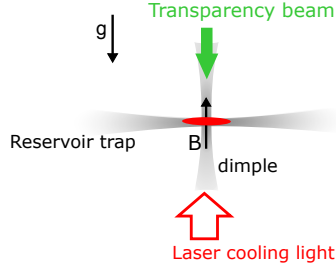
a) Laser cooling to BEC b) Steady-state BEC experiment

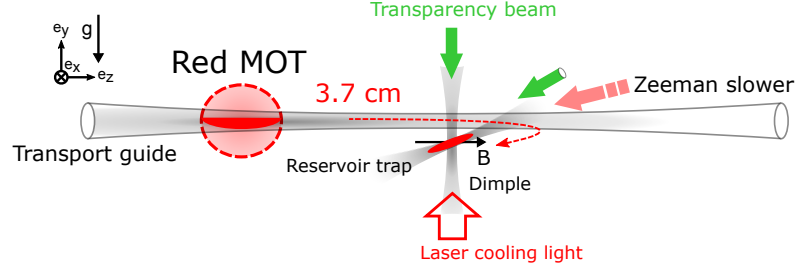FIGURE 2.12: **Magnetic quantization axis for the reservoir trap.** (a) In the "laser cooling to BEC" experiment the transparency beam is almost co-aligned with the magnetic quantization axis. (b) In the steady-state BEC experiment the reservoir trap is located in a place where the quantization axis, determined by the steady-state red MOT quadrupole field, is parallel to the reservoir trap.

is

$$\Delta E = -\frac{3\pi c^2}{2\omega_0^3}\left(\frac{\Gamma}{\omega_0 - \omega} + \frac{\Gamma}{\omega_0 + \omega}\right)I(r) \cong \frac{3\pi c^2}{2\omega_0^3}\left(\frac{\Gamma}{\Delta}\right)I(r), \qquad (2.2)$$

where ω is the laser frequency, ω_0 is the transition frequency from $|g\rangle$ to the higher lying state $|e\rangle$, Γ is the transition linewidth, and $\Delta \equiv \omega - \omega_0$ is the laser's detuning from the transition. The two-level approximation holds if $|\Delta| \ll \omega_0$.

The transparency beam is employed to shift the $^3P_1$ state by $h \times 10\,\text{MHz}$ upwards in energy. The $^1S_0$ - $^3P_1$ transition is therefore detuned far away from the frequency of red MOT laser and red MOT fluorescence photons. The scattering rate of these photons is significantly decreased in the volume of the transparency beam, making it possible to create BECs there.

In the laser cooling to BEC experiment [11], only one transparency beam is applied and aligned along the quantization axis, which is chosen to be parallel to the local magnetic field and perpendicular to the reservoir plane, see Fig. 2.12(a). The cooling light consists of an upward propagating, circularly polarized beam, red detuned by about $15\,\text{kHz}$ from the σ^+ $^1S_0$ - $^3P_1$ transition, with only negligible admixtures of other components. In this setting the cooling light only addresses the $^3P_1$ $m_J = +1$ state, whereas the others are not accessible because of selection rules, and also because they are shifted away by the applied magnetic field. Therefore the transparency only needs to shift the $^3P_1$ $m_J = +1$ state, which is possible with a single transparency beam.

By contrast, in our experiment the magnetic field is oriented in the horizontal plane, orthogonal to the vertical transparency beam. Furthermore the magnitude of the magnetic field is limited to about $0.8\,\text{Gauss}$, making it impossible to split the $^3P_1$

m_J states much. Therefore we would like to shift all three m_J states by about 10 MHz up in energy. However, as a detailed calculation [64] shows, coupling of $^3P_1$ to $^3S_1$ by a single transparency beam cannot achieve this. Therefore we use two transparency beams in our setup. The first beam is counter-propagating with the dimple dipole trap beam and covering the entire BEC region, see Fig. 2.12 (b). It has a beam waist of $28\pm2\,\mu$m in the plane of the sheet-shaped reservoir dipole trap. The second transparency beam is propagating nearly horizontally, with an angle of $12°$ to the horizontal plane (xz plane) and $42°$ to the vertical (yz plane) and has a waist of $\sim\ 41\mu$m, see Fig. 2.12 (b). Operating the two beams with a frequency offset of 700 MHz allows us to shift all three m_J states.

2.3.5 Dipole trap

An overview of the optical dipole trap (ODT) laser setup is given in Fig. 2.13. We use a 20-W IPG ytterbium fiber laser (wavelength: 1070 nm, linewidth: 1.115 nm). The setup uses three 80-MHz AOMs[10] to control the intensities of three beams that are delivered via polarization maintaining fibers to the vacuum chamber. The laser polarization is set to vertical when passing light through the AOM as other orientations would lead to polarization drift on thermal time scales. The diffraction orders and frequencies are set to different values in each AOM path (81.537, 79.386, 80.729 MHz) to avoid interference between the ODT beams, although the risk of interference is low because of the broad linewidth of the laser source. The AOMs are used in single-pass configuration. Collimated beams are sent through the AOMs, with the beam size chosen as a compromise between diffraction efficiency, rise time, and crystal laser damage thresholds. The used beam size is $\sim\ 1.6\,$mm diameter, which results in an estimated rise time of $4\,\mu$s[11]. Typically 95% AOM diffraction efficiency is achieved. Fibers are injected with S+K 6.2-03 collimators[12], and we reach fiber coupling efficiencies of 90(2)%. For the AOM path with high power (> 15 W). We use 3-meter high-power fibers[13], which are capable of transmitting optical powers of approximately 13 W to the fiber output before Brillouin scattering sets in. The linear polarization of the light is carefully aligned with the fiber axis to keep the polarization stable.

---

[10]Gooch & Housego, 3080-194 (TeO$_2$ - 80 MHz)

[11] The sound velocity in the common modulator material TeO$_2$ is 4160 m/s.

[12] Schäfter + Kirchhoff GmbH S+K 6.2-03

[13] OZ optics, PMJ-A3AHPC, high power coreless fiber end cap, air gap connector
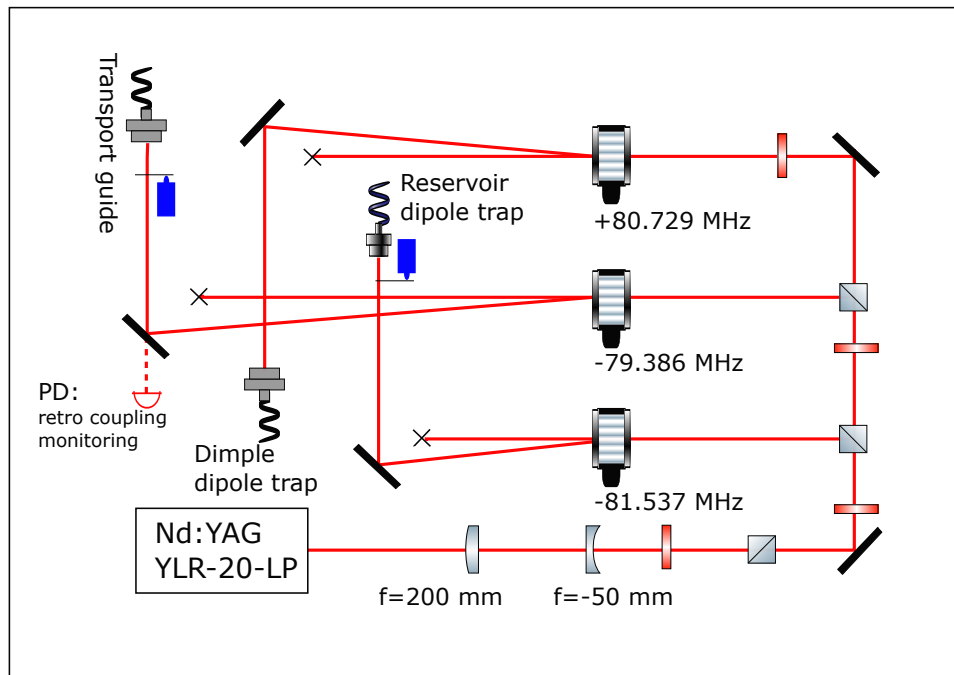
FIGURE 2.13: Schematic of the ODT laser source. We distribute power between transport dipole trap, reservoir dipole trap, and dimple dipole trap beams by varing half-wave plates in the beam path.

Transport guide

The transport guide is an elongated optical dipole potential that can guide atoms from the bright capture red MOT region into a much darker region that is 37 mm away, see Fig. 2.1. Several criteria have to be considered when designing the transport guide. At the capture MOT location, both trap-size and trap-depth have to be ideal for efficient atom loading. This constraint favours a large and deep trap. Another requirement is that the atoms have to be levitated against gravity over the rather long transport distance. Roughly speaking this requires that the potential of the guide in absence of gravity, U_0, is deeper than the gravitational potential difference mgr over the radius of the guide r, where m is atomic mass and g is the gravitational acceleration. More precisely, the potential of the guide including the effect of gravity has to be deeper than about ten times the temperature of the gas in order to avoid loss of atoms by evaporation. Guaranteeing this condition along the whole guide is not trivial.

A Bessel beam could be a good choice since the size and intensity of an ideal Bessel beam's core doesn't change over distance due to its non-diffractive property. A transport dipole guide built using this type of beam has been demonstrated and used
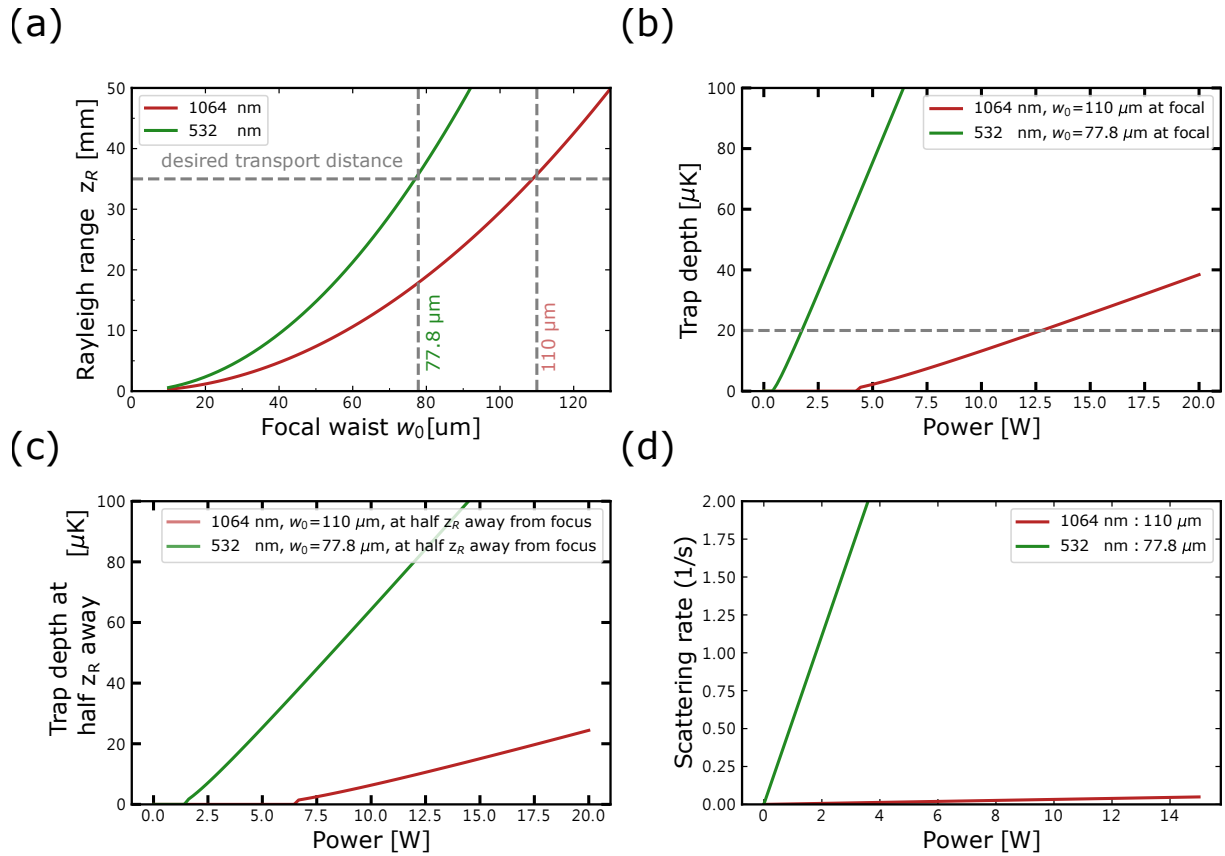
(a)

(b)

(c)

(d)

FIGURE 2.14: **Transport guide with light of different wavelength.** (a) Rayleigh range as a function of beam waist. Setting 37 mm as a target transport distance, distance leads us to choose this value for the Rayleigh range of the transport guide. (b) Trapdepth with gravitational sagging as a function of beam power at focus. (c) Trapdepth with gravitational sagging as a function of beam power at an axial distance of half a Rayleigh length away from the focus. (d) Scattering rate as a function of applied beam power.

to transport ultracold atoms over up to 20 cm [65]. However, due to the fact that a Bessel beam has its energy (or power) evenly distributed among its ideally infinitely many rings, this type of guide requires an enormous amount of power [66, 67].

We thus choose to work with a Gaussian beam instead of a Bessel beam. In order to keep the potential depth reasonably constant along the guide, we choose a Rayleigh length $z_R = \pi w_0^2 / \lambda$ comparable to the transport distance, 37 mm.

We now have to decide which wavelength of light we should choose for the dipole guide. Suitable lasers with powers of a few 10 W are available at 1064 nm and 532 nm. Both wavelengths are red detuned with respect to the main transition originating from the ground state, which means both types of lasers lead to an attractive dipole potential and are in principle suitable for our application.
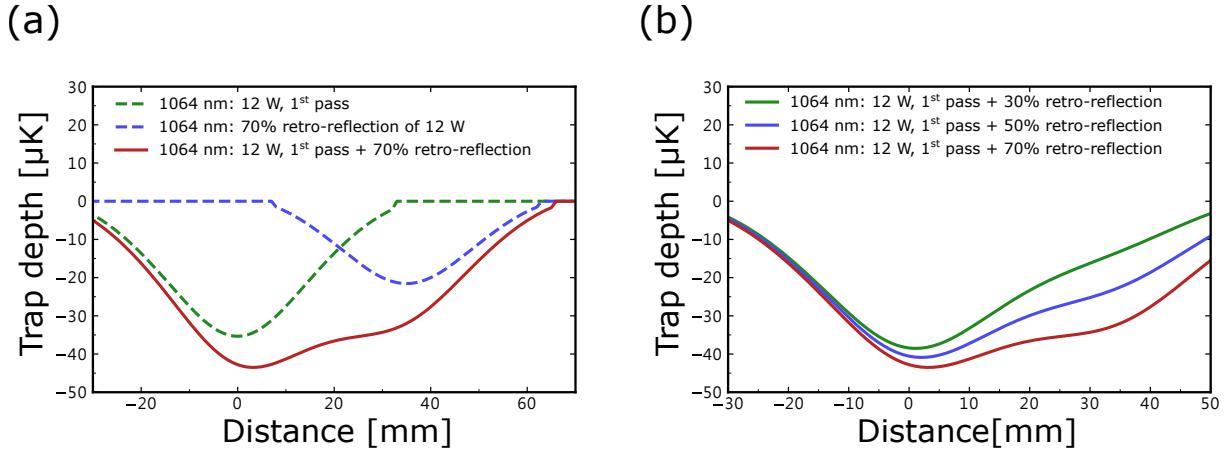
(a)

(b)

FIGURE 2.15: (a) Transport guide potential landscape along the axial direction. The calculation is done for beams with a waist of $100\,\mu$m and a wavelength of 1070 nm. The effect of gravitational sagging is included in the effective trap depth determination. Potentials of the first pass beam (dashed green), retro-reflected beam (dashed blue), and their sum (solid brown) are plotted. (b) Total potential for different retro reflection beam powers relative to first pass beam power.

In order to choose between them we calculate the beam requirements for a transport guide at these two wavelengths. In Fig. 2.14(a) the Rayleigh range is plotted in dependence of the focal waist size and it is clear that it is longer for the shorter wavelength, making it more favorable. Another advantage of 532 nm light is that the polarizability of the Sr ground state atoms is ~ 3.2 times larger at that wavelength than at 1064 nm. We estimate that the atomic beam velocity is $\sim$10 cm/s, a multiple of the typical thermal velocity for an atomic sample with a temperature of $\sim$1 μK. The desired guide needs to confine atoms at that velocity radially, which leads to a few tens of μK guide depth. We compare both wavelengths using waist sizes that give a Rayleigh range equal to the planned transport distance, 37 mm. As shown in Fig. 2.14 (b), we see that to achieve a reasonable trap depth of $\sim$20 μK, one requires 12 W of 1064 nm light, whereas one only needs $\sim$1.75 W of 532 nm light. If we also consider the off-resonant scattering rate and we assume an atomic beam with velocity of 10 cm/s, the transport will take $\sim$300 ms and nearly every atom will scatter a photon during transport, leading to heating. The heating from the scattering of a single photon increases the temperature of the gas by only 10%, which is negligible. Therefore, the simulation suggests comparable performance for a transport guide built either using a 1064 nm laser or a 532 nm laser. We choose 1064 nm because of the availability of a high power light source in our group.

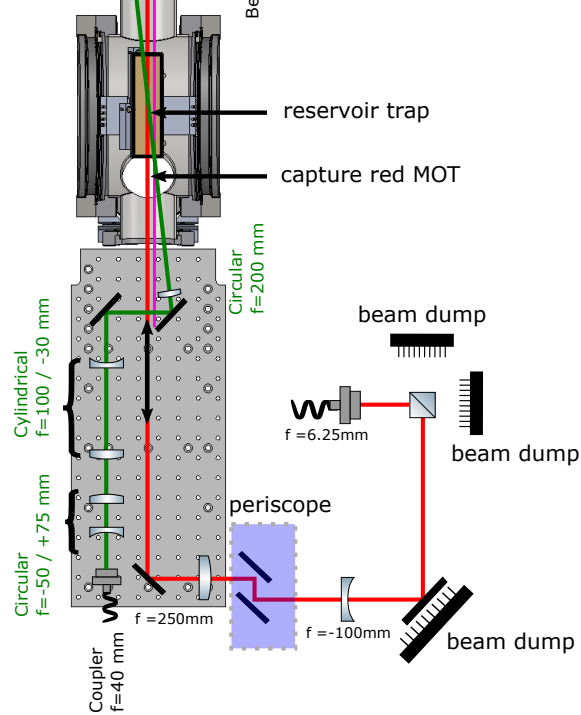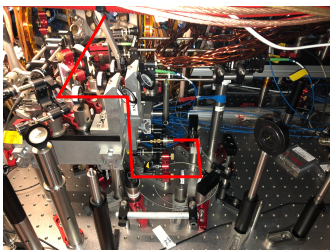To simplify the task of keeping a sufficient trap depth along the whole transfer
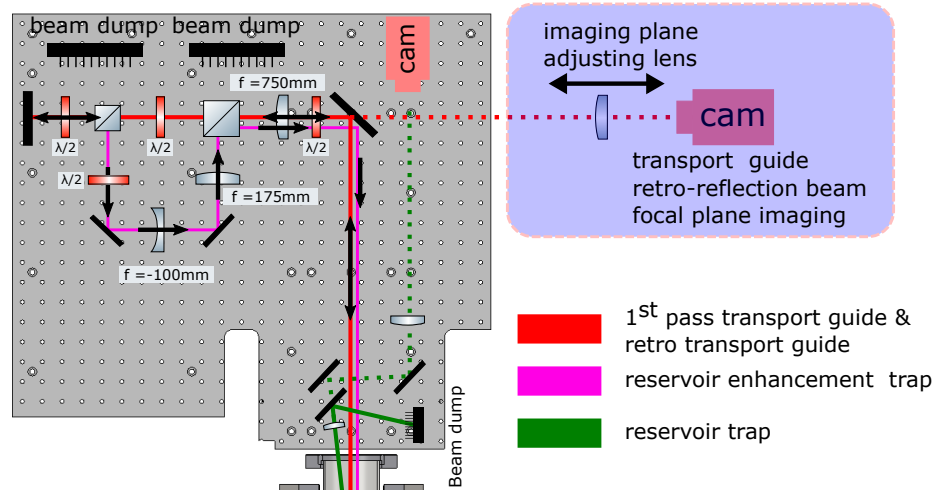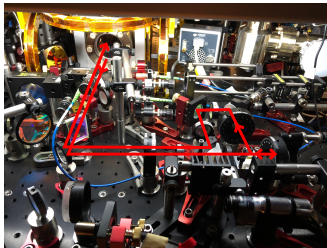
FIGURE 2.16: (a) Sectional drawing of the atom laser chamber, including the breadboard for optics relevant to the transport guide setup. (b) A photograph of the transport guide retro-reflection and reservoir enhancement optics. (c) A photograph of the transport guide first pass optics.

distance we choose to retro-reflect the transport beam. Since the linewidth of our laser source[14] is 1.115 nm, the coherence length $L_{\mathrm{coh}} = c/\pi\Delta\nu$ is only 0.3 mm, which means that we can ignore interference between the counter-propagating beams. Retro-reflection has two advantages. First, it approximately halves the required beam power. Second, we can obtain a flatter potential landscape along the transport axis compared to a single Gaussian beam. This can be achieved by placing the focus of the incoming beam onto the starting point of the transfer and the focus of the retro beam onto the end point. This allows us to effectively overcome the limitation originating in the finite Rayleigh range of 37 mm for the chosen waist of $100\,\mu$m. In this way we can engineer the axial potential landscape of the transfer guide, see Fig. 2.15. The infrared light of the transfer beams is fiber coupled[15] from a laser power distribution setup to the vacuum chamber, see Fig. 2.16.

2.3.6   Dark cylinder

In order for atoms to glide freely through the transport guide they may not be exposed to MOT laser beams. One of the MOT beam pairs is propagating parallel to the guide and we produce a dark shadow in those beams at the location of the guide. This shadow needs to stretch along the whole 37 mm transport distance and has to be small in diameter, such that the MOT still works well. The first idea to achieve this could be to place a dark spot on a glass plate into the MOT beam path or to image such a spot onto the beam path. However this would not result in the desired elongated and thin shadow region, a dark cylinder. A method that works is to image an elongated object, a thin metal wire, onto the transfer beam.

In Fig. 2.17 we show how this wire[16] is mounted. We use XY translator[17] mounts for the adjustment of the radial position of the two wire ends. The wire is hollow, which allows us to thread even thinner metal wire ($100\,\mu$m) through it. We threaded three thin wires through the hollow wire. At the hollow wire ends these thin wires are pulled in a tedrahedron shape sideways and glued to the XY translator with enough tension force to straighten the hollow wire. In this way, when we integrate the wire mounting setup into the beam path, we can fine-adjust the rigid wire position and

---

[14]YLR-20-LP

[15]OZ optics, PMJ-A3AHPC, high power coreless fiber end cap, air gap connector

[16]Dark cylinder object, a rigid thin wire that has an outer diameter of $600\,\mu$m, and an inner diameter of $400\,\mu$m.

[17]Thorlabs, CXY1, 30 mm Cage XY Translator

FIGURE 2.17: **Dark cylinder wire mount.** Each wire end can be adjusted using a radial translation stage.

orientation relative to the MOT beam at will. The wire is imaged onto the transfer beam using an imaging system with a magnification of one.

We built an imaging system to characterize the dark cylinder performance. The characterization setup is shown in Fig. 2.18. The transport guide dipole beam is combined with the z-axis MOT beam using a long-pass dichroic mirror. Due to the fact that the optics used here are not 100% perfect, we can still have some leakage red MOT light after the dichroic mirror, and also the back-polished IR mirror. We use this residual transmitted light for our dark-cylinder characterization. By adjusting the lens position in front of the camera, we can select a specific crossection plane within the beam path as our imaging plane. This allows us to make a full tomography of the region of interest, using the transport guide light as our position marker, see Fig. 2.18. In the particular planes shown in Fig. 2.18 (b,c) the dark cylinder is overlapping with the transport guide. Using this method, we checked the alignment of the dark volume across the whole region of interest, i.e. the plane corresponding to the capture red MOT up to the reservoir location 37 mm away. Due to the dark cylinder, red MOT light is attenuated by a factor of $30 \sim 40$ within the transport guide.
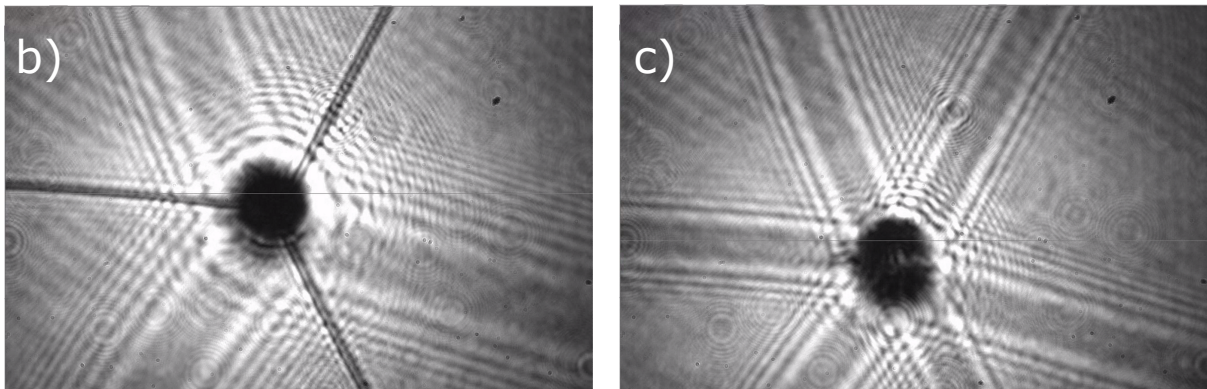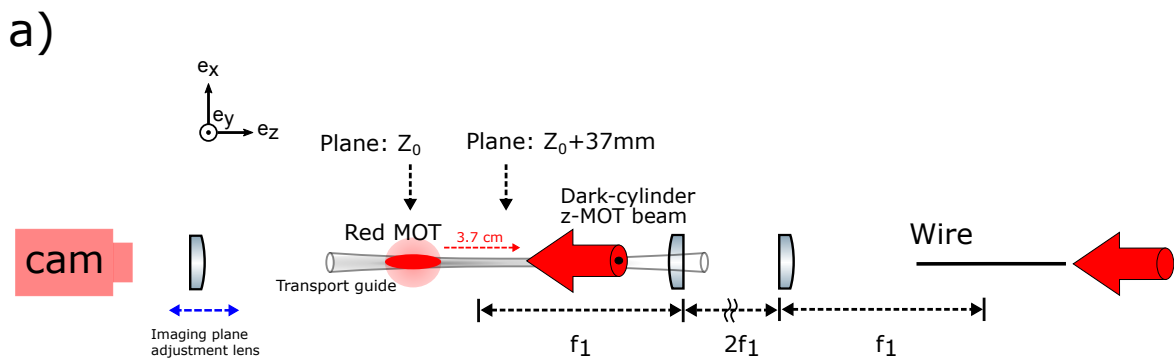
FIGURE 2.18: **Tomography of the dark cylinder inside the MOT beams.** (a) Tomography setup. The figure shows the imaging setup and a lens system that projects the wire onto the transport guide. (b) Imaging plane (z_0) at the edge of the 3D wire, which shows sharp focusing of the holding wires, suggesting that we are imaging the plane of one end of the dark cylinder crossection. (c) Imaging plane ($z_0 + 37$ mm away)

Chapter 3

Publication: A Steady-State MOT with 100 fold improved Phase Space Density

Shayne Bennetts, Chun-Chia Chen, Benjamin Pasquiou*, and Florian Schreck

Van der Waals-Zeeman Institute, Institute of Physics, University of Amsterdam, Science Park 904, 1098XH Amsterdam, The Netherlands

We demonstrate a continuously loaded ^{88}Sr magneto-optical trap (MOT) with a steady-state phase-space density of $1.3(2) \times 10^{-3}$. This is two orders of magnitude higher than reported in previous steady-state MOTs. Our approach is to flow atoms through a series of spatially separated laser cooling stages before capturing them in a MOT operated on the 7.4-kHz linewidth Sr intercombination line using a hybrid slower+MOT configuration. We also demonstrate producing a Bose-Einstein condensate at the MOT location, despite the presence of laser cooling light on resonance with the 30-MHz linewidth transition used to initially slow atoms in a separate chamber. Our steady-state high phase-space density MOT is an excellent starting point for a continuous atom laser and dead-time free atom interferometers or clocks.

3.1 Introduction

Laser cooled and trapped atoms are at the core of most ultracold quantum gas experiments [7], state-of-the-art clocks [69] and sensors based on atom interferometry [70]. Today, these devices typically operate in a time-sequential manner, with distinct

---
†

phases for sample preparation and measurement. For atomic clocks a consequence is the need to bridge the dead time between measurements using a secondary frequency reference, typically a resonator. This introduces a problem known as the Dick effect [71] in which the sampling process inherent to a clock's cyclic operation down converts or aliases high frequency noise from the secondary reference into the signal band, thus degrading performance [72]. Recently, a new generation of atomic clocks using degenerate atoms in a three-dimensional optical lattice has been demonstrated using Sr [73]. To reach the potential of such a clock, it will be necessary to overcome the Dick effect, which can be achieved by reducing the dead time and/or by creating vastly improved secondary references. Our steady-state MOT can lead to significant advances in both directions. It approaches the high flux and low temperature requirements needed for a steady-state clock, which would completely eliminate the Dick effect. Furthermore, our MOT is created under conditions compatible with the creation of degenerate samples or an atom laser [11, 74]. This would be the ideal source for a secondary frequency reference based on superradiant lasing, which is expected to outperform current references [75, 76, 77, 78, 79]. Our source and a future atom laser based on it might also be valuable for atomic inertial sensors [74]. Improved clocks and inertial sensors will allow tests of fundamental physics [80] or be suitable for gravitational wave astronomy [81, 82, 83, 70].

Over the years many creative approaches have honed laser cooling to produce pulsed samples of ever increasing phase-space density (PSD) [84, 14, 85, 86, 87, 88, 89, 90, 13, 28, 91, 92]. Pulsed MOTs using ^{88}Sr have demonstrated phase-space densities of 10^{-2} [93] while atoms held in dipole traps recently reached degeneracy [11, 12]. Despite the exquisite performances, these techniques suffer from extremely small capture velocities. As a consequence atoms must first be captured and precooled, and thus these techniques have only been used as part of time-varying sequences.

Several continuous high PSD MOT schemes have been demonstrated mostly based on bichromatic MOTs using alkaline earth atoms [94, 95]. The most successful reached a steady-state PSD of 1.2×10^{-5} [96]. This scheme used a MOT on a broad linewidth transition to capture atoms which then leak into a metastable state cooled by a MOT on a narrow transition. Narrow-line MOTs fed by a 2D MOT or Zeeman slower on the broad transition have been demonstrated for Yb and Er although steady-state PSDs are not measured [97, 98]. Another approach is the dark SPOT MOT [99], which creates a central spatial region of reduced laser interaction. Adding a further steady-state trapping and cooling stage to a MOT can increase the PSD

substantially [100, 31, 32], with a steady-state PSD of $\sim 4 \times 10^{-4}$ reached for Cr atoms at a temperature of $\sim 50\,\mu K$ [32].

3.2 Method

In this Letter, we demonstrate a ^{88}Sr MOT at a temperature of $\sim 2\,\mu K$ and a steady-state phase-space density of $1.3(2) \times 10^{-3}$, two orders of magnitude higher than reported for previous steady-state MOTs [96]. Combining our MOT with techniques such as [101, 11, 102, 100, 31, 32] promises yet higher PSDs and potentially a steady-state BEC and atom laser. Our result is achieved by flowing atoms through a series of spatially separated cooling stages as illustrated in Figure 3.1. First we use the high capture velocity of the broad-linewidth, "blue", $^1S_0 - {}^1P_1$ transition (30 MHz linewidth, 461 nm wavelength) in several stages to slow and cool atoms to mK temperatures, finishing with a 2D "blue" MOT. Next, we capture the atoms in a 3D MOT using the narrow-linewidth, "red", $^1S_0 - {}^3P_1$ transition (7.4 kHz linewidth, 689 nm wavelength), which can reach temperatures close to the recoil limit [93]. We operate the two MOTs in separate chambers to avoid heating of the 3D "red" MOT by blue photons scattered from surfaces and from fluorescing atoms in the 2D blue MOT. The transfer of atoms between chambers is ensured by two key ingredients: firstly, the atomic beam from the 2D blue MOT is collimated by a red optical molasses and secondly, the atoms are slowed in the second chamber by a hybrid slower+MOT configuration operated on the low capture velocity red transition. We show that this approach allows the red MOT to produce clouds with unprecedented phase-space densities for a steady-state apparatus. Furthermore, we show that the red MOT location is sufficiently protected to form BECs even with all the blue cooling stages operating.

The path of atoms through the setup begins with a high-flux atomic beam source adapted from our previous design [41, 103]. In brief, this source is composed of an oven similar to [104], followed by a transverse cooling stage and a Zeeman slower, both using laser cooling on the broad-linewidth blue transition. A 2D blue MOT [105, 106, 107], whose non-confining axis is oriented in the direction of gravity, is located approximately 5 cm after the exit of the Zeeman slower (see Figure 3.1a). This MOT has a loading rate of $2.66(16) \times 10^9$ ^{88}Sr atoms/s (measured by absorption imaging) and cools atoms to about 1 mK in the radial (xz) plane. To prevent atoms from escaping
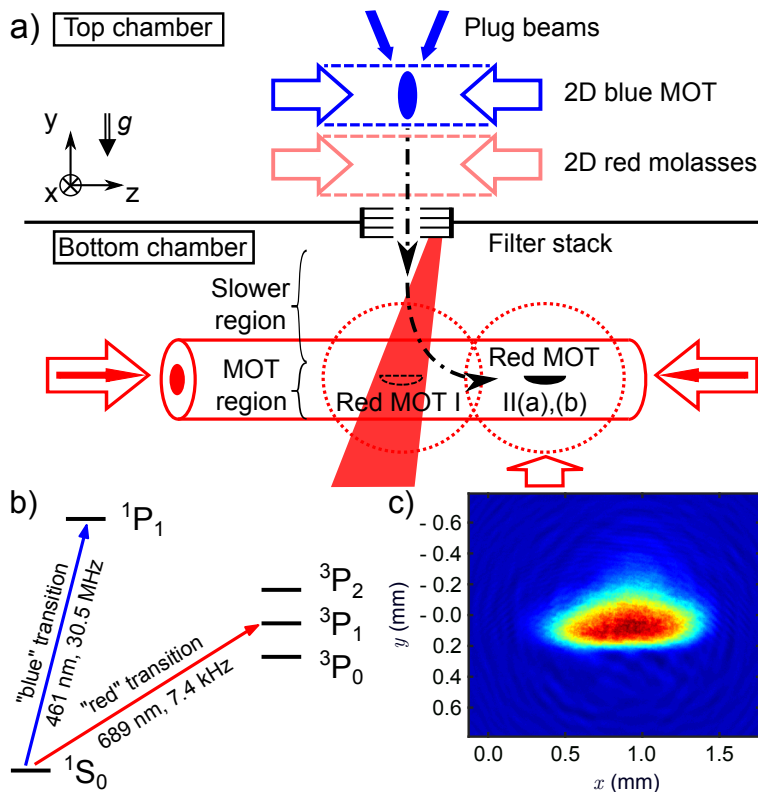
FIGURE 3.1: a) Schematic of our setup, showing the main cooling stages, and the position of the three "red" MOT configurations (see text). b) Electronic level scheme of strontium, with the "blue" and "red" transitions used for laser cooling. c) In situ absorption picture of a steady-state ^{88}Sr MOT with a PSD of $1.3(2) \times 10^{-3}$ (Red MOT II(b) configuration).

upward, a pair of downward propagating blue "plug" beams are placed symmetrically to each other at an $8°$ angle from the y axis, increasing the flux by around 30%.

The high phase-space density MOT must be operated on the narrow-linewidth red transition while being protected against photons from the broad-linewidth blue transition [94]. In order to ensure such protection, we position the red MOT in a separate chamber, $41\,\mathrm{cm}$ below the 2D blue MOT. The two chambers are separated and baffled by a set of four stacked 1-inch absorptive neutral density filters (Thorlabs NE60A). These filters are separated by $20\,\mathrm{mm}$ and have an $8\,\mathrm{mm}$ diameter center hole allowing atoms to pass.

Upon exiting the 2D blue MOT, atoms have a radial velocity of about $0.5\,\mathrm{m/s}$, an average downward velocity of $3\,\mathrm{m/s}$ (see Section 3.5.2), and they fall accelerated by gravity towards the bottom chamber. Radial expansion during the $185\,\mathrm{mm}$ drop to the bottom of the baffle section would give a transfer efficiency less than 2%. Accelerating the atoms downward is out of the question, since we can only use the

low capture velocity red transition in the bottom chamber. Instead, we radially cool atoms emerging from the 2D MOT using a 2D molasses operating on the red $^1S_0$ - $^3P_1$ π transition, which is insensitive to the spatially varying magnetic field. To compensate the Doppler broadening of the atomic transition, which is more than 100 times the 7.4 kHz natural linewidth, it is necessary to modulate the frequency of the molasses laser beams forming a frequency comb spanning from 30 to 750 kHz to the red of the transition, with 25 kHz spacing [103]. This technique is used on all our red-transition laser beams. To prevent the two red $^1S_0$ - $^3P_1$ σ transitions towards the $m_{J'} = \pm 1$ states from hindering the radial slowing process, we produce a Zeeman shift of about 3 MHz by applying a bias magnetic field of 1.4 G in the vertical direction. Such a small field doesn't disturb the operation of the 2D blue MOT. This molasses reaches steady state after a few 10 ms, easily provided by four horizontal molasses beams with $1/e^2$ diameters of 45.6 mm along the y axis.

After a 41 cm fall from the top to the bottom chamber, the atomic beam has a measured downward velocity distribution peaked at 4 m/s. Our protection scheme necessitates slowing and capturing these falling atoms using only the red transition. However, the small scattering rate on this line allows a maximum deceleration of only $\sim 16\, g$, where g is earth acceleration. To overcome this extreme limitation we implement a hybrid slower+MOT.

Our first hybrid setup configuration labeled "Red MOT I" (see Figure 3.1a) uses a magnetic quadrupole field centered 23 cm directly below the bottom baffle between chambers. The gradients are $(0.55, 0.35, 0.23)$ G/cm in the (x, y, z) directions. Horizontally propagating laser beams in the x, z axes are placed in a MOT configuration and provide radial cooling and confinement. On the y axis, a single, upward propagating beam is used, with circular polarization as needed for the MOT. Due to the weakness of the transition this upward propagating beam and gravity are sufficient to confine atoms in the vertical direction without a downward propagating MOT beam [108]. The vertical beam is directed slightly to the side of the baffle onto the lowest neutral density filter, to prevent it from affecting the cooling processes in the top chamber. This beam is converging to exert a restoring force towards the beam center during the slowing process [109].

Upon reaching the second chamber, atoms enter the region illuminated by the circularly-polarized upward-propagating beam, whose frequency is set to the red of the $^1S_0 - ^3P_1$ transitions. We now describe the slowing process using an upward pointing quantization axis, see Figure 3.2a. The Doppler shift $\delta_{\mathrm{Doppler}}(v)$ of atoms with

a downward velocity v brings them into resonance with the σ^+ transition from $^1S_0$ to the state $m_{J'} = +1$ of $^3P_1$. As radiation pressure slows atoms down, $\delta_{\mathrm{Doppler}}$ diminishes, which is partially compensated by the spatial variation of the magnetic field, following the principle of a Zeeman slower. The narrow linewidth of the red transition does not allow for a slowing process robust against magnetic and laser intensity fluctuations, so we modulate the laser frequency ν_L with a span of $\Delta\nu_L = 4.05\,\mathrm{MHz}$, as used for example in "white light" slowing [110]. If atoms are successfully slowed and reach the region below the quadrupole field center, $\delta_{\mathrm{Doppler}}$ is small and atoms are resonant with the laser light as in a standard broadband narrow-line MOT [93]. Note that for the experimental configurations used the angle between the local magnetic field and the beam direction can be big, leading to significant additional absorption on the π transition during the slowing process.

3.3 Results and discussion

We numerically model this hybrid setup by evolving classical atomic trajectories, first in an idealized 1D geometry with only a linear vertical magnetic field gradient and a uniform circularly polarized vertical beam, and then using a Monte Carlo approach in a realistic 3D geometry including all beams and details of the magnetic fields (see Section 3.5.4). The behavior of a falling atom can be obtained by analyzing the deceleration it experiences in dependence of time when dropped into the slower+MOT region with various starting velocities. The idealized 1D results shown in Figure 3.2b are qualitatively confirmed by the more realistic 3D model results shown in Figure 3.2c. With these simulations we estimate a maximum capture velocity of around 6 m/s for the hybrid slower+MOT setup, which is compatible with the measured velocity distribution of the atomic beam produced by the 2D blue MOT (see Section 3.5.2).

The characteristics of the hybrid Red MOT I are summarized in Table 3.1. The loading rate gives an estimated transfer efficiency of $19\,\%$ between the two chambers. Unfortunately, the high power broadband beams needed for the hybrid setup limit the PSD to $2.8(1.2) \times 10^{-6}$, low compared to what can be achieved with a pure red MOT geometry in a time-varying sequence [93]. Moreover, with direct line-of-sight to a bright fluorescing blue MOT, this configuration does not provide protection against heating from blue photons sufficient to produce a steady-state BEC (see Section 3.5.3).
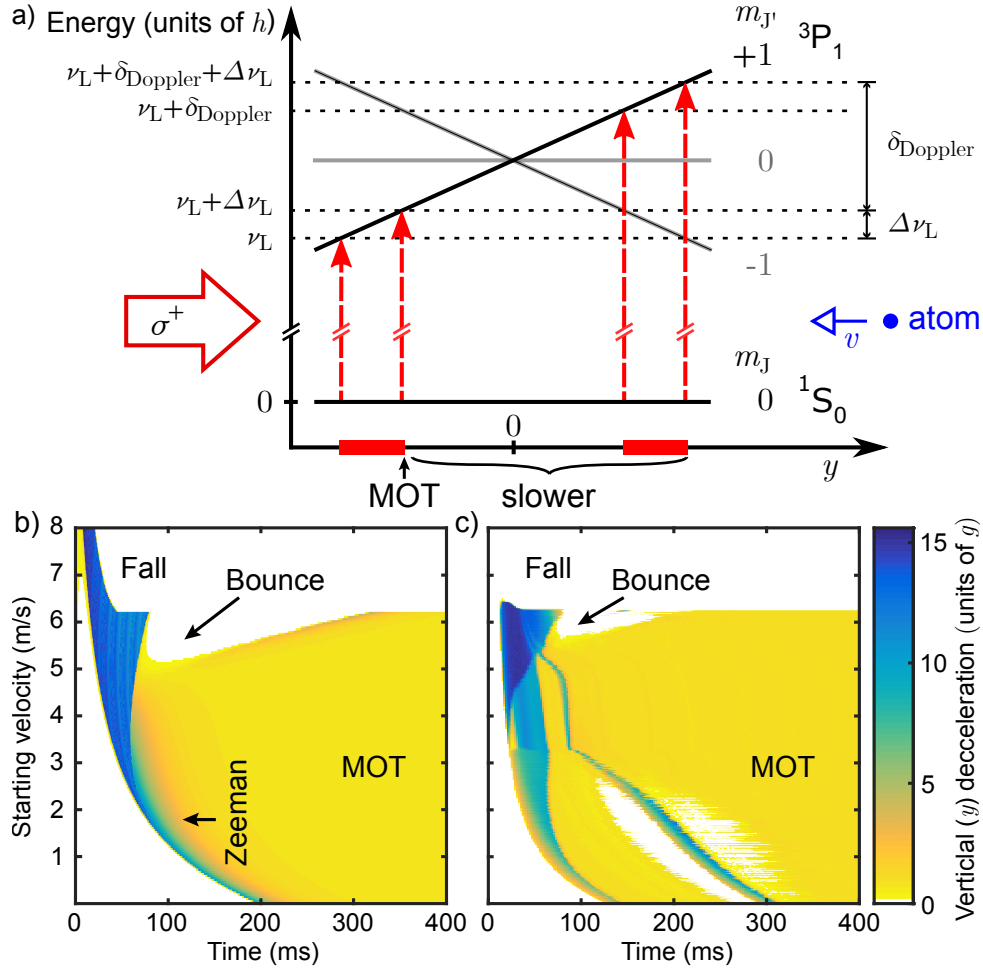
FIGURE 3.2: Working principle of the hybrid slower+MOT in Red MOT I configuration. a) Energy diagram of the $^1\mathrm{S}_0, m_\mathrm{J}$ and the $^3\mathrm{P}_1, m_{\mathrm{J}'}$ states in dependence of y for $x = z = 0$, where the coordinate origin lays in the quadrupole field center. An atom with velocity $v \neq 0$ along the y axis is addressed by the upward-propagating Red MOT I beam in a region delimited by the pair of red dashed arrows on the right. The range of this region is determined by the span of the laser frequency modulation $\Delta\nu_\mathrm{L}$ and the magnetic field gradient. An atom with $v = 0$ is addressed in the region delimited by the pair of dashed arrows on the left. b) y deceleration from scattering of photons on the red transition (in units of earth acceleration g) in dependence of the initial velocity of atoms 20 cm above the quadrupole field center, obtained by an idealized 1D calculation. A horizontal path across the diagram corresponds to a 1D time-dependent trajectory along y. Annotations indicate regions dominated by Zeeman type slowing or red MOT type trapping. Atoms eventually captured in the MOT exhibit a time-independent non-zero force (yellow region at $\sim 1g$). The white regions show decelerations smaller than $0.25g$. The "Bounce" and "Fall" regions are undesirable cases described in (see Section 3.5.4). c) Equivalent deceleration data obtained by a full 3D Monte Carlo calculation with a realistic geometry.

TABLE 3.1: Characteristics of the three Red MOT configurations. All uncertainties stated in this letter are taken as $\pm 2\sigma$ from the fitted data.

	Red MOT I	Red MOT II(a)	Red MOT II(b)
Flux [^{88}Sr/s]	$5.1(7) \times 10^8$	$5.3(4) \times 10^7$	$5.3(9) \times 10^6$
Temperature x	-^{1}	$3.7(3)\,\mu\text{K}$	$2.01(6)\,\mu\text{K}$
Temperature y	$20(5)\,\mu\text{K}$	$1.9(1)\,\mu\text{K}$	$1.42(3)\,\mu\text{K}$
Temperature z	$26(7)\,\mu\text{K}$	$2.8(2)\,\mu\text{K}$	$1.91(9)\,\mu\text{K}$
Width σ_x	-^{1}	$385(4)\,\mu\text{m}$	$150(2)\,\mu\text{m}$
Width σ_y	$725(61)\,\mu\text{m}$	$192(3)\,\mu\text{m}$	$88(1)\,\mu\text{m}$
Width σ_z	$2086(41)\,\mu\text{m}$	$528(3)\,\mu\text{m}$	$247(3)\,\mu\text{m}$
Atom number [^{88}Sr]	$2.54(10) \times 10^9$	$1.71(5) \times 10^8$	$2.5(1) \times 10^7$
Peak density [^{88}Sr/cm^3]	$5.1(7) \times 10^{10}$	$2.8(2) \times 10^{11}$	$4.8(4) \times 10^{11}$
Peak PSD	$2.8(1.2) \times 10^{-6}$	$4(1) \times 10^{-4}$	$1.3(2) \times 10^{-3}$
$1/e$ lifetime	$4.53(6)\,\text{s}$	$2.8(2)\,\text{s}$	$1.95(6)\,\text{s}$

For these reasons, we implement a second MOT configuration, "Red MOT II(a)", located $3\,\text{cm}$ in the z direction away from the Red MOT I position (see Figure 3.1a). This is achieved by adding another 5-beam geometry MOT (4 beams along x and z, 1 beam along y), whose beams make a smooth connection with the Red MOT I beams, and by displacing the center of the quadrupole field to the intersection of these new beams. Along the z axis the two additional beams are implemented as an $8\,\text{mm}$ diameter low-intensity core within hollow $48\,\text{mm}$ diameter Red MOT I beams. In this configuration, atoms entering the second chamber are decelerated by the hybrid slower plus Red MOT I beams, then continuously pushed to the Red MOT II(a) where they are confined and further cooled. The working principle of the hybrid setup remains unchanged, with the exception that the π transition becomes more important, since the magnetic field lines are more tilted with respect to the Red MOT I vertical beam.

Within this second red MOT, we have more freedom to adapt the beam parameters and thereby reach higher PSD. The main limitations to the PSD are firstly power broadening of the red transition effectively raising the Doppler cooling limit and secondly multiple scattering due to the high density. Both limitations recede with reduced MOT powers. For this reason, we implement a spectrally dark SPOT MOT by shaping the spectral intensity profile of our broadband MOT beams. At the steady-state MOT location, the effective scattering rate is just enough to hold atoms against gravity, while in the surrounding region an effective high optical power captures fast atoms.

With Red MOT II(a) using the parameters given in Table 3.1, we reach a

steady-state MOT with a PSD of $4(1) \times 10^{-4}$ for ^{88}Sr. The transfer efficiency from the top chamber to this MOT is 2%, an order of magnitude lower than for Red MOT I. Simulations suggest significant losses may be attributed firstly to increased bouncing of atoms in the hybrid slower when the π transition is dominant and secondly to atom trajectories intersecting with mirrors inside the vacuum chamber.

We also produce a Red MOT II(a) using the much less abundant ^{84}Sr isotope, which is particularly suited to produce quantum degenerate gases, owing to its favorable scattering properties. This ^{84}Sr MOT contains up to $9.0(2) \times 10^{6}$ atoms at temperatures of $1.5(3)\,\mu$K and $3.4(1.1)\,\mu$K in the vertical and horizontal axes respectively. By loading this MOT into an optical dipole trap in a time sequential manner and applying a $3\,$s evaporative cooling sequence, we produce ^{84}Sr BECs of $3.0(2) \times 10^{5}$ atoms.

The protection provided by the dual chamber and baffle system against photons from the broad-linewidth blue transition is determined by comparing the BEC lifetime at the location of the Red MOT II(a) with and without the 2D blue MOT operating. The atomic flux is disabled by turning off the red transition beams during these measurements. The BEC lifetime in the dipole trap is $3.0(4)\,$s without blue light and $2.7(2)\,$s with blue light. Lifetimes were strongly limited by one-body collisions due to poor vacuum quality. These measurements confirm significant protection from blue photons thanks to our two-chamber design, making our system suitable for experiments aimed at developing a steady-state source of degenerate quantum gas.

Finally, "Red MOT II(b)" is a configuration designed to optimize phase-space density at the expense of transfer efficiency. This MOT reaches a steady-state PSD of $1.3(2) \times 10^{-3}$ for ^{88}Sr, which is two orders of magnitude higher than demonstrated in previous steady-state MOTs [96] (see Figure 3.1c and Table 3.1). Red MOT II(b) is the same as Red MOT II(a) except that we reduce the bandwidth of the MOT II beams to cover only -40 to -200 kHz detuning, resulting in three improvements. First, the smaller detuning of -40 kHz compresses the MOT, second, the reduced bandwidth reduces the total beam intensity required, and third, by ending the spectrum well before the photoassociation line located at -435 kHz detuning [46], we reduce losses due to molecule formation. The transfer efficiency from the top chamber to this MOT is 0.2%, an order of magnitude lower than for Red MOT II(a). The $1/e$ lifetime of Red MOT II(b) measured after the atomic flux is suddenly stopped is 1.95(6) s, which is significantly smaller than the 4.53(6) s lifetime of Red MOT I. This reduction is due to two-body light-assisted collisions, which ultimately limits the maximum density

achievable [46]. Both these losses and the need to compensate for gravity set the limits on the PSD achievable with this MOT configuration.

3.4 Conclusions

To summarize, we have demonstrated the operation of a MOT with a PSD of $1.3(2) \times 10^{-3}$ in the steady-state regime. This result requires the use of broad- and narrow-linewidth transitions to simultaneously achieve both high PSD and high capture efficiency. We use a dual chamber architecture to protect the MOT from heating by broad-linewidth transition photons, and efficient transfer between chambers is achieved using a hybrid slower+MOT configuration using only cooling on the narrow-linewidth transition. Although Sr is ideally suited to this architecture, our approach is broadly applicable to alkaline-earth metals, lanthanides and any other species with a strong transition to precool atoms and a weak transition supporting the operation of a MOT with a high PSD [111, 112]. Finally, we have shown that our design is compatible with the generation of quantum degenerate gases in the presence of a laser cooled influx. The use of this high-PSD source of matter, combined with a protection mechanism such as that demonstrated in [11], should allow the creation of a steady-state Bose-Einstein condensate and ultimately an atom laser with uninterrupted phase coherent output.

3.5 Supplemental Material

3.5.1 Details of the experimental setup
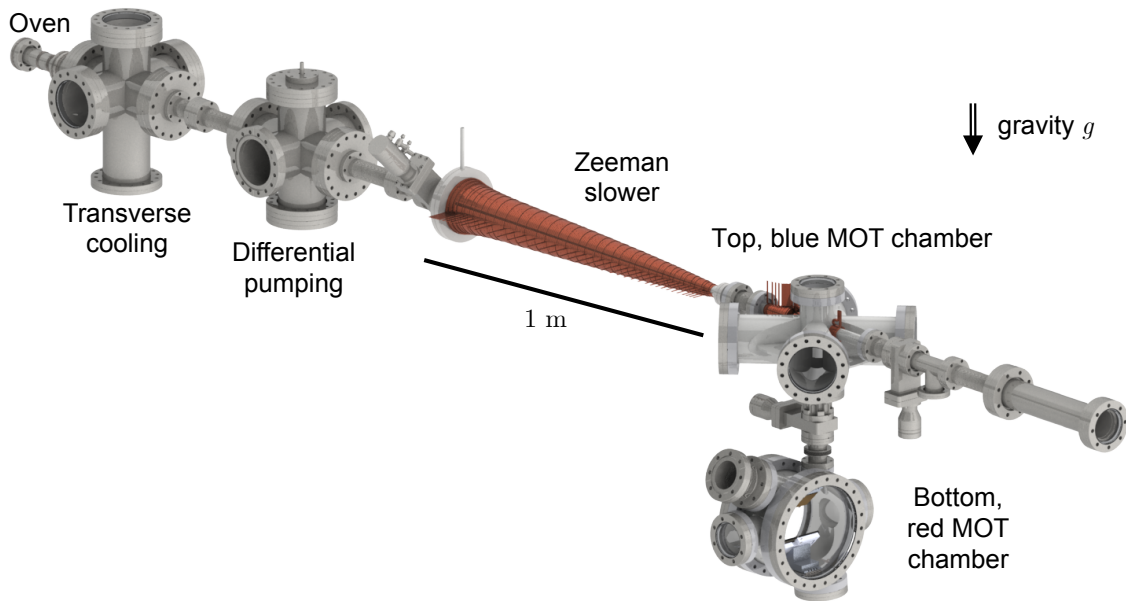
FIGURE 3.3: CAD drawing of the machine excluding vacuum pumping sections.

The atomic source is an oven producing a 10 mm diameter effusive jet of strontium atoms by heating Sr metal pieces (99.5 % from Alfa Aesar) to around 500 °C. While the oven was designed to operate at 550 °C for 18 months it is currently operated at only 500 °C as this has been found to deliver sufficient flux and will extend the operating life before needing to refill the Sr reservoir and rebake the oven section of the vacuum system. Increasing the temperature to 550 °C is expected to increase the flux by a factor of five, an important option when working with 0.5 % abundant ^{84}Sr. The oven output is collimated by an array of 8 mm long stainless steel microtubes with 80 μm inner diameter and 180 μm outer diameter, following a design inspired by [104]. The atoms are then transversely cooled in two dimensions over a 90 mm long region using for each axis a "zig-zag" configuration with four passes and retro-reflection of the laser beam. Finally a 105 cm long Zeeman slower, with a spin-flip design and a modeled maximum capture velocity of 500 m/s, slows the atoms to approximately 20 m/s.

The Zeeman slower output is captured by a 2D MOT using the blue 461 nm transition. The 2D MOT magnetic field gradient is created by two vertical permanent magnet arrays, facing each other with opposite pole orientation. The position and

TABLE 3.2: Properties of laser cooling beams using the blue $^1S_0 - {}^1P_1$ transition.

Beam name	Detuning [MHz]	Power [mW]	$1/e^2$ diameter [mm]	Comments
Transverse cooling	$-18\,(-0.6\Gamma)$	30	23×9.6	Beam is passed 4 times side by side giving a 90 mm long cooling region. Same for both horizontal and vertical axes.
Zeeman slower	$-424\,(-14\Gamma)$	64	25.4	Focused to 12 mm diameter at the oven exit.
2D MOT	$-25\,(-0.8\Gamma)$	10.5	22.8	4 beams with centers at the same height as the Zeeman slower axis.
Plug beams	$-13\,(-0.4\Gamma)$	0.017	9.6	2 symmetric beams inclined at $8\,°$ to the vertical (y axis) and aimed at the top half of the blue 2D MOT.

TABLE 3.3: Properties of laser beams used for Red MOT I. Under "detuning" $\Delta_1 : \delta : \Delta_2$ refers to a modulated comb of lines from Δ_1 to Δ_2 with a spacing of δ.[1]

Beam name	Detuning [MHz]	Power [mW]	$1/e^2$ diameter [mm]	Comments
2D Red molasses	-0.03 : 0.025 : -0.75	4.6	45.6×18.2	2 sets of 2 counter-propagating beams, centered 38 mm below Zeeman slower plane.
Red MOT I Y	-0.95 : 0.017 : -5	10.8	68	Waist given 22 cm below the quadrupole center. Beam focused on the bottom baffle 22 cm above the quadrupole center at $z = +10$ mm from the central axis of the falling atomic beam.
Red MOT I X	-0.7 : 0.015 : -3	3.3	47	2 counter-propagating beams
Red MOT I Z Outer	-0.7 : 0.016 : -3	1.14	48	2 counter-propagating beams with an 8mm hole to allow Red MOT I Z Inner beams to pass.
Red MOT I Z Inner	-0.73 : 0.017 : -1.1 -1.1 : 0.019 : -3.5	0.16[1]	8	2 counter-propagating beams

orientation of individual magnets stacked in each array can be independently adjusted to produce the desired radial gradient, which is approximately 10 G/cm in the region of the blue MOT and rapidly transitions to approximately 2 G/cm over about 15 mm. Helmholtz bias coils are used to trim the pointing and location of the 2D MOT in order to maximize capture by the 3D red MOT in the second chamber. Other details are described in the main text and illustrated in Figure 3.3. The parameters of all the beams for laser cooling on the blue transition are listed in Table 3.2. The parameters of the beams used for Red MOT I, Red MOT II(a) and Red MOT II(b) are listed in Table 3.3, Table 3.4 and Table 3.5, respectively.

TABLE 3.4: Properties of laser beams used in the apparatus for Red MOT II(a). Under "detuning" $\Delta_1 : \delta : \Delta_2$ refers to a modulated comb of lines from Δ_1 to Δ_2 with a spacing of δ.

Beam name	Detuning [MHz]	Power [mW]	$1/e^2$ diameter [mm]	Comments
2D Red molasses	-0.03 : 0.025 : -0.75	4.6	$45.6 \times$ 18.2	2 sets of 2 counter-propagating beams, centered 38 mm below Zeeman slower plane.
Red MOT I Y	-0.5 : 0.017 : -4	10.8	68	Waist given 22 cm below the quadrupole center. Beam focused on the bottom baffle 22 cm above the quadrupole center at $z = +10$ mm from the central axis of the falling atomic beam.
Red MOT I X	-0.7 : 0.015 : -3	3.3	47	2 counter-propagating beams
Red MOT I Z Outer	-0.7 : 0.016 : -4	1.14	48	2 counter-propagating beams with an 8mm hole to allow Red MOT II Z Inner beams to pass.
Red MOT II Z Inner	-0.1 : 0.017 : -0.25 -0.26 : 0.015 : -2.85	0.063[1]	8	2 counter-propagating beams
Red MOT II Y	-0.1 : 0.016 : -0.25 -0.26 : 0.014 : -2.85	0.43[1]	36	1 upward-propagating beam
Red MOT II X	-0.1 : 0.017 : -0.25 -0.26 : 0.013 : -2.85	0.099 [1]	28.8	2 counter-propagating beams

TABLE 3.5: Properties of laser beams used in the apparatus for Red MOT II(b). Under "detuning" $\Delta_1 : \delta : \Delta_2$ refers to a modulated comb of lines from Δ_1 to Δ_2 with a spacing of δ.

Beam name	Detuning [MHz]	Power [mW]	$1/e^2$ diameter [mm]	Comments
2D Red molasses	-0.03 : 0.025 : -0.75	4.6	$45.6 \times$ 18.2	2 sets of 2 counter-propagating beams, centered 38 mm below Zeeman slower plane.
Red MOT I Y	-0.5 : 0.017 : -4	10.8	68	Waist given 22 cm below the quadrupole center. Beam focused on the bottom baffle 22 cm above the quadrupole center at $z = +10$ mm from the central axis of the falling atomic beam.
Red MOT I X	-0.7 : 0.015 : -3	3.3	47	2 counter-propagating beams
Red MOT I Z Outer	-0.7 : 0.016 : -4	1.14	48	2 counter-propagating beams with an 8mm hole to allow Red MOT II Z Inner beams to pass.
Red MOT II Z Inner	-0.04 : 0.017 : -0.2	0.016	8	2 counter-propagating beams
Red MOT II Y	-0.04 : 0.016 : -0.2	0.09	36	1 upward-propagating beam
Red MOT II X	-0.04 : 0.017 : -0.2	0.026	28.8	2 counter-propagating beams

3.5.2 Velocity distribution from the 2D Blue MOT

The atoms exiting the Zeeman slower enter the 2D MOT region. Due to the broad linewidth of the blue transition, they are rapidly cooled to about $1\,\mathrm{mK}$ in the radial direction, but are presumably unaffected in the 2D MOT, vertical axis. The velocity distribution along this axis depends mostly on the oven output collimation, the transverse cooling stage, and the transverse spread due to scattering from the Zeeman slower beam. This last contribution amounts to about 5×10^4 spontaneously emitted photons, which gives an energy increase in the slower transverse direction of $\sim 15\,\mathrm{mK}$, part of which will affect the vertical velocity distribution.

Aiming to measure the vertical velocity distribution, we place two cylindrical $4\,\mathrm{mm}$ $1/e^2$-diameter high by $16\,\mathrm{mm}$ $1/e^2$-diameter wide "gate" beams in the top chamber, which are actuated by fiber coupled acousto-optic modulator "switches" and centered $40.8\,\mathrm{mm}$ and $70.8\,\mathrm{mm}$ below the plane of the Zeeman slower. Each beam uses approximately $2\,\mathrm{mW}$ of light resonant with the blue transition to "blow away" any atoms attempting to travel to the bottom chamber. By sequentially opening these blocking beams a known velocity class can be selected. We find that opening any one beam for less than $5\,\mathrm{ms}$ (with the other beam off) results in no atoms transmitted to the lower chamber, so we use a $6\,\mathrm{ms}$ gate opening time resulting in an effective opening time of $1\,\mathrm{ms}$. Atoms are collected in Red MOT I and then compressed by ramping up the gradient and decreasing the detuning to give a cloud dense enough to reliably measure the atom number using absorption imaging. By scanning the time between the opening of the two gate beams, we measure the velocity distribution of the atomic beam emanating from the top chamber that is capturable by Red MOT I, see Figure 3.4.

3.5.3 Heating from blue MOT photons

We now estimate the heating of Red MOT I by the scattering of fluorescence photons from the 2D blue MOT. The minimum scattering rate from atoms in a red MOT that is required to counter acceleration due to gravity is $\gamma_\mathrm{min} = mg/\hbar k$, where m is the atom mass, $\hbar$ is the reduced Planck constant and k is the photon wavenumber. Considering a blue transition photon scattering rate of $20\,\%$ of γ_min as acceptable, we can estimate the maximum allowable intensity of the blue photon flux at the location

---

[1]Note that due to nonlinearities in the amplifiers and AOMs, it is not possible to separately measure the optical powers in each component of the spectrum.
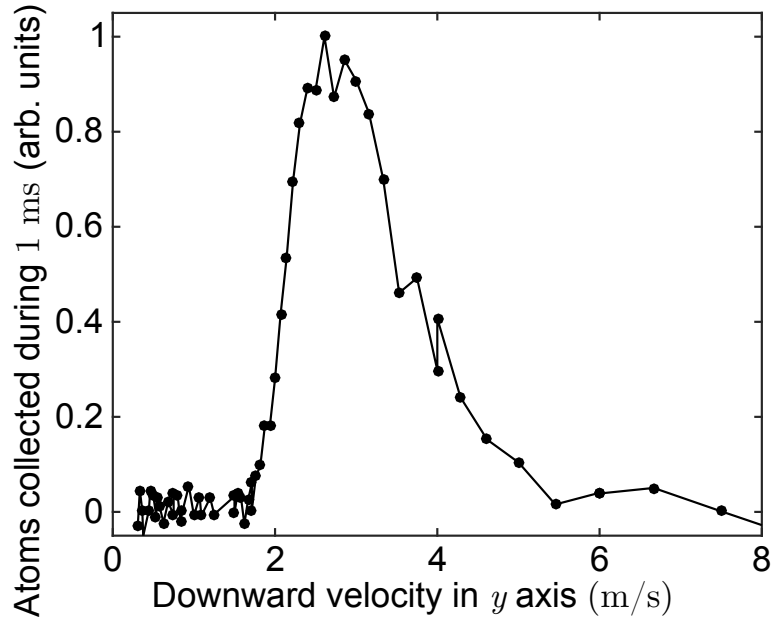
FIGURE 3.4: Velocity distribution of the atomic beam emitted downward by the blue 2D MOT and captured by Red MOT I, given for atoms located $55\,\mathrm{mm}$ below the plane of the Zeeman slower.

of the red MOT, $I_{\mathrm{max}} \approx 0.2 \times 2\gamma_{\mathrm{min}} I_{\mathrm{sat,blue}}/\Gamma_{\mathrm{blue}} \approx 0.13\,\mu\mathrm{W/cm^2}$, with $I_{\mathrm{sat,blue}}$ and Γ_{blue} being the saturation intensity and the natural linewidth of the blue transition, respectively. Our blue MOT with optical frequency ν_{blue} has a flux of $F \approx 2.5 \times 10^9\,\mathrm{atoms/s}$ and atoms spend around $t_{\mathrm{blue}} \approx 20\,\mathrm{ms}$ passing through the blue MOT. The intensity of the blue MOT light is $I_{\mathrm{MOT}} \approx I_{\mathrm{sat,blue}}/4$. The power scattered by the 2D blue MOT is thus $P = Ft_{\mathrm{blue}}\,h\nu_{\mathrm{blue}}\,\Gamma_{\mathrm{blue}}/2\,I_{\mathrm{MOT}}/(I_{\mathrm{sat,blue}}(1 + I_{\mathrm{MOT}}/I_{\mathrm{sat,blue}})) \approx 4.1 \times 10^{-4}\,\mathrm{W}$. If we ignore all other sources of blue transition photons such as scattering off the chamber surfaces and windows, and consider only scattered light from the 2D MOT atoms, we need a minimum distance r of $r > \sqrt{P/(4\pi I_{\mathrm{max}})} \approx 16\,\mathrm{cm}$ to reduce heating in the red MOT to an acceptable level. For the production of a degenerate gas where we require a scattering rate below $1\,\mathrm{Hz}$ for a reasonable lifetime, the corresponding distance is $r > 2.8\,\mathrm{m}$. This effectively requires there be no line of sight between a BEC and the 2D blue MOT, or any surface scattering light from the blue MOT, which dictates our apparatus design.
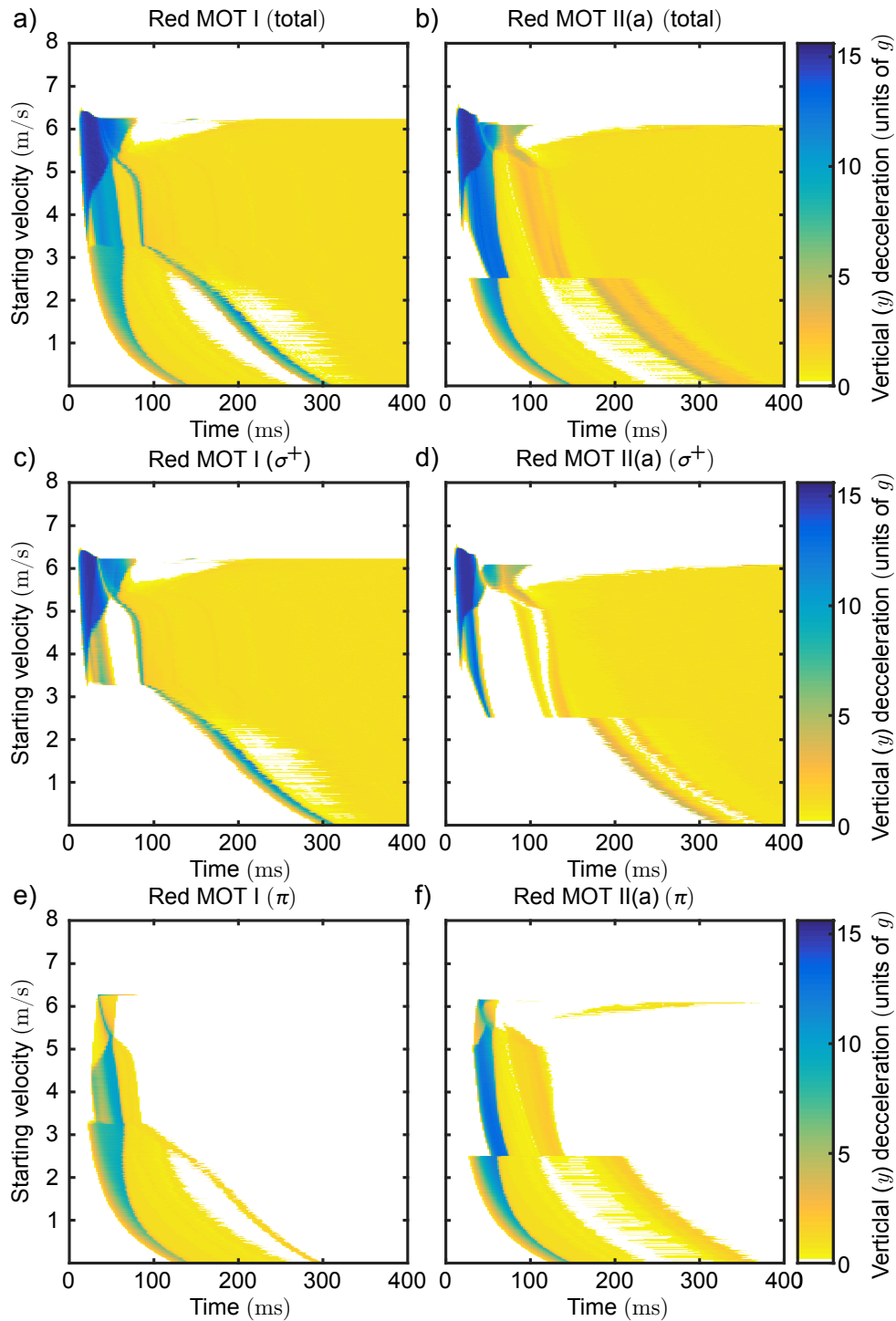
FIGURE 3.5: Monte Carlo numerical simulations of the hybrid slower+MOT. In these simulations, atoms start to fall from the center of the bottom baffle between the chambers, approximately $20\,\mathrm{cm}$ above the quadrupole center in the case of Red MOT I, with only a downward, y velocity component, which is indicated on the vertical axis. The horizontal axis corresponds to time during 1D trajectories along y. (left) Scattering in the Red MOT I configuration and (right) scattering in the Red MOT II(a) configuration. (a-b) Total scattering rate (in units of gravity g), (c-d) scattering from the σ^+ (MOT and Zeeman) and (e-f) scattering from the π (non magnetic) components separated. The white regions show decelerations smaller than $0.25g$.

3.5.4 Numerical model results

We now describe the behavior of the hybrid slower+MOT setup, based on our numerical simulations. The results for the 1D idealized situation have already been presented in Figure 2b of the Letter and the 3D Monte Carlo simulations are shown in Figure 2c of the Letter and Figure 3.5. The 3D simulations begin with atoms released from the center of the aperture in the bottom baffle approximately $20\,\mathrm{cm}$ above the quadrupole field center in the case of Red MOT I, and with only a y velocity component. The atoms are then allowed to fall under gravity and experience radiation pressure from the various laser beams and heating from spontaneous emission. Spontaneous emission heating is modeled as a lumped impulse in a random direction proportional to the root of the net radiation impulse absorbed.

In the idealized case, for a low starting velocity $20\,\mathrm{cm}$ above the quadrupole field center (below $5\,\mathrm{m/s}$), the falling atoms first experience a Zeeman slower-like deceleration on the σ^+ transition with a scattering rate close to $\Gamma_\mathrm{red}/2$, where Γ_red is the natural linewidth of the red $^1\mathrm{S}_0 - {}^3\mathrm{P}_1$ transition. This scattering rate corresponds to a deceleration of about $16\,g$ (blue-colored region in Figure 2b of the letter). As atoms keep decelerating, the Doppler shift δ_Doppler diminishes and a combination of the Zeeman effect and the broadening $\Delta\nu_\mathrm{L}$ of the laser beam frequency dictates the scattering rate at each spatial location. Eventually atoms are almost at rest in the vertical direction and δ_Doppler becomes negligible. Atoms thus behave like in a standard broadband MOT, and they reach the height where the radiation pressure compensates exactly gravity, typically at the top of the spatial region addressed by the broadband MOT (yellow-colored region labeled "MOT" in Figure 2b and c of the letter). These atoms are thus captured in the MOT.

For medium starting velocities (between 5 and $6.2\,\mathrm{m/s}$ in the idealized case) the atoms' scattering is saturated for most of the time, until atoms are stopped in the vertical direction. This happens at a location deep within the region addressed by the broadband MOT. As a consequence, the scattering rate is way more than what is necessary to compensate gravity, and the hybrid setup acts as a spring and makes the atoms bounce up (see region labeled "Bounce" in Figure 2b and c of the letter). The relatively weak gravitational force is the only mechanism to push them downward. The simulations indicate that most atoms having bounced will then fall back into the MOT region and get captured there, provided they do not reach surfaces of the vacuum chamber. The horizontal confinement provided by Red MOT I X and Z beams is instrumental to this purpose.

For high starting velocities (above $6.2\,\mathrm{m/s}$ in the idealized case), the saturated scattering is insufficient to provide enough deceleration for the atoms before they reach the bottom of the spatial region addressed by the broadband MOT, and they are not captured (region labeled "Fall" in Figure 2b and c of the letter).

The main difference between the idealized case and the more realistic 3D simulation results is the influence of the π transition. Due to the tilted magnetic field orientation with respect to the hybrid vertical slower beam, a large part of the interaction occurs on the non-magnetic π transition and the σ^+ Zeeman slower-like transition is less important, as shown in Figure 3.5. Moreover, two main extra features appear in the results of the 3D simulations. The first is the disappearance of scattering for starting velocities above $6.5\,\mathrm{m/s}$, which limits the maximum capture velocity. This originates from the Red MOT I vertical beam frequency boundaries, in combination with its location. Indeed, because of the tilt we apply to the beam in order to hit the side of the bottom baffle, the fastest atoms enter the beam location only after having passed the spatial region where the light is on resonance with the slowing transitions, and thus they are never decelerated. The second feature is the kink in scattering rate appearing for starting velocities of $3.2\,\mathrm{m/s}$ for Red MOT I and $2.5\,\mathrm{m/s}$ for Red MOT II(a). This arises when atoms enter the vertical slower beam with a velocity smaller than the minimum velocity addressed by the σ^+ transition but within the frequency range of the π transition. In this case atoms are slowed entirely by the π transition before falling at the maximum velocity allowed by the π transition into the MOT region.

Chapter 4

Steady-state Ultracold Sr near Quantum Degeneracy

4.1   Introduction

Continuous cold atomic beams have been pursued for fundamental physics endeavors such as attempts to develop the first continuous atom laser and ultrahigh resolution spectroscopy, but also for applied systems like sources for high brightness and focused ion beams [113, 114]. More recently, interest has grown in applications like atom interferometry for precision measurement [115, 116], sympathetic cooling and cold chemistry [117, 118] although these have typically focused on developing pulsed sources due to the relative ease of developing high phase-space density (PSD) samples in a time-sequential process.

Various properties of an atomic beam, such as the total flux, brightness, and phase-space density are of interest depending on the application. In 2004, Lahay et al. [30] reached a PSD of 10^{-7} by continuously coupling rubidium atoms from a MOT into a 7 m long magnetic waveguide in which they were evaporatively cooled. A similar approach with a much more compact spiral waveguide design was pursued by Raithel [119]. Pfau et al. [31] used a moving molasses to couple chromium atoms into an 1 mK deep dipole trap waveguide with transverse laser cooling to reach a phase-space density of 10^{-8}.

Although many architectures have been developed, most so far produce beams with extremely poor center-of-mass peak phase-space density, which eventually poses limitations for future applications. For example, a higher brightness or PSD of the atomic beam is desired to obtain a smaller spot size for a focused ion beam based on an ultracold beam source. In metrology, to overcome the Dick effect caused by the dead time during which the samples are prepared, a continuous source for a

(a)

(b)

(c)
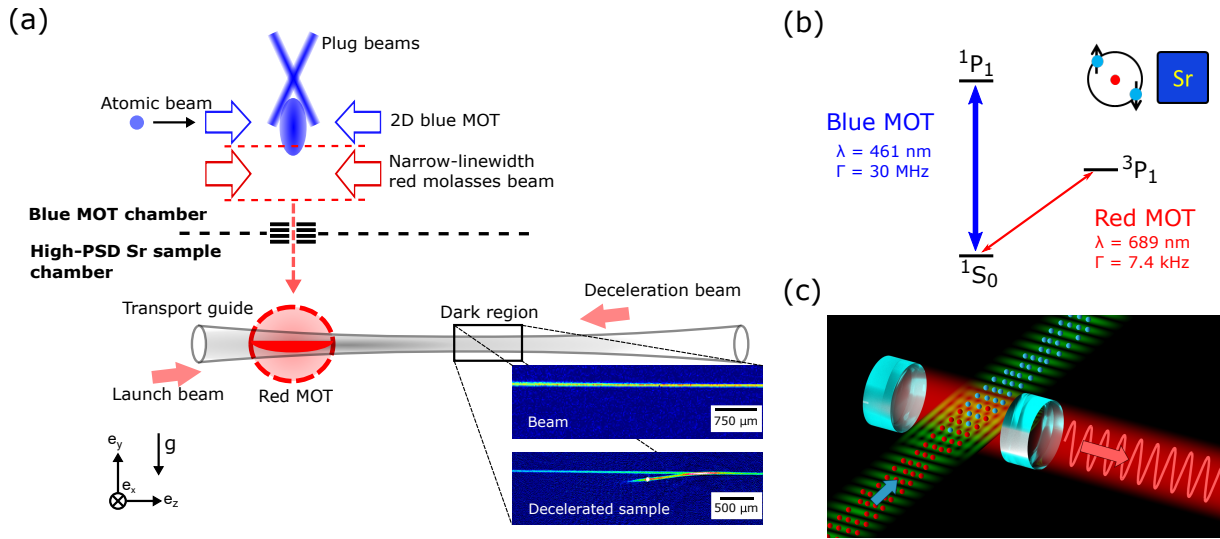
FIGURE 4.1: (a) Schematic of the steady-state ultracold Sr beam setup. Laser cooling steps are implemented sequentially in space. (b) Two main cooling transitions are both utilized in this steady-state cooling setup. The broad transition is employed where high declaration is needed: to convert a hot atomic beam from an oven into a $\sim 1\,\mathrm{m/s}$ slow beam sent from the "Blue MOT chamber" to the "High-PSD Sr sample chamber". The intercombination line does only provide small deceleration (up to 15 g), but allows cooling to the μK range. (c) One prospective application of our beam source is to continuously replenish atoms in a superradiant laser cavity.

high-PSD beam is in demand. Another noteworthy application, a high-PSD atomic beam could be a continuous atom replenishing source for a superradiant (bad cavity) laser. Such type of laser can be extremely stable, because in this system the information about the phase is stored in the atoms instead of the photons, and therefore immune to thermal fluctuations of the cavity mirror. A high-PSD atomic beam is instrumental for converting a so-far pulsed, Fourier-transform limited superradiant laser into steady-state operation, ultimately reaching a coherence time fundamentally limited by the transition linewidth.

Our ability to produce an atomic beam with ever increasing PSD impacts fields from the production of ion beam sources for focussed ion beam milling or microscopy to sympathetic cooling and cold chemistry to more fundamental challenges, such as efforts aimed at producing the first steady-state matter-wave source, a continuous atom laser, and a steady-state superradiant laser.

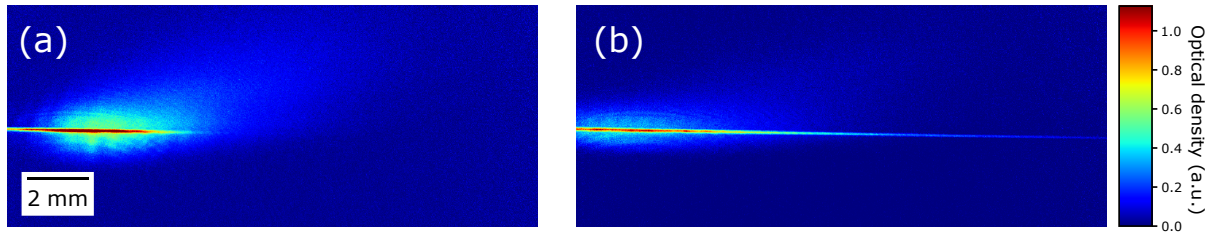FIGURE 4.2: **Comparison between different z-axis red MOT beam intensities.** (a) With higher intensity, the red MOT cloud shape is compressed along the z-axis. There is also a clear indication that the atoms get pushed towards the quadruple field center within the transport guide, see main text. (b) Red MOT with reduced z-axis MOT beam intensity.

4.2 Steady-state ultracold atomic beam

4.2.1 Setup

We have constructed an apparatus capable of producing an ultracold Sr beam with unprecedented performance. We benchmark the apparatus by characterizing a steady-state ^{88}Sr atomic beam with a high PSD of $\sim 1 \times 10^{-5}$, and demonstrate continuous loading of ^{84}Sr atoms into a reservoir trap from an ultracold atomic beam, realizing a steady-state trapped atomic sample near quantum degeneracy. Our steady-state beam source is prepared by flowing a stream of atoms sequentially through multiple cooling stages, separated in space, before reaching the region where the characterization of the high PSD sample is carried out, see Fig. 4.1. All cooling steps before the red magneto-optical trap (MOT) are presented both in our published work [68] and also in Chapter 3. We limit our discussion here on the new method we have developed to generate an ultracold atomic beam and ultracold atomic samples near quantum degeneracy.

Our method consists of several steps, a loading step where a red MOT accumulates atoms, and a transfer step that out-couples the atoms from the MOT into the guide and transports them to the dark region where near-resonant red MOT light is kept at an intensity level of ~ 1 saturation parameter. In the dark region we produce ultracold atomic beam propagating within the transport guide, and we also implement a deceleration scheme to slow down the atoms and demonstrate the continuous loading of a reservoir dipole trap, realizing a steady-state sample near quantum degeneracy. In the following we explain each step in detail.

Loading —   We produce a steady-state red MOT at a temperature of $\sim 6\,\mu\text{K}$ operating on the 7.4-kHz linewidth $^1\text{S}_0$ - $^3\text{P}_1$ intercombination line. We optimize the laser intensities and detunings in order to maximize the transport guide loading efficiency, not in order to obtain the lowest temperature. The red MOT trap geometry uses only five beams in an orthogonal configuration. In the vertical direction, we have only one beam from below and rely on the action of gravity to provide the trapping force from above.   The MOT magnetic quadruple field has gradients of $(0.55, 0.35, 0.23)\,\text{G/cm}$ in the (x, y, z) directions. A schematic representation of the MOT beams can be found in Fig. 3.1, labelled as "Red MOT I", and the beam powers are listed in Tab. 4.1.

The power of the MOT beams along the z-axis is adjusted such that the radiation pressure restoring force along this axis is reduced compared to the other two axes, see Table. 4.1.   We observe that with reduced MOT beam intensities along the out-coupling direction, we could achieve a better transport guide loading efficiency. We benefit from a reduced restoring force in two aspects. First, the cloud has an elongated atomic cloud shape along the out-coupling axis (the z axis) compared to the other two axes (x,y). We therefore get a better shape matching between the atomic cloud and the transport guide. Second, we implement a "dark cylinder" in the MOT beams propagating along the z axis, as shown in Fig. 4.1(b) and explained in Sec. 2.3.6. The reduced beam intensities along the out-coupling axis lead to less residual radiation force within the dark cylinder region. We therefore reduce the radiation force pushing atoms in the guide back towards the quadrupole field center. Both aspects facilitate the loading process of the atoms into the transport guide. In Fig. 4.2 we show an atomic cloud shape comparison between low and high intensity of the z-axis MOT beam.

Transport guide — We continuously load atoms into the transport guide formed by an optical dipole beam overlapped with the steady-state red MOT. The dipole beam is retro-reflected, with the 1st-pass focus located at the red MOT position and a $37\,\text{mm}$ displaced retro-reflection beam focus, forming a tunable transport guide potential landscape, see Fig. 4.3 (c) and Sec. 2.3.5. By varying the retro-reflection power, we can optimize the axial potential landscape profile for the atomic beam deceleration process. The dark cylinder on the z-axis MOT beams is aligned onto the co-propagating transport guide. A dark region is thus covering the whole transport guide and atoms inside the transport guide are thus protected from resonant light scattering from the z-axis MOT beams. The dark region darkness is ultimately limited

TABLE 4.1: Steady-state red MOT laser parameters used in the apparatus. Under "Detuning", $\Delta_1 : \delta : \Delta_2$ refers to a modulated comb of lines from Δ_1 to Δ_2 with a spacing of δ.

Beam name	Detuning [MHz]	Power [mW]	Comments
Red MOT Y	-0.95: 0.02 : -5.2	10.8	Depending on the quadrupole field center relative to the transport guide, detuning is adjusted for optimized atomic cloud shape and spatial overlapping with the trap.
Red MOT X	-0.66 : 0.015 : -2.2	1.2	2 counter-propagating beams
Red MOT Z Outer	-0.82 : 0.016 : -2.2	1.14	Optional, can improved loading flux, but not substantial.
Red MOT Z Inner	-0.85 : 0.017 : -1.25	$\sim$0.01	With dark spot in the beam center.

by imperfections of the dark cylinder and Poisson's spot due to diffraction. By adding a "launch" beam resonant with the $^1S_0 - {}^3P_1$ π transition and pointing it at the overlap between the red MOT and the transport guide, we can outcouple MOT atoms into the guide with a well-controlled mean velocity ranging from 0.08 to 0.25m/s, see Sec. 4.3.2.

Dark cylinder — We create a thin "line-like" dark cylinder in the MOT beams, see Fig. 4.3 (b) and Sec. 2.3.6, similar to the conventional dark setup for a 3D MOT where the atoms do not interact with the repumping light [99] within a "sphere-like" region inside the MOT.

Decelerating — We use the radiation pressure force from the narrow intercombination line to slow down the atomic beam. As Zeeman slower field we exploit the magnetic field gradient from the MOT quadrupole field (see Fig. 4.3 (c)), which has a gradient of 0.23 G/cm along the atomic beam propagation axis. In our implementation atoms are outcoupled from the quadrupole field center into the transport guide, forming an atomic beam that is slowed and stopped 37 mm away from the field center. In a conventional Zeeman slower, the Zeeman slower beam propagates in the opposite direction of the atomic beam, and the radiation pressure force is a function of both Doppler and Zeeman shift. The slowing process stops in a controlled way when the Zeeman shift from the engineered magnetic field combined with the Doppler shift fails the resonance criterion. Atoms are slowed down to a well-defined finite velocity, then propagate onwards in free flight, until they reach the MOT region and are finally stopped and captured by the MOT light near the MOT quadrupole field center. In our Zeeman slower deceleration scheme, the Zeeman slower beam counter-propagates and crosses the transport guide at a small angle, see Fig. 4.3. We spectrally broaden the 7.4 kHz $^1S_0$ - $^3P_1$ narrow-linewidth transition to
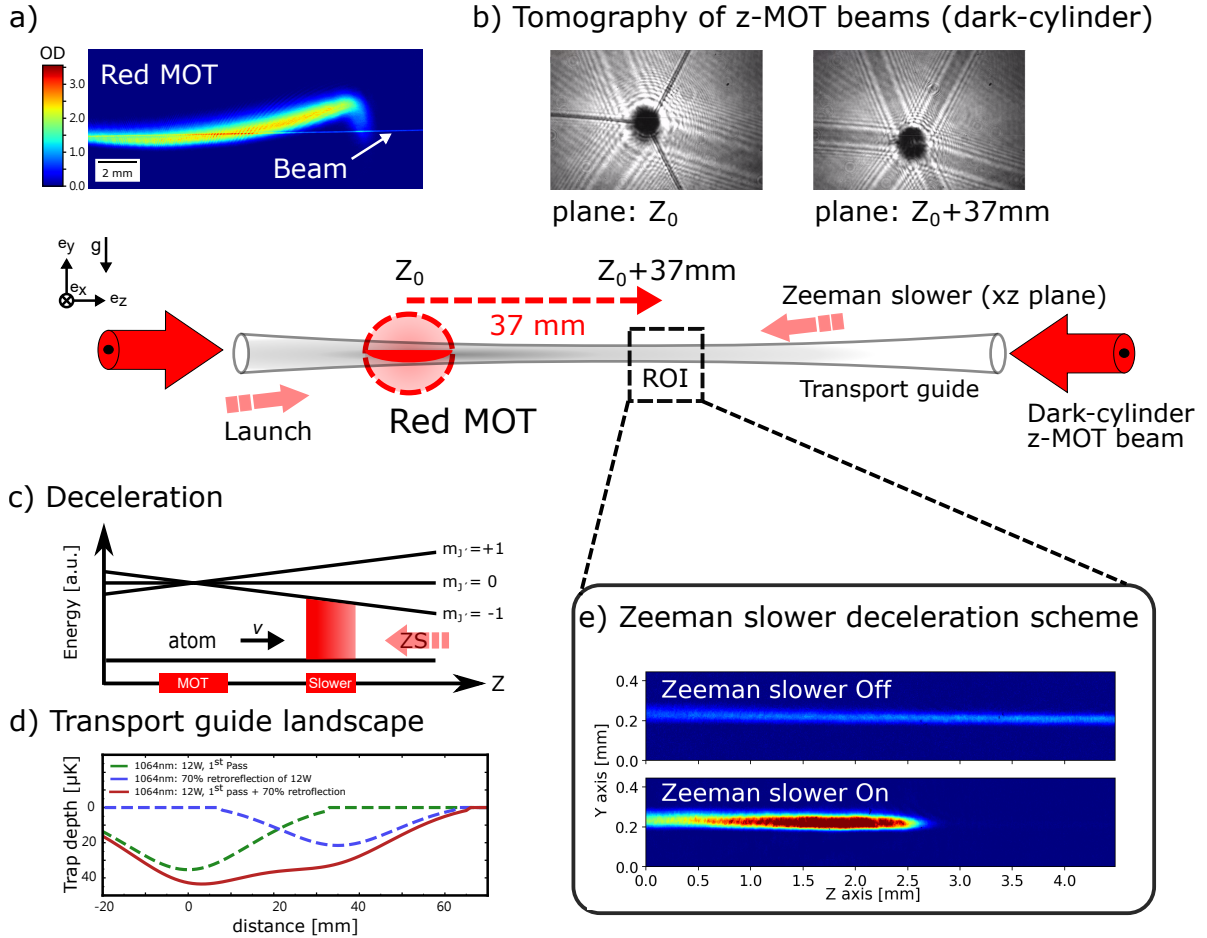
FIGURE 4.3: **Loading, guiding, and decelerating an ultracold Sr beam.** (a) **Scheme of the setup.** A transport guide overlaps with the red MOT. Atoms are continuously loaded into the guide and propagate along the z axis, which is visible in the absorption picture as a faint horizontal line. An elongated dark shadow, a dark cylinder, in the MOT beams eliminates the radiation pressure from the MOT beams on the atoms in the guide. After 37 mm of travel the atoms are slowed by a Zeeman slower operating on the red MOT transition. An overlapping section between the transport guide and the Zeeman slower beam sets the atom-light interaction range and thus the region in which the atoms are decelerated (region of interest (ROI)). (b) **Tomography.** To verify the dark cylinder we image different sections of the MOT beam profile across the transport guide. Two representative figures at the MOT plane (z_0) and the Zeeman slower intersection region ($z_0 + 37$mm) are shown respectively. Three thin wires supporting a dark-cylinder wire on each end are shown in the figure. (c) **MOT quadrupole field.** The diagram shows how the MOT quadrupole field gradient is exploited for a Zeeman slower deceleration scheme. The Zeeman slower beam has a bandwidth of 50 kHz and its detuning is adjusted to be resonant with the atoms in the overlap region. (d) **Transport guide potential landscape.** We calculate the trap potentials formed by the 1st-pass transport guide dipole beam, its retro-reflection and their sum. By varing the retro-beam power we can engineer the transport guide potential landscape. (e) **Zeeman slower.** The upper absorption image shows the atomic beam in absence of the Zeeman slower beam. The lower image shows how atoms accumulate in the ROI when the Zeeman slower beam is present.

50 kHz, and we use it as our Zeeman slower beam exploiting the MOT quadrupole field gradient as Zeeman slower field. Via adapting the frequency detuning depending on the MOT field gradient, we can obtain good spatial selectivity of the region in which the radiation pressure force exists. This way, the slower working distance is preselected by the slower beam alignment and fine adjusted by the frequency detuning. Because the MOT coils are large (several 10 cm) we cannot engineer the Zeeman slower field on a length scale that is smaller than the slowing region, which is only a few mm long. Therefore it is the light intensity within the extent of the Zeeman slower beam and transport guide crossing region determines the atomic beam end velocity.

4.2.2 Figures of merit - an overview

We characterize the flux, velocity, and temperature of the ultracold atomic beam within the transport guide. We quantify the performance of the atomic beam and put it into the context relevant for applications such as superradiant lasers.

In steady-state, atoms propagate along the transport guide with an axial velocity distribution of

$$p(v_z) = \sqrt{\frac{m}{2\pi k_B T_\parallel}} \exp\left(\frac{-m(v_z - \bar{v}_z)^2}{2k_B T_\parallel}\right), \tag{4.1}$$

where m is the mass of the atom, $\bar{v}_z$ is the mean velocity of the atoms, and $T_\parallel$ is the temperature corresponding to the momentum distribution along the transport guide in the moving frame with velocity $\bar{v}_z$. The potential along the radial direction of the transport guide can be approximated by a harmonic potential. Assuming that atoms inside the guide follow a Maxwell-Boltzmann distribution with radial temperature T_r, the density distribution along the radial direction is $n(r) = n_0 \exp\left(-\frac{U(r)}{k_B T_r}\right)$, where r is the radial coordinate, n_0 the peak spatial density, k_B Boltzmann's constant, and $U(r)$ the potential energy at location r. The beam flux Φ thus is represented by

$$\begin{aligned}
\Phi &= \int_0^\infty n_0 \exp\left(-\frac{U(r)}{k_B T_r}\right) \bar{v}_z \, 2\pi r dr \\
&= \int_0^\infty n_0 \exp\left(-\frac{r^2}{2\sigma_r^2}\right) \bar{v}_z \, 2\pi r dr = 2\pi \sigma_r^2 \, n_0 \, \bar{v}_z.
\end{aligned} \tag{4.2}$$

Here $\bar{v}_z$ is the mean longitudinal velocity. The radial atomic density profile is therefore a Gaussian distribution, where σ_r is the $1/e^2$-radius of the atomic beam. By measuring the flux, beam waist and the mean velocity, we then obtain the peak density n_0.

For a gas of bosonic atoms with number density n and temperature T in a three dimensional trap, the phase transition to quantum degeneracy occurs if its phase-space density $\rho = n\lambda_{dB}^3$ exceeds a value of 2.612. Here $\lambda_{dB} = h/(2\pi m k_B T)^{1/2}$ is the thermal de Broglie wavelength, where h is the Planck's constant. The total atom number, N, and the peak density of the cloud are related as $N = n_0(2\pi k_B T/m\bar{\omega}^2)^{3/2}$, where $\bar{\omega} = (\omega_x \omega_y \omega_z)^{1/3}$ is the mean trap frequency. Here we approximate the optical trap potential by a harmonic potential and assume that atoms follow a Boltzmann distribution. Using this relation we can approximate the phase-space density to be $\rho = N \times (\hbar\bar{\omega}/k_B T)^3$.

We can also derive an expression for the phase-space density ρ of the atomic beam at the center of the transport guide and in the frame moving with the beam. For an atomic beam inside a dipole trap guide

$$\lambda_{dB} = \sqrt{\frac{2\pi\hbar^2}{mk_B(T_r^2 T_\parallel)^{1/3}}}.$$
(4.3)

Accordingly the phase-space density is

$$\rho = n_0 \lambda_{dB}^3 = n_0 \left(\frac{2\pi\hbar^2}{mk_B T_\parallel}\right)^{1/2} \left(\frac{2\pi\hbar^2}{mk_B T_r}\right).$$
(4.4)

With knowledge of the radial density distribution n(r) and the axial and radial temperature we can determine the peak phase-space density of our atomic beam.

4.2.3 Results

Atomic beam velocities and axial temperature — Conventionally Doppler sensitive laser-induced fluorescence (LIF) [120, 121] is used for characterizing an atomic beam velocity. However, this method has a limited resolution in our application. We estimate the atomic beam velocity in our setup to be lower than 30 cm/s. The Doppler shift has to be at least comparable to the fluorescence light transition linewidth in order to have a LIF signal with enough velocity resolution. For a 1 cm/s atomic beam the Doppler shift is 14.5 kHz for the 7.4 kHz $^1S_0$ - $^3P_1$ transition, whereas it is 21.7 kHz on the 30 MHz $^1S_0$ - $^1P_1$ transition. So a LIF velocity spectroscopy cannot be based on the 30 MHz broad transition. The 7.4 kHz transition on the other hand is difficult to use since it has a low scattering rate. Furthermore it is difficult to install the required photon collection optics in our experiment because of spatial restrictions.
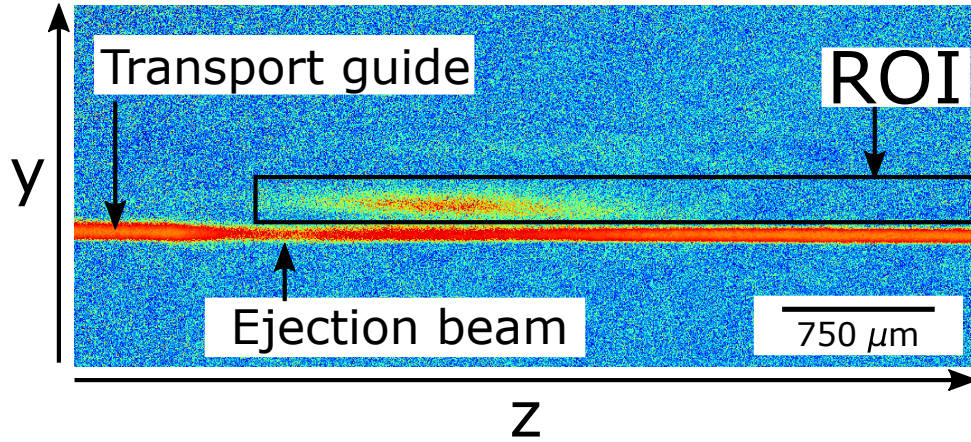
FIGURE 4.4: Atomic beam centre-of-mass velocity and temperature determination. A bunch of atoms is ejected from the transport guide by a resonant pulse of light from an orthogonal "ejection" beam. After 8 ms of free flight the bunch reaches the region of interest (ROI), which we use as fit region to determine velocity and temperature.

Instead, to measure the atoms centre-of-mass velocity and axial temperature of the beam, we briefly pulse on a strongly focused beam align in the transverse direction to the transport guide and resonant with the $^1S_0$ - $^1P_1$ transition. This pulse ejects a burst of atoms out of the transport guide, see Fig. 4.4. The pulse only lasts $1\,\mathrm{ms}$, and we assume that spontaneously emitted photons are equally distributed in all directions during the ejection process, so that the on-axis mean velocity is not affected by the light absorption. By examining the propagation of the packet of ejected atoms almost copropagating near the transport guide, we can infer the mean axial velocity within the $4\,\mathrm{mm}$ long region of interest (ROI) at a distance of $37\,\mathrm{mm}$ away from the capture MOT. Since the Rayleigh range of our transport guide is much longer than the ROI, the axial potential landscape is essentially flat in the ROI region, varying at most by 3%. We thus assume the mean velocity to be constant throughout the ROI. By varying the launch beam intensity, we can regulate the atomic beam velocity from 0.08 to $0.25\,\mathrm{m/s}$. Two representative velocity conditions are shown in Fig. 4.5(b). We observe that in both launching beam intensity conditions the ejected beams have the same temperature $T_\parallel$, see Fig. 4.5(c).

Atomic beam radial temperature — To be able to quantify the phase-space density of the ultracold beam, we also measure the atomic beam temperature in the radial direction. After the atomic beam has reached steady state, we switch off the transport guide and let the atomic beam experience a ballistic expansion. Because the trap depth is estimated to only vary by $\sim 3\%$ across the ROI, we assume that there is only a small

a)
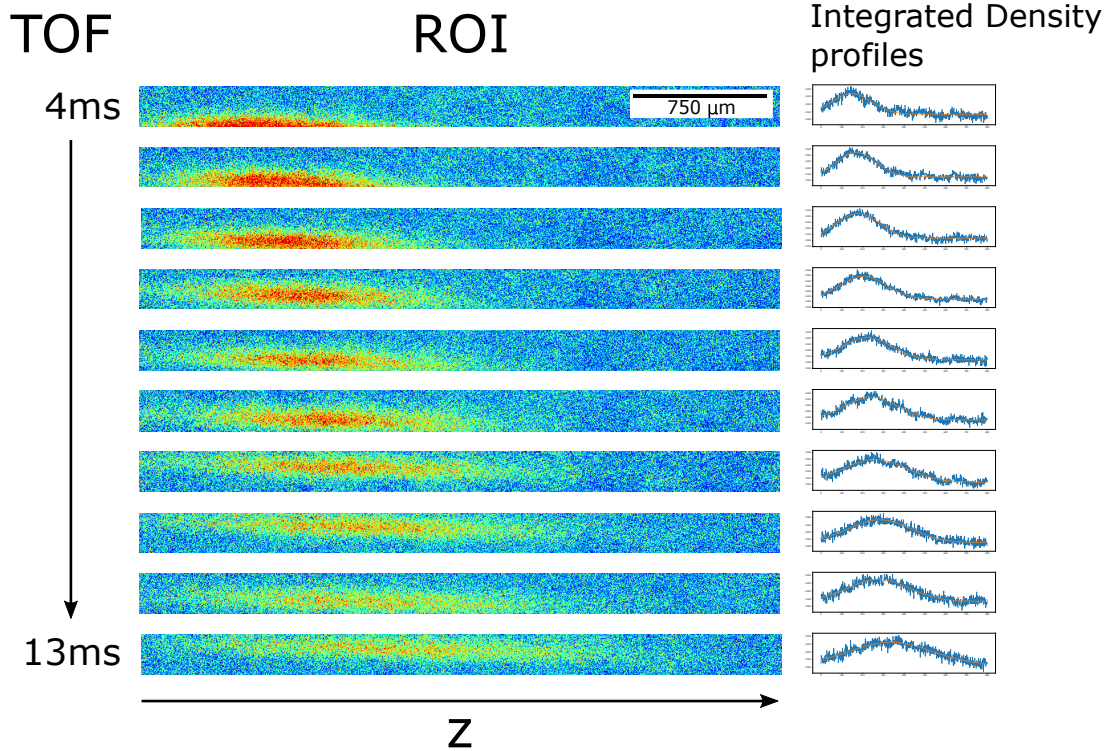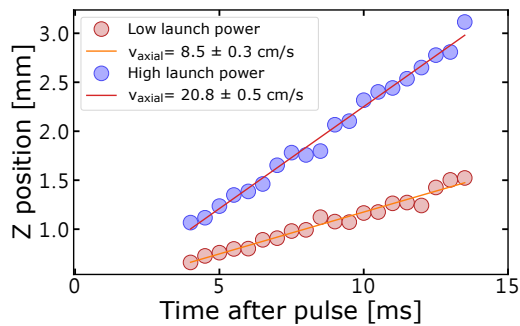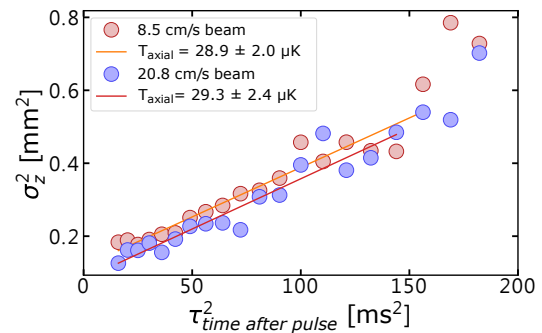
FIGURE 4.5:   **Atomic beam characterization.** (a) Absorption images and respective density profiles of clouds of atoms ejected from the transport guide, taken 4 to 13 ms after the ejection pulse. (b) Evolution of the position along the z axis of two ejected clouds with different mean velocities. The lines are fits from which we extract the velocities. (c) Evolution of the cloud width of two ejected clouds with different mean velocities. By fitting the width, we extract the axial temperature.
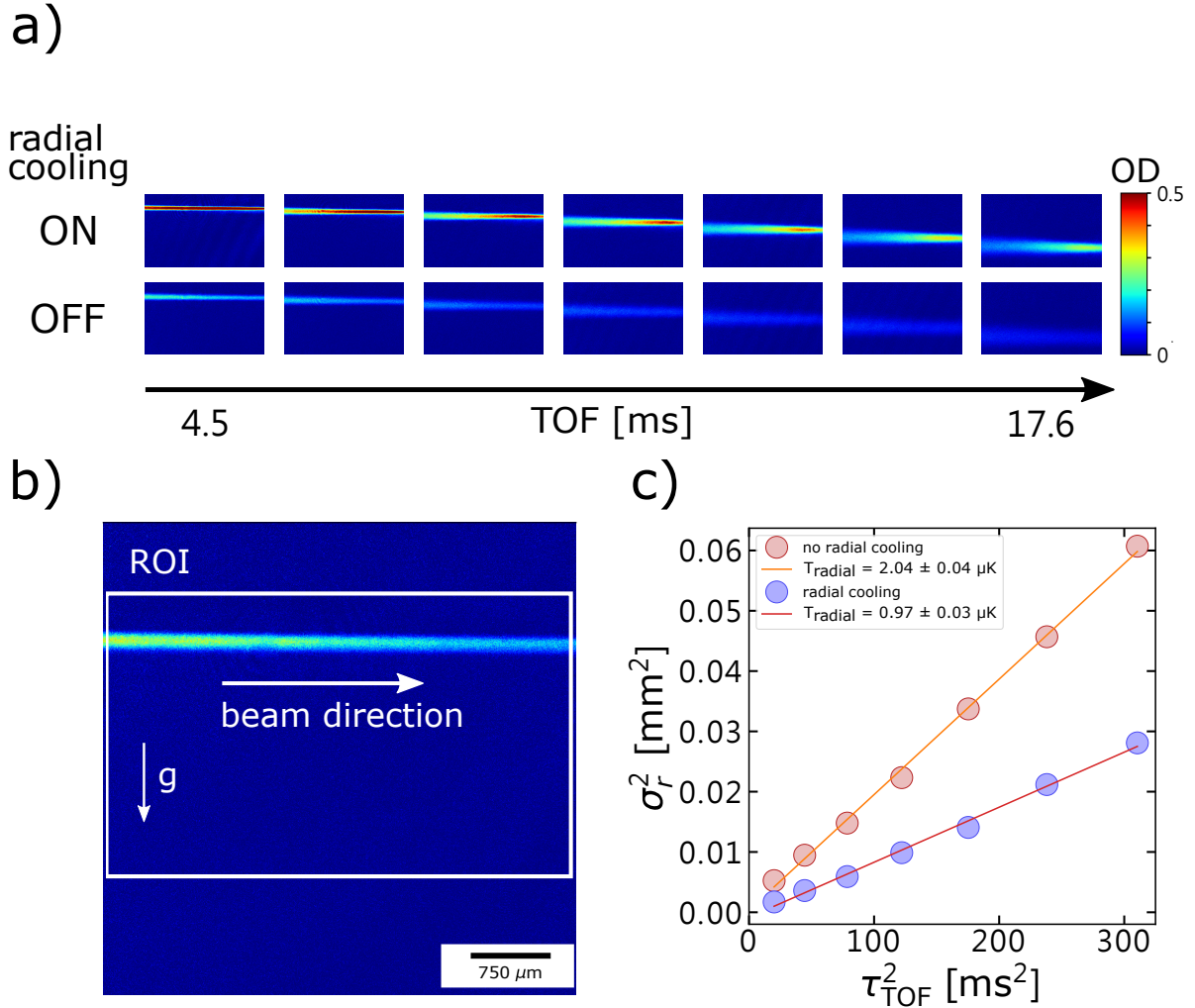
FIGURE 4.6: **Measure of the ^{88}Sr atomic beam radial temperature.** (a) Absorption images of the steady-state atom beam, taken after suddenly switching the transport guide and laser cooling beams off and letting the cloud expand for a certain time of flight (TOF). We compare the behavior of steady-state beams with or without transverse cooling light. (b) Full image has field of view of 4.5×4.5 mm. The white box highlights the region of interest (ROI) shown in (a). We integrate the horizontal axis of the ROI to derive the averaged radial temperature. (c) Atomic beam temperature along the radial direction is measured by integrating the ROI along the horizontal axis, fitting Gaussians to the profile and analyzing the expansion.

radial trapping frequency variation across the ROI. By fitting the TOF images we can get the average atomic beam temperature in the radial direction within the ROI, see Fig. 4.6.

Within the ROI, we observe a mild density distribution gradient along the longitudinal direction of the transport guide. One hypotheses to explain this fact is that there is a small amount of heating because of the residual light from the counter-propagating MOT beam due to imperfections of the dark cylinder. The effect gradually decreases across the ROI because downstream atoms of the atomic beam encounter photons from the counter-propagating laser beam before upstream atoms. The downstream atoms thus get heated but also attenuate the residual light. Another hypothesis could be that they are heated out because corrugations in the guide potential transfer momentum from the axial to the radial direction, leading atoms to escape the guide. By adding the transverse cooling light, we notice that it mitigates the heating effect and improves the atomic beam flux. The transverse cooling light is illuminating the guided atomic beam from the radial direction using $28.8\,\mathrm{mm}$ $1/e^2$ diameter Gaussian laser beams with a combined intensity corresponding to a saturation parameter of ~ 1. This dramatically increases the atomic beam flux, see Fig. 4.6 (a). Transverse cooling also reduces the radial temperature of the atomic beam, and we can achieve sub-μK radial temperature, see Fig. 4.6 (c).

We have presented a steady-state ultracold ^{88}Sr atomic beam horizontally guided by a transport dipole trap. We achieve sub-μK temperature in the radial direction and an atomic beam flux $> 1.1 \times 10^5$ ^{84}Sr/s ($> 6 \times 10^6$ ^{88}Sr/s). The atomic beam in the guide has a waist of $23.3 \pm 0.8\,\mu$m across the full ROI, as measured with in-situ absorption imaging, see Fig. 4.6 (b). The ^{88}Sr atomic beam central density $n_0 \sim 1.2(6) \times 10^{10}$ $1/\mathrm{cm}^3$, calculated using Eq. 4.2 and the knowledge of atomic beam waist and velocity. Combined with the knowledge of $\mathrm{T_{radial}} \sim 1\ \mu$K and $\mathrm{T_{\parallel}} \sim 30\ \mu$K, we demonstrate an ultracold ^{88}Sr beam with a phase-space density $\sim 1.4(6) \times 10^{-5}$. To our knowledge, this is the highest phase-space density ever achieved in a continuous ultracold beam experiment [122].

4.3   Steady-state ^{84}Sr cloud near quantum degeneracy

Compared to the abundant ^{88}Sr isotope of which the scattering length is almost zero, ^{84}Sr has a scattering length of about $+124\,a_0$, which is suitable for atoms to efficiently reach thermal equilibrium. To attain even higher phase-space densities and
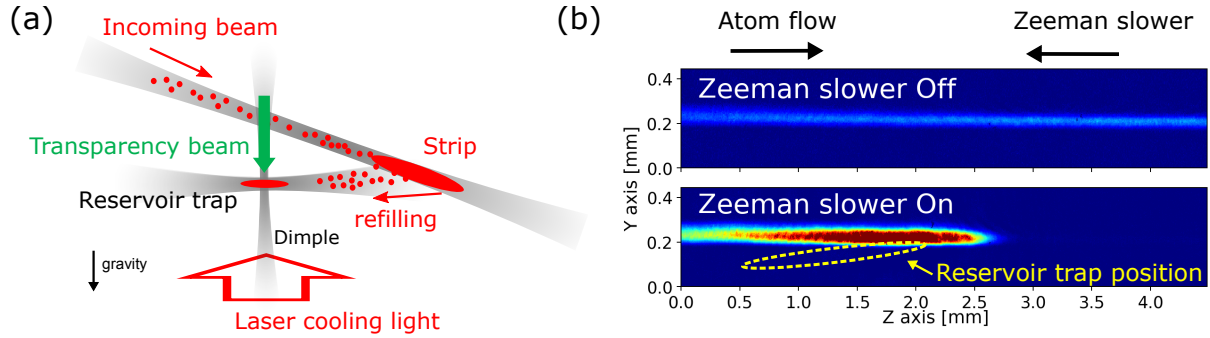
FIGURE 4.7: **Adding a refilling mechanism to the laser cooling to BEC scheme.** (a) **Reservoir filling scheme.** The trapped ^{84}Sr atoms in the reservoir dipole trap are continuously exposed to the laser cooling light (red arrow). Within the crossing region of the reservoir trap and the dimple trap, atoms are exposed to a "transparency" laser (green arrow) , which induces a light shift on the $^3P_1$ state, protecting the atoms from laser cooling light. The atoms accumulate in a dimple trap and thermalize with the laser cooled cloud via elastic collisions. By replenishing the reservoir trap with newly-decelerated ultracold atoms, we intend to create a steady-state BEC. (b) **Reservoir trap position.** The figure shows an ultracold atomic beam in the transport guide with and without applying a Zeeman slower beam. By using a Zeeman slower, we decelerate the atoms next to the location of the reservoir. The reservoir location is marked in the figure, and its position is adjacent to the strip of decelerated atoms.

ultimately realize a steady-state BEC, we switch to the ^{84}Sr isotope and continuously load the atoms into the reservoir trap. We show the unprecedented performance of the atomic beam by demonstrating its instrumental role as a reservoir refilling beam source for realizing an ultracold cloud of ^{84}Sr near quantum degeneracy.

4.3.1 Setup

The atoms are transferred through the guide into the dark region, Zeeman slowed there, and transferred into the laser cooling to BEC platform. This platform consists of three elements. A large reservoir dipole trap, a vertical dimple dipole beam crossing the reservoir and two transparency beams.

Reservoir— Before the atoms are loaded into the reservoir trap, atoms within the transport guide are slowed down by the Zeeman slower beam. The atoms now have a velocity distribution corresponding to a few photon recoils. We plan to use the continuous atomic beam we have made for reloading the reservoir of our "laser cooling to BEC" platform, see Fig. 4.7. In the architecture as shown in Fig. 4.7 (a), atoms within the reservoir are continuously laser cooled by the cooling light working as optical molasses. The cooling power (entropy dissipation power) is determined by

the local atomic density within the laser-cooled reservoir, which sets the elastic collision rate. Therefore the achieved steady-state temperature of the reservoir is a dynamic balance established between the cooling power and new energetic refilled atoms, whereas cooling atoms within the transparency protected region relies on elastic collisions with atoms in the reservoir.

One might ask if it would be possible to exploit the atomic beam strip in the transfer beam as reservoir and create a steady-state BEC in the middle of the atomic beam strip by crossing the transfer beam with a dimple and transparency beam. We tried this approach and did not reach low temperatures in the reservoir. The reason for this outcome is that in our Zeeman slower implementation, see Fig. 4.3 (d), a near-detuned counter-propagating laser beam crosses the incoming atomic beam at a small angle, creating a strip of decelerated atomic cloud. On the input side of the decelerated atomic beam strip, atoms experience head-on collisions from the incoming flow of atoms. Atoms on the other side (right in Fig. 4.7 (b)) experience a radiation pressure force from the Zeeman slower beam. We measure the temperature of the atomic beam strip and show that the temperature along the deceleration axis is a factor of six higher than the reservoir temperature demonstrated in the "laser cooling to BEC" experiment. We therefore conclude that it is not ideal to position our reservoir trap at the same location as the ZS, which will very likely complicate the deceleration and reservoir laser cooling process.

We decide to implement the reservoir at the position that connects with the decelerated atomic beam strip only on one end instead of right on top, overlapping with the deceleration region, see Fig. 4.7 (b). By configuring the architecture in this way, we can de-couple the deceleration mechanism from atoms within the laser-cooled reservoir. The reservoir beam has an elliptical beam geometry with a beam waist of 14.8 μm (119 μm) in the vertical (horizontal) direction, reaching an aspect ratio of 1 : 8. The elliptical beam creates a trapping potential with a high trapping frequency in the vertical direction, while keeping the mean trapping frequency low. The horizontal trapping frequency is mainly provided by a vertical dimple beam, which crosses the horizontal elliptical beam, see Fig. 4.7. The implementation of the reservoir trap starts with a fiber coupler with a focal length of 40 mm[1]. The beam size is then expanded by the 1$^{\text{st}}$ stage telescope with a (-50, 75) mm lens combination. After the beam expansion stage, we insert a cylindrical lens telescope (100, 30) mm to convert the beam into an elliptical beam with the long axis

---

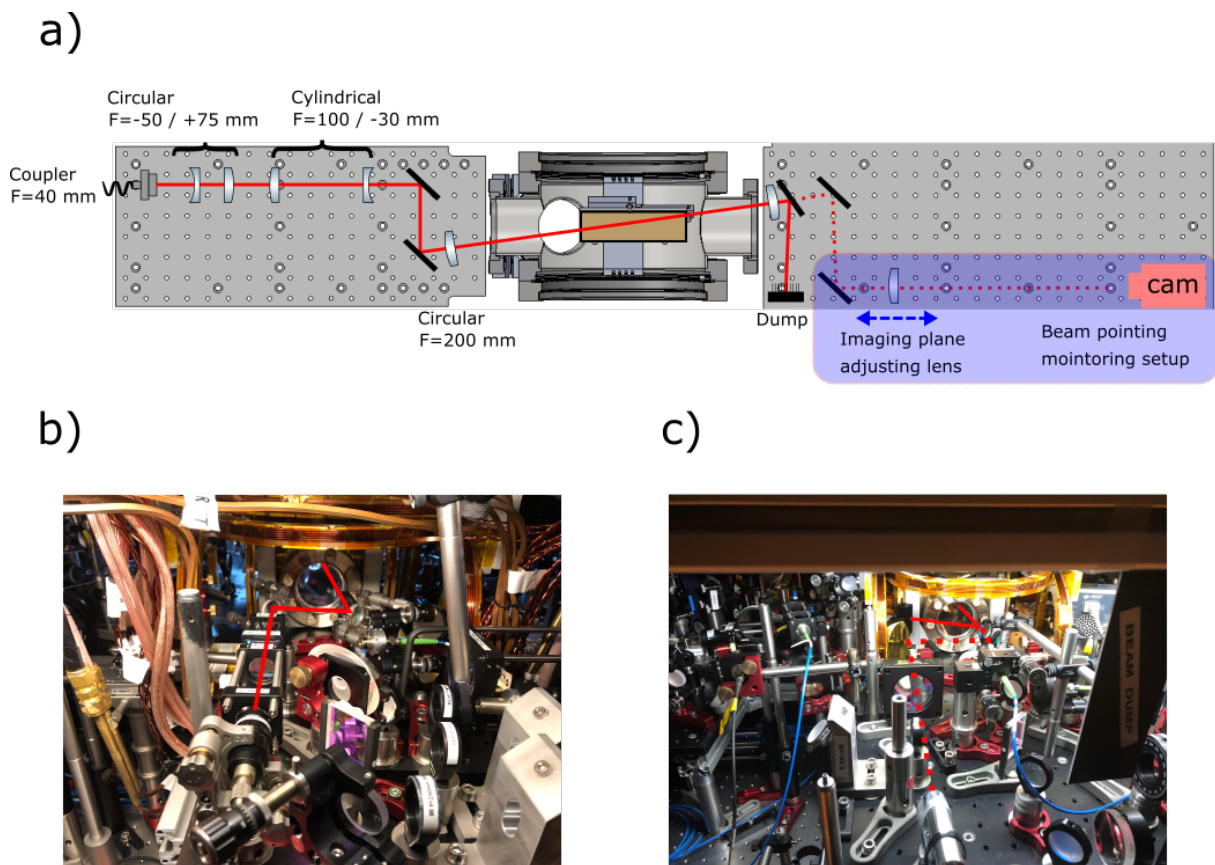[1]Schäfter + Kirchhoff GmbH, M40-37

FIGURE 4.8: **Reservoir dipole trap setup.** (a) Optics layout for the reservoir beam implementation. The light purple area highlights the beam pointing monitoring setup. We use it for daily alignment checks. It is also useful to determine the reservoir beam focal plane. (b) Optics on the wall side. (c) Optics on the aisle side.

in the vertical direction. After shaping the beam, we focus it with a 200 mm lens and send the light into the chamber, see Fig. 4.8.

Dimple — We employ a crossed-beam geometry for the final region of our experiment, similar to the potential landscape used in our laser cooling to BEC work [11].

Transparency beam — The transparency laser frequency is $\sim$ 30 GHz blue-detuned with respect to the $^3P_1$ to $^3S_1$ transition. Two transparency beams, one vertical and one under a $\sim 45°$ angle relative to the z axis, overlap at the location where the reservoir trap is crossed by the vertically oriented dimple beam. The non-vertical transparency beam contains a σ^+ component, which shifts the $^3P_1$, $m_J = -1, 0$ sublevels. It complements the vertical transparency beam, which has π polarization and shifts only the $m_J = -1, +1$ sublevels. Together both transparency beams shift all three sublevels of the $^3P_1$ state. In order for the two light shifts to add without interference we use a frequency difference of 700 MHz between the two transparency beams.

4.3.2   Results

Quantities characterizing crucial steps in our scheme are shown in Fig. 4.9 (a) for an oven temperature of $510\,°C$. We show absorption images of the reservoir region from horizontal and vertical directions in Fig. 4.9 (b,c). The transport guide and the reservoir dipole trap potential landscape are revealed by the in-situ image of the steady-state atomic density distribution. As has been noted above, the reservoir trap is displaced from the transport guide in the vertical direction to avoid the incoming stream of atoms, which would lead to undesirable collisions, see Fig. 4.9 (c). By a judicious choice of the position of the reservoir trap, we realize a suitable potential landscape for reservoir refilling at the crossing section of reservoir trap and transport guide. We also have the same dipole trap induced light shift on the red MOT transition in both, the reservoir trap and the transport guide. We can thus reach optimum molasses cooling in both regions using one set of laser beams applied along the radial direction.

Estimation of phase-space density (PSD) — To determine how close our experimental conditions are from the critical value for the phase transition to steady-state quantum degeneracy, we characterize the PSD of our steady-state atomic cloud. In Fig. 4.10, we show images taken from both the horizontal and vertical axes

a)

Guided atomic beam:
Flux: >1.1 X 10^5 ^{84}Sr/s (>5 X 10^6 ^{88}Sr/s)
Beam $1/e^2$ radius: 0.023µm
T_{radial}: 1.35 µK
Velocity~ 0.1 m/s

Slower (without reservoir and dimple):
Flux: 1.1 X 10^5 ^{84}Sr/s
Number: 3.7 X 10^5 ^{84}Sr
T_{radial}: 0.95 ± 0.05 µK
T_{axial} : 6 ± 2 µK

Transparency beam

e_y g
e_x
e_z

Red MOT
3.7 cm
Zeeman slower

Transport guide
Reservoir trap
Dimple

Laser cooling light

Reservoir:
T_y: 0.61 ± 0.02 µK
T_x: 0.85 ± 0.05 µK

Red MOT:
Flux: 2 X 10^6 ^{84}Sr/s
Number: 6 X 10^6 ^{84}Sr
T_y: 6.8 µK
Transport trap depth: ~30 µK

b) Theoretical potential landscape

c) Experimental density distribution

FIGURE 4.9: **Performance of a steady-state ultracold Sr beam continuously loading into the dipole trap reservoir.** (a) Beginning with a steady-state MOT operating on the $^1S_0 - {}^3P_1$ transition, atoms are continuously out-coupled and transferred into a reservoir trap through a transport guide, which is dark-cylinder protected from residual near-resonant MOT light. A dimple trap is overlapped with a transparency beam, making atoms within this dimple trap off-resonant to laser cooling light, thus suitable for condensation. The atomic beam performance is characterized at each stage of the SrPAL beam machine running in a steady-state regime. We choose ^{84}Sr as our characterization isotope (see main text). (b) Top and side view of calculated potential landscape for $^1S_0$ state. (c) Top and side view of ^{84}Sr atoms, continuously loaded into a reservoir trap.

a)

b)

c)

FIGURE 4.10: **Production of steady-state ultracold ^{84}Sr near quantum degeneracy.** (a,b) In-situ absorption images of density profiles of the atoms in the reservoir region taken from the side and from the top, respectively. (c) Time of flight of an ultracold ^{84}Sr sample. From the cloud expansion along the vertical direction we can derive the temperature by fitting the spatial profile of the atomic cloud. We also try to look for signs of a bimodal distribution in the cloud expansion images, a typical signature for a BEC.

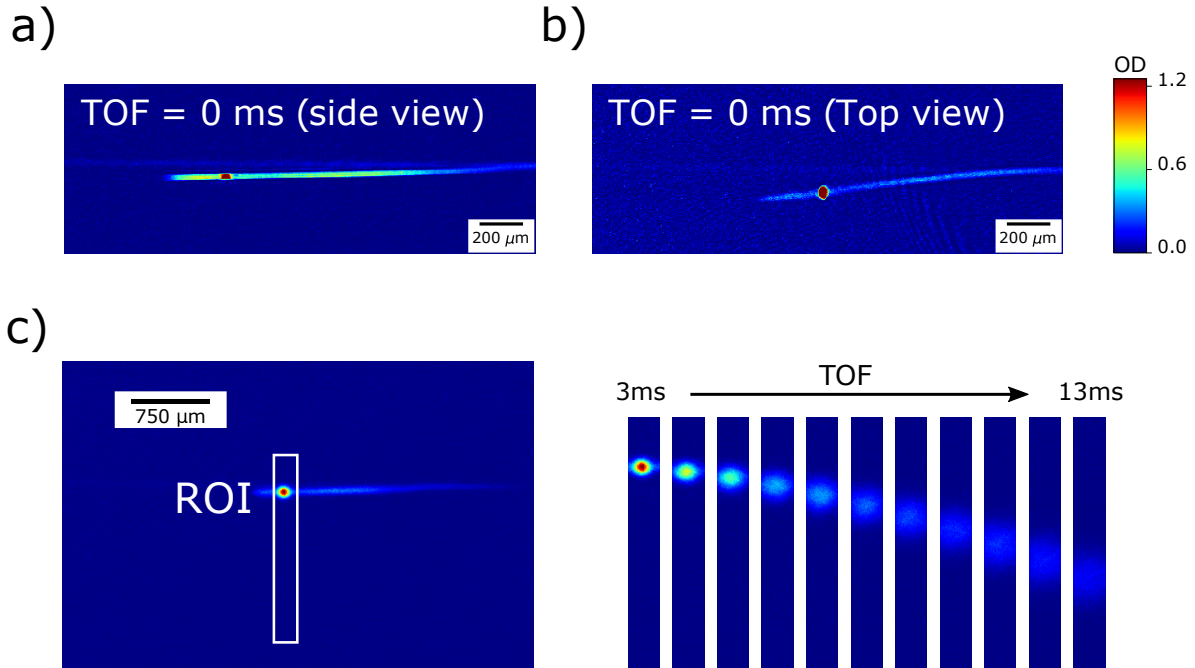of a steady-state ultracold ^{84}Sr atomic cloud. We have $N = 2.5(2) \times 10^5$ atoms in a trap with frequencies of $(\omega_x, \omega_y, \omega_z) = 2\pi \times (290 \pm 5, 980 \pm 3, 290 \pm 5)$Hz. The measured temperatures along each axis are $(T_x, T_y, T_z) = (1.07(4), 0.98(3), 1.80(20))$ μK. A conservative estimation of PSD is given for our steady-state ultracold cloud, and we show that we have achieved a PSD of 1.21 ± 0.13. So far we have not observed any steady-state BEC signatures in time-of-flight images of the ultracold cloud from our steady-state experiment, such as a bimodal distribution or the inversion of aspect ratio of an elliptical cloud. This is by far the best steady-state PSD ever achieved, exceeding previous experiments by four orders of magnitude, see Fig. 4.12.

We have verified the effectiveness of the transparency beam protection by comparing the lifetime of a time-sequentially produced BEC within the transparency beam protected trap. We measured the lifetime in presence or absence of the near-resonant 689-nm light as used in steady-state operation. In both cases we measured the same BEC lifetime, $\tau_{\text{BEC}} = 1.27 \pm 0.05$ s (1.30 ± 0.06 s), in presence (absence) of 689-nm light as used in steady state. We therefore conclude that the

transparency beam provides enough light shift for atoms within the protection region and our PSD is not limited by "atom-photon scattering".

We notice that the phase transition occurs if we first reach steady-state and then only switch off the beam of the red Zeeman slower at the end of the transfer guide. This effectively nullifies the reservoir trap loading rate and reduces any effect of the Zeeman slower beam on the reservoir region not protected by the transparency beams. In Fig. 4.11, we show an absorption image of a condensate that forms 200 ms after the red Zeeman slower is switched off.

The ease of obtaining a BEC demonstrates that we have nearly reached degeneracy in steady-state. Furthermore it suggests that our reservoir atoms are still disturbed by the red Zeeman slower, be it from its light or from the atoms that it continuously loads into the reservoir. To verify the real cause of disturbance, we produce BEC time-sequentially and investigate the BEC behavior in presence of reservoir loading condition as used in steady-state operation, and compared it to the case with reduced reservoir loading rate (40% less red Zeeman slower intensity). We observed the BEC melts under the steady-state experimental operation condition while it maintains condensation in the later case. We conclude that the collisional heating induced by the newly arriving atoms so far exceeds the reservoir cooling power. A more gentle way of loading the reservoir is needed and demonstrated in the next chapter.
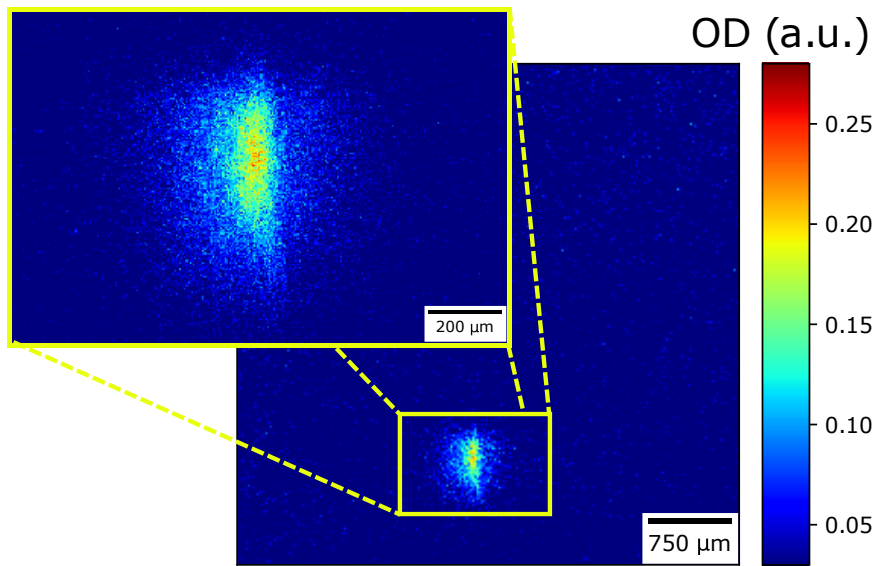
FIGURE 4.11:   **One step from a high phase-space density ^{84}Sr sample to quantum degeneracy.** A BEC achieved after reaching steady-state and then suddenly reducing the Zeeman slower beam power by a factor of two. This lowers the reservoir loading rate and also reduces the Zeeman slower beam intensity on the reservoir. After a wait time of 200 ms, a 22 ms time-of-flight image is taken, showing the characteristic density profile of a BEC.
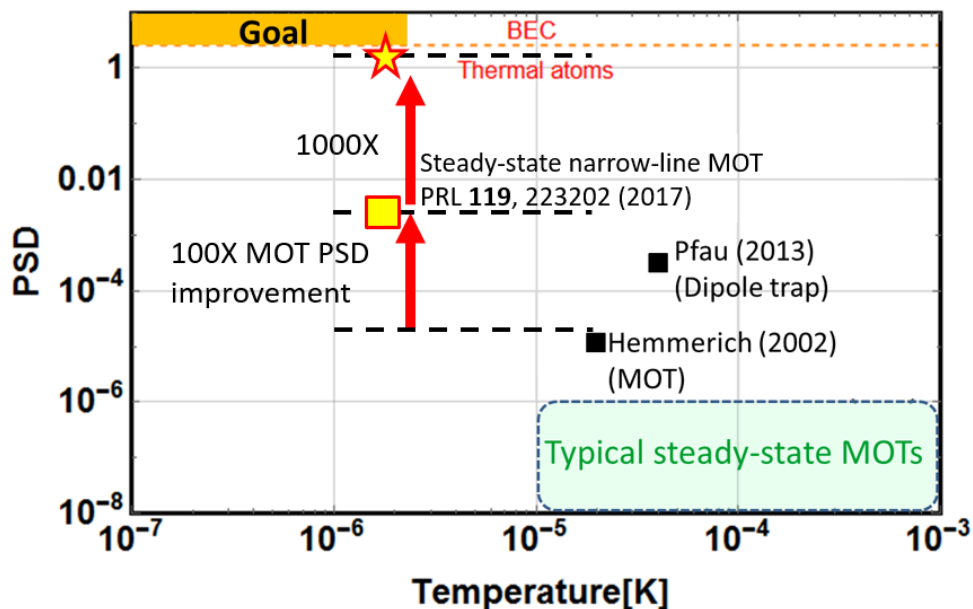
FIGURE 4.12: **History of steady-state ultracold samples.** Previous experiments and ours are marked in this plot of two figures of merit, steady-state PSD and temperature. The yellow square marks our experiment from Chapter 3 and the yellow star indicates the current status of our experiment: a phase-space density of unity at a temperature of $1.23 \pm 0.05 \,\mu$K.

Chapter 5

Pre-print: Sisyphus Optical Lattice Decelerator

Chun-Chia Chen , Shayne Bennetts, Rodrigo González Escudero, Florian Schreck, Benjamin Pasquiou

Van der Waals-Zeeman Institute, Institute of Physics, University of Amsterdam, Science Park 904, 1098XH Amsterdam, The Netherlands

We experimentally demonstrate a variation on a Sisyphus cooling technique that was proposed for cooling antihydrogen. In our implementation, atoms are selectively excited to an electronic state whose energy is spatially modulated by an optical lattice, and the ensuing spontaneous decay completes one Sisyphus cooling cycle. We characterize the cooling efficiency of this technique on a continuous beam of Sr, and compare it with radiation pressure based laser cooling. We demonstrate that this technique provides similar atom number for lower end temperatures, provides additional cooling per scattering event and is compatible with other laser cooling methods. This method can be instrumental in bringing new exotic species and molecules to the ultracold regime.

5.1   Introduction

The asymmetry between matter and antimatter is one of the great mysteries of modern physics. A promising avenue to better understand this asymmetry is to precisely compare spectra of hydrogen with antihydrogen, but this requires the ability to generate robust trapped samples of ultracold antihydrogen [123, 124, 125, 126, 127].

Unlike hydrogen, antihydrogen can not be cooled through evaporation [128]. Indeed, antihydrogen atoms are produced in such small numbers that collisions are rare and thermalization rates are impractical [123, 124]. Instead, laser cooling is needed at 121.6 nm, where performances remain strongly constrained by current laser technology despite heroic efforts [129, 130, 131, 132]. The proposal in [34] overcomes these limitations by allowing the extraction of many photon recoils of momentum per scattering event by the simple addition of an optical lattice.

This method is not limited to cooling antihydrogen [34]. Related proposals have considered a similar working principle to cool and localize atoms [33, 133] as well as to decelerate hot Yb atomic beams [134]. Slowing and cooling ultracold molecules [135, 136, 137] is perhaps the most topical application for this method today. Recent striking successes in molecule cooling have relied chiefly on applying laser cooling to molecules, either by choosing species with close-to-diagonal Franck-Condon factors [138, 139, 140], or by using highly efficient laser cooling techniques [141, 142]. The introduction of the present cooling method can bring better cooling efficiency and a broader class of laser cooled molecules. In turn, progress in molecule cooling is opening a plethora of ways to probe the very foundations of physics [143, 144]. Some of the most prominent include tests for the possible variation of fundamental constants [80] and tests of the validity of fundamental symmetries [145, 146, 147, 148, 149, 150].

A range of approaches have been devised to achieve improved performance while relaxing constraints imposed by traditional Doppler cooling techniques. For example, rapid cycling using stimulated emission can provide stronger momentum transfer without spontaneous heating or loss from non closed cycling transitions. This is demonstrated in bichromatic force cooling [151], adiabatic rapid passage [152] and SWAP cooling [153] but it requires intense resonant light not available at the 121.6 nm transition needed for antihydrogen. Alternatively, Sisyphus-like cooling methods [14], where kinetic energy is converted into potential energy, can function effectively even at very low pumping rates and are routinely applied to beat the Doppler temperature limit [84]. Examples of this approach include Zeeman-Sisyphus decelerators [154] and Rydberg-Stark decelerators [155, 156], where a photon excitation changes the internal state allowing a significant part of the slowing to be done by an externally applied electromagnetic field gradient.

In this letter, we present a proof-of-principle demonstration of a variation on the scheme proposed by Wu et al. [34] to laser cool antihydrogen. Without using
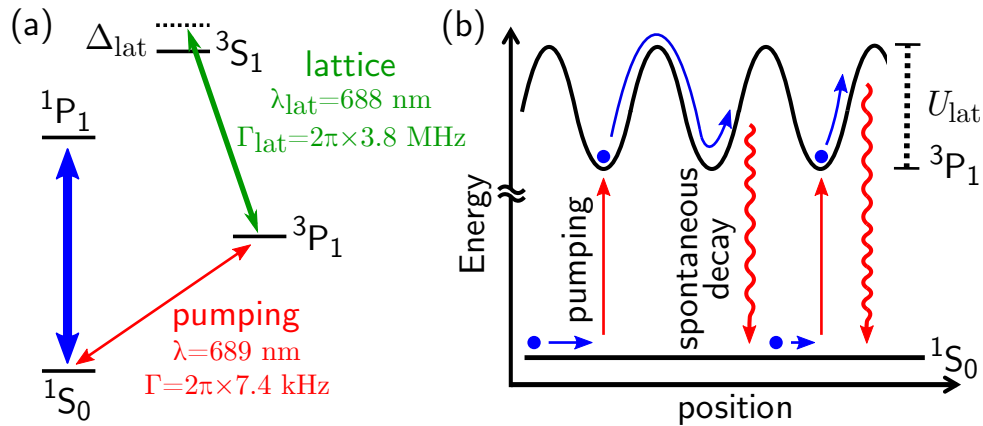
FIGURE 5.1: (a) Relevant electronic levels of strontium and the two transitions used for pumping and optical lattice creation, both necessary for the SOLD. (b) Schematic of two typical cooling cycles, from pumping to spontaneous decay.

radiation pressure, we slow a continuous stream of strontium atoms using a Sisyphus-like deceleration mechanism also described in other proposals [33, 133, 134]. The method uses a 1D optical lattice acting on the excited $^3P_1$ electronic state combined with a selective pumping mechanism that excites atoms to the lattice potential minima. We explore the performance of this technique, which we name a Sisyphus Optical Lattice Decelerator (SOLD), for various atomic beam velocities and lattice heights. Compared with the standard Zeeman slower, we show that the SOLD obtains similar fluxes but with lower temperatures. In principle, by using a deep lattice very few pumping photons can be sufficient to bring fast atoms to rest, making SOLD a good decelerator candidate for exotic species and molecules without a closed cycling transition [136, 138, 139, 142, 140].

5.2 Sisyphus cooling scheme principle

The working principle of the SOLD relies on a 3-level system coupled by two optical transitions, something ubiquitous for both atomic and molecular species. Our implementation using strontium is depicted in Fig. 5.1(a). An optical lattice is formed using a pair of coherent counter-propagating beams with a frequency in the vicinity of the $^3P_1 - ^3S_1$ transition. This produces a spatially modulated coupling between the $^3P_1$ and $^3S_1$ states and thus a spatially modulated light shift on the excited $^3P_1$ state. The ground $^1S_0$ state remains essentially unaffected. By applying a laser resonant with the $^1S_0 - ^3P_1$ transition, atoms can be optically pumped into the $^3P_1$ state where

they experience the force associated with the lattice potential, see Fig. 5.1(b). If the linewidth Γ of the $^1S_0 - {}^3P_1$ intercombination line is much smaller than the lattice height $U_{\text{lat}} \gg \hbar\Gamma$, this "pumping" laser can be tuned to selectively address the bottom of the lattice sites. For high enough velocity $v > \lambda_{\text{lat}}\Gamma$, atoms pumped into $^3P_1$ will then climb a significant fraction of the lattice potential hills and lose kinetic energy before spontaneously decaying back to the ground state as shown in Fig. 5.1(b). As atoms in $^1S_0$ continue to propagate along the lattice axis, this cooling cycle can repeat like a Sisyphus mechanism. By making the lattice very deep it is theoretically possible to remove most of the forward kinetic energy of an atom with a single cycle, as in Rydberg-Stark decelerators [155, 156], and potentially within distances on the order of the lattice period. The theoretical temperature limit for this scheme is the higher of an effective Doppler temperature depending on Γ [133], or the recoil temperature associated with spontaneous emission.

5.3 Experimental realization

To demonstrate experimentally the feasibility of the SOLD, we implement the setup shown in Fig. 5.2(a). We start with a magneto-optical trap (MOT) operating in a steady-state regime on the $7.4\,\text{kHz}$-linewidth $^1S_0 - {}^3P_1$ line, as described in our previous work (configuration "Red MOT I" of [68]). We overlap this MOT with an optical dipole trap acting as a "transport" guide [157]. This 1D guide is $\sim 35\,\mu\text{K}$ deep at the MOT location and propagates horizontally along the z axis. By adding a "launch" beam resonant with the $^1S_0 - {}^3P_1$ π transition and pointed at the overlap between the MOT and transport guide, we outcouple MOT atoms into the guide with a well-controlled mean velocity ranging from 0.08 to $0.25\,\text{m.s}^{-1}$ (see Section 5.6.3). Atoms then propagate along the transport guide for $\sim 3.7\,\text{cm}$ until they reach the decelerator region.

We produce a 1D lattice potential with a pair of counter-propagating laser beams whose frequency is blue-detuned by $\Delta_{\text{lat}} \approx 2\pi \times 30\,\text{GHz}$ from the $^3P_1 - {}^3S_1$ transition. The lattice beams cross the transport guide at a shallow angle of $6°$, overlapping the atomic beam for about $3.4\,\text{mm}$. Optical "pumping" from the $^1S_0$ to $^3P_1$ state is provided by illuminating the atoms from the radial direction. Pumping laser beams are $15\,\text{kHz}$ red detuned from the π transition and their combined intensity corresponds to a saturation parameter of ~ 1. In addition to pumping, these beams provide an optical molasses effect, which brings the atoms' radial temperature to
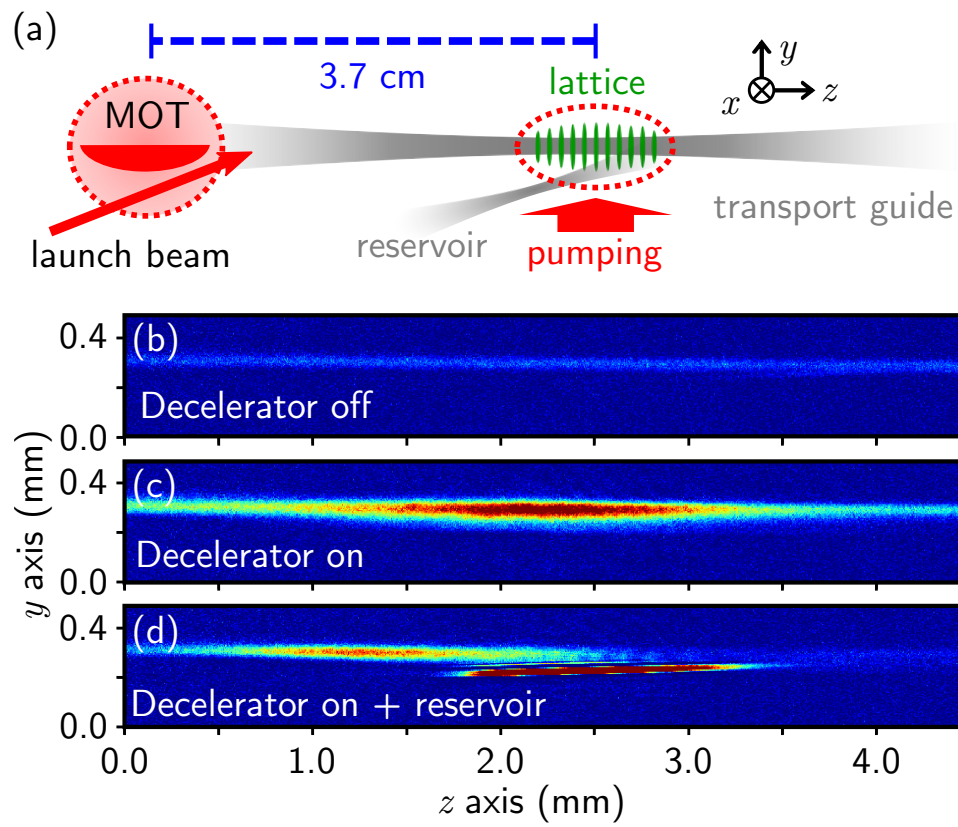
FIGURE 5.2: (a) Side view of the setup. (b,c,d) $^1S_0 - {}^1P_1$ absorption imaging pictures of the atomic beam at the location of the decelerator, (b) without lattice, (c) with lattice, and (d) with both lattice and reservoir trap.

$\sim 2\,\mu$K. Importantly, there is no near-resonant light capable of slowing atoms in the z axis in the absence of the SOLD optical lattice.

We operate the decelerator on a guided atomic beam continuously fed by the MOT, with a homogeneous axial density across the full field of view of our imaging system, see Fig. 5.2(b). When the lattice is switched on, the density in the overlap region between the atomic and lattice beams sharply increases, suggesting an accumulation of slowed atoms, as shown in Fig. 5.2(c). Without either lattice beam or with a large (160 MHz) frequency difference between the two lattice beams, this feature vanishes. Fig. 5.2(c) also shows that some atoms travel completely across the lattice region due to incomplete slowing or by diffusion. Note that our slowing mechanism is fully compatible with a steady-state apparatus, and we perform our measurements after reaching steady state.

For better characterization of the SOLD, and since we are concerned about diffusion of slowed atoms, we add a second "reservoir" dipole trap beam. This beam crosses below the transport guide at the lattice location, with an offset adjusted to allow slow atoms to pass from the guide into the reservoir while not significantly disturbing the potential landscape of the guide. Thus, the reservoir collects slowed atoms $2\,$mm away from the crossing, which are ultimately stored there with the help of optical molasses, see Fig. 5.2(a). We measure the mean velocity selectivity of the loading of this reservoir (see Section 5.6.1), which matches a Gaussian centered around zero velocity with a width $\sigma_v = 0.0084(4)\,$m.s^{-1}. We show one example of loading into this reservoir in Fig. 5.2(d), which also exemplifies a means of atom extraction from our ultracold atom source. We show in Fig. 5.3 the measured atom number loaded into the reservoir by the SOLD. The efficiency is poor for small lattices, as not enough kinetic energy is removed before atoms leave the lattice location. For increasing lattice height, we observe a clear loading optimum, followed by a slow decrease. These two features originate from the behavior of the pumping rate to ^{3}P$_1$.

5.4   Sisyphus cooling scheme: model

We can better understand the observed SOLD slowing efficiency by using a simple semi-classical model describing its various working regimes, which depend on the relative magnitude of the atoms kinetic energy with respect to the lattice height. Consider an atom initially pumped into the ^{3}P$_1$ state at the bottom of the lattice
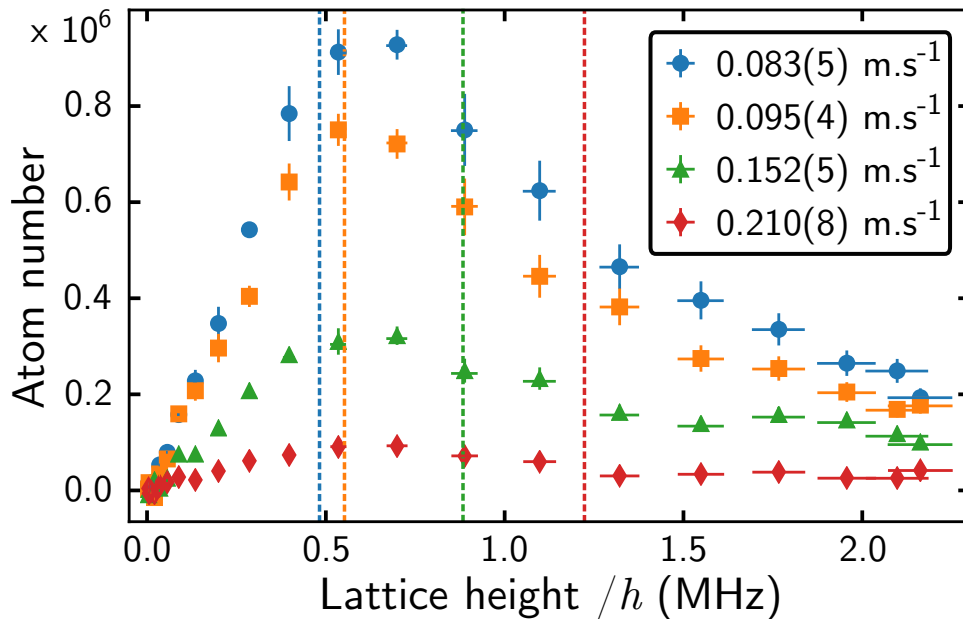
FIGURE 5.3: Measured steady-state number of atoms slowed by the SOLD and loaded in the reservoir, for varying lattice height and four different initial velocities. The dash vertical lines give the criterion of eq. (5.1) for $m = 1$. The vertical error bars represents standard errors from binned data points. The horizontal error bars origin is described in Section 5.6.5.

potential. In Fig. 5.4(a), we plot the dependence of the average energy lost per pump cycle E_{lost} with incoming velocity v and lattice height. For high kinetic energies compared to the lattice height $\frac{1}{2}mv^2 \gg U_{\text{lat}}$, atoms travel through several lattice sites and the energy lost saturates to $E_{\text{lost}} \to U_{\text{lat}}/2$ provided that $v \gg \lambda_{\text{lat}}\Gamma$. A striking feature of Fig. 5.4(a) is that E_{lost} exhibits an efficiency peak for $\frac{1}{2}mv^2 = U_{\text{lat}}$. In this case, atoms have just enough energy to climb one lattice maximum, where they spend most of their time and are thus more likely to undergo spontaneous emission. The energy lost asymptotically reaches $E_{\text{lost}} \to U_{\text{lat}}$ for $v \gg \lambda_{\text{lat}}\Gamma$ (see Section 5.6.2).

An important benchmark for a laser cooling technique is the average number of photons which needs to be scattered to slow atoms from some initial velocity to the final velocity allowed by this technique. In Fig. 5.4(b) we calculate the number of pumping photons needed to reach a kinetic energy equivalent to a temperature below $2\,\mu\text{K}$. This temperature was arbitrarily chosen ~ 4 times larger than the recoil temperature associated with the $^1\text{S}_0 - {}^3\text{P}_1$ transition, the relevant cooling limit in our case. For comparison with radiation pressure based laser cooling methods, we also show in Fig. 5.4(b) the number of photons required in the case of a Zeeman slower (ZS) [120]. The SOLD requires always less cooling photons than the ZS for a lattice
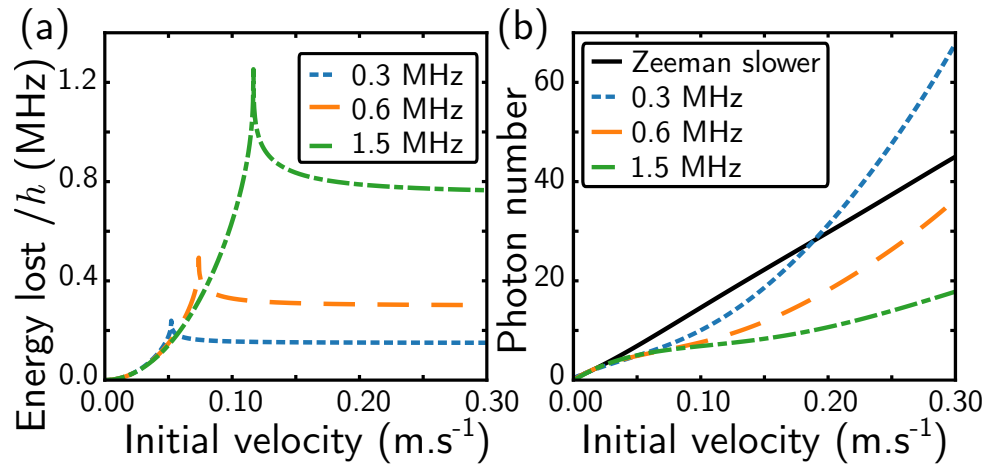
FIGURE 5.4: Efficiency of our cooling scheme for varying initial velocity. (a) Average energy E_{lost} lost during the first cooling cycle. (b) Number of cycles/pumping photons needed for the SOLD compared with a Zeeman slower. The plain black line shows the behavior of the ZS, while the dotted, dashed and dash-dotted lines are for the SOLD with lattice heights $U_{\mathrm{lat}} = h \times 0.3\,\mathrm{MHz}$, $0.6\,\mathrm{MHz}$ and $1.5\,\mathrm{MHz}$, respectively.

height satisfying $U_{\mathrm{lat}}/h > v/\lambda_{\mathrm{lat}}$.

The SOLD ability to slow atoms with high incoming velocities is strongly dependent on the pumping rate. We model this rate by solving the optical Bloch equations for a two-level system in dependence of velocity and lattice height. Assuming a constant velocity, we numerically solve for the average population in $^3\mathrm{P}_1$ (see Section 5.6.2), which we show in Fig. 5.5(a). The remarkable feature in Fig. 5.5(a) is the presence of multiple resonances where there are high pumping rates. These can be explained by in-phase multiple π-over-N pulses. Indeed, only at the bottom of a lattice site is the detuning small enough to pump a significant population to $^3\mathrm{P}_1$. While the atoms propagate from one site to the next, the $^1\mathrm{S}_0$ and $^3\mathrm{P}_1$ states acquire different phases. Once at the next site, further population is efficiently pumped to $^3\mathrm{P}_1$ only if the dephasing is equal to multiples of 2π, see Fig. 5.5(b). This criterion on the dephasing leads to the relation

$$\frac{U_{\mathrm{lat}}}{h} = m \times \frac{4v}{\lambda_{\mathrm{lat}}}, \tag{5.1}$$

with $m \in \mathbb{N}$ and h the Planck constant. The optimums in loading efficiency observed in Fig. 5.3 correspond mainly to the fulfillment of this criterion for the case $m = 1$. Including both the average lost energy E_{lost} and the pumping rate, we model the behavior of the SOLD and reproduce qualitatively the features of the experimental

TABLE 5.1: Comparison of the SOLD and the Zeeman slower (ZS). The rows give steady-state atoms numbers, fluxes, $1/e$ loading times, and radial (axial) temperatures T_{rad} (T_z). The various configurations are, in order, the SOLD in the transport guide, the SOLD plus the reservoir trap (R), the ZS plus reservoir and the combination of both techniques.

	SOLD	SOLD+R	ZS+R	SOLD+ZS+R
Atom ($\times 10^6$)	0.78(01)	0.69(01)	1.87(04)	2.00(10)
Flux ($\times 10^6\,\text{s}^{-1}$)	0.74(04)	0.65(03)	2.11(14)	2.80(15)
Loading (ms)	705(20)	625(52)	434(43)	507(55)
T_{rad} (μK)		1.53(02)	1.08(04)	1.34(02)
T_z (μK)		2.30(06)	5.67(94)	2.59(10)

data, see Section 5.6.2. Moreover, we find that the criterion of eq. (5.1) with $m = 1$ dictates the capture velocity of the SOLD, which reads $v_c = U_{\text{lat}}\lambda_{\text{lat}}/4h$. For a lattice height thus matching the atoms' velocity, the SOLD requires less photons than standard radiation pressure based laser cooling methods like the Zeeman slower.

We now compare experimentally the SOLD performance with that of a Zeeman slower. To this end, we add a laser beam counter-propagating to the transport guide, focused in the SOLD region and with a circular polarization set to address the $m_{\text{J}} = -1$ Zeeman sub-state. We demonstrated in previous work that it is possible to operate a ZS on the narrow Sr intercombination line [68]. We report in Tab. 5.1 a comparison between the two slowing methods. Both give similar results for fluxes and final atom numbers, with an advantage for the ZS, which we attribute mainly to the spatial selectivity of its optical excitation. However, we observe a clear difference in the final axial temperatures T_z within the reservoir, which effectively reflects the final mean velocities. For the SOLD, T_z is almost as low as the radial temperature T_{rad} provided by the molasses cooling, whereas T_z is 2.5 times hotter for the ZS. This is because a Zeeman slower is unable to decelerate atoms to zero velocity, as they remain somewhat resonant with ZS photons and are pushed backwards. On the contrary, for the SOLD the final mean velocity is stationary in the frame of the optical lattice, whose velocity can be set at will by the frequency difference between lattice beams [158, 159].

An additional difference is that, since the SOLD does not rely on radiation pressure from the pumping beam to cool, it is possible to use a much broader class of transitions than for standard laser cooling methods. It is for example possible to use the ZS beam as a pumping beam that features both spatial and velocity selectivity. The lattice, now acting on atoms in $^3\text{P}_1\, m_{\text{J}} = -1$, is the one charged with decelerating atoms to zero

axial velocity. In presence of both lattice and ZS beams, we observe the best number of atoms in the reservoir, while keeping the low temperature T_z due to the SOLD, see Tab. 5.1.

Let us now turn to considerations for further applications of this cooling scheme. Firstly, it is clear from Fig. 5.5(a) that, at high velocities, pumping rates are low unless the lattice height matches the conditions of eq. (5.1). This can be dealt with by temporal modulation of the lattice intensity, which varies the resonance locations. Secondly, for lattices much higher than the transport guide depth, we observe a clear spread of the atomic beam out of the guide. This is due both to the radial anti-confinement from the blue-detuned lattice beams and the slight angle between lattice and transport beams. A red-detuned lattice could remedy this by confining the atoms radially, but this will make correctly tuning the pumping frequency dependent on the lattice intensity. Thirdly, if the lattice detuning Δ_{lat} is insufficient, atoms in the $^3\text{P}_1$ state can be optically pumped by the lattice light to $^3\text{S}_1$ (see Section 5.6.4), where they can decay to the metastable $^3\text{P}_0$ and $^3\text{P}_2$ states, introducing a need for repumping [160]. Finally, the initial velocities decelerated in this proof of principle are low compared with several applications of interest, in part due to the small lattice deceleration region used. In the proposal of Wu et al. [34], the lattice is $78.5\,\text{MHz}$ high and the capture velocity is set to $v_{c,\bar{H}} \approx 25\,\text{m.s}^{-1}$. It would take about 20 photon scattering events for the SOLD to bring antihydrogen close to the recoil limit, which, as seen in Fig. 5.4(b), is similar to the numbers demonstrated in this work. If we consider the same velocity and lattice height for much heavier elements such as strontium, the number of photons required by the SOLD is about 1700, much lower than the ZS case of 3700.

5.5 Conclusion

To summarize, we experimentally demonstrate the feasibility of a Sisyphus-type decelerator first proposed in a slightly different form to laser cool antihydrogen [34, 33, 133, 134]. The efficiency of this decelerator is characterized in the steady-state regime both experimentally and theoretically in dependence of incoming atom velocities and lattice heights. We determine the capture velocity of this technique, and compare the SOLD with a Zeeman slower, where we show axial temperatures a factor of 2.5 lower. With both techniques combined, we profit from both the ZS spatial/velocity selectivity and the SOLD end temperatures. Finally, we briefly
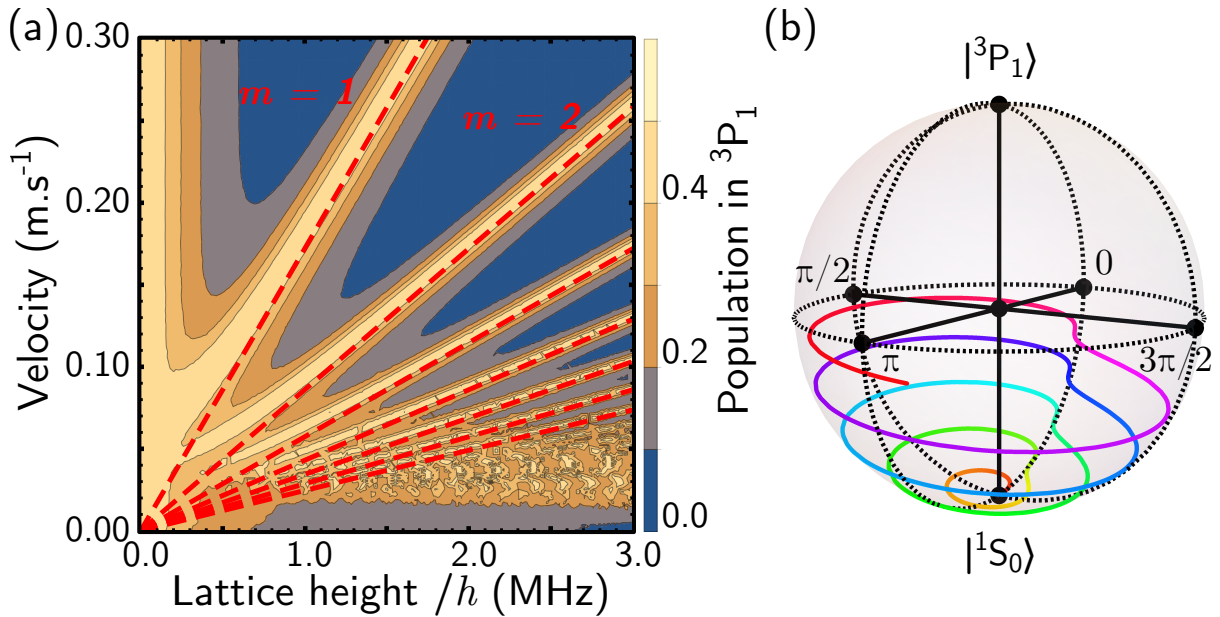
FIGURE 5.5: (a) Population transferred to the $^3P_1$ state depending on the lattice height and the atom velocity. For clarity of the figure, the population is calculated for a saturation parameter of the pumping transition of ~ 1600 instead of the $0.1 \sim 10$ typically used. Dashed red lines show the condition of eq. (5.1) for $m \in \{1...7\}$. (b) Short time evolution of the bloch vector (for 5 "pulses") in the case of in-phase excitation satisfying eq. (5.1) with $m = 1$.

consider some improvements and applications to the case of antihydrogen. In order to efficiently slow atoms the SOLD method requires only three simple requirements; a three level system, selective pumping in a lattice with $U_{\text{lat}} \gg \hbar\Gamma$, and an initial velocity satisfying $v > \lambda_{\text{lat}}\Gamma$. Such simple requirements can be fulfilled by many systems where laser cooling to the ultracold regime remains a challenge, such as new exotic species and (polyatomic) molecules [136, 138, 139, 142, 140, 137, 141]. Moreover, by careful choice of the time sequence for the lattice velocity and intensity, a pulsed version of the SOLD could bring an atom wavepacket to any desired velocity while scattering only a handful of photons.

Note added Recently, we became aware of related Sisyphus cooling in optical tweezers [57].

5.6   Supplemental Material

5.6.1   Sisyphus Optical Lattice Accelerator

The SOLD deceleration scheme brings atoms ultimately to zero mean velocity in the reference frame of the lattice. By applying a small frequency difference between two lattice beams, a lattice will move at a well-controlled velocity [158, 159]. This implies that the SOLD can ideally decelerate or accelerate atoms to any desired velocity. We test this using a $1.53(2)\,\mu$K stationary cloud produced by loading a MOT into a dipole trap, at the location of the lattice. We shine both lattice and pumping light onto this cloud for $100\,\mu$s, and after $20\,$ms observe the number of atoms in a displaced cloud corresponding to the moving lattice frame. The results are shown in Fig. 5.6. We observe an increase in the displaced fraction with lattice height, which we attribute to the increase in energy $\sim U_{\text{lat}}/2$ given to the atoms for each scattering event. We also observe an optimal lattice velocity for a given lattice height, which roughly corresponds to our model criterion of eq. (5.7) with $m = 1$. The variation in the location of these efficiency peaks is more visible in Fig. 5.6 than in Fig. 5.3, because here the SOLD is pulsed for a short duration instead of operating in the steady-state regime, so the effects of each resonance corresponding to eq. (5.7) are more pronounced. Note that due to the initial size of the cloud and its location with respect to the lattice, our estimation of the effective lattice depth is much rougher than for the data of Fig. 5.3.

We can also use the moving lattice to characterize our reservoir dipole trap. The loading of this reservoir is both sensitive to the mean velocity of atoms and to the location they end up when reaching zero mean velocity. We characterize the velocity acceptance of the reservoir by varying the frequency difference between the two lattice beams. The loading efficiency of the reservoir depending on the lattice velocity is shown in Fig. 5.7. It can be fitted by a Gaussian whose width is $\sigma_v = 0.0084(4)\,$m.s^{-1}, centered at $v_{\text{R}} \sim -0.002\,$m.s^{-1}. This slight departure from zero velocity can be explained by the orientation of the reservoir relative to the guide, which favors the loading of atoms that move backward. We include this measured velocity selectivity of the reservoir in our model of the SOLD.
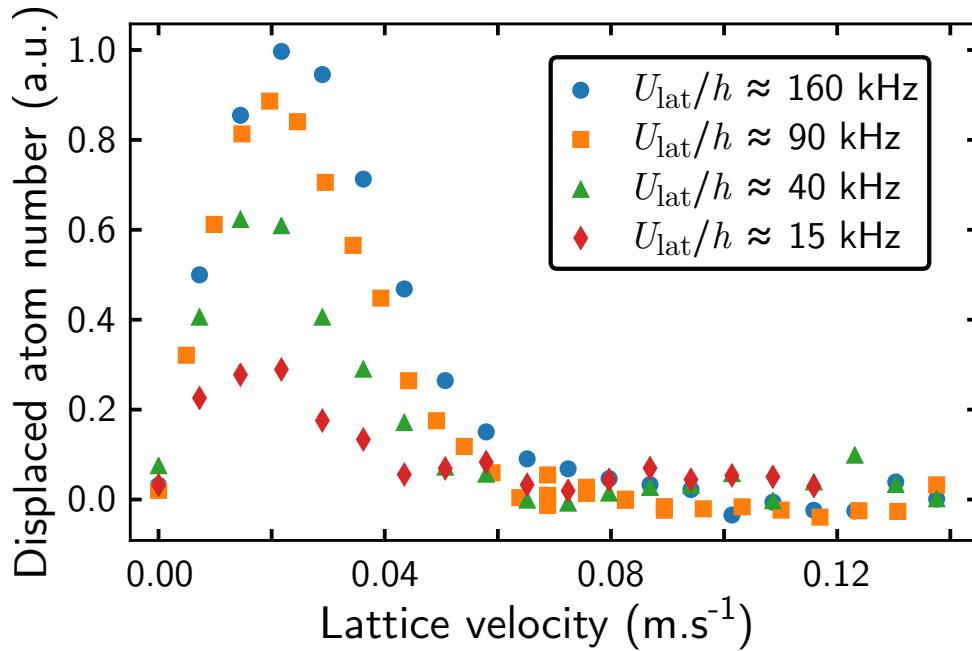
FIGURE 5.6: Acceleration of a stationary strontium cloud by a moving lattice, for various lattice heights. The abscissa gives the lattice velocity and the ordinate, in arbitrary units, is proportional to the fraction of atoms in the moving frame measured after $100\,\mu s$ of acceleration followed by $20\,ms$ of evolution.

5.6.2 SOLD Model

Here we give a description of our model of the SOLD that is an extended version of the description given in the main text.

In order to model our cooling scheme in an insightful way, we split the problem into two parts: the average energy lost per cooling cycle and the pumping rate. We then use both results to simulate the time evolution of the atoms' velocity.

Energy lost

We begin with a study of the energy lost due to the presence of the lattice. We assume that the atoms are optically pumped into the $^3\mathrm{P}_1$ state at the bottom of the lattice and we solve the differential equation for the motion $z(t)$ along the lattice propagation axis:

$$\frac{1}{2}mv_0^2 = U_{\text{lat}}\sin^2 k_{\text{lat}}z + \frac{1}{2}m\left(\frac{dz}{dt}\right)^2 , \; z(t=0) = 0, \tag{5.2}$$
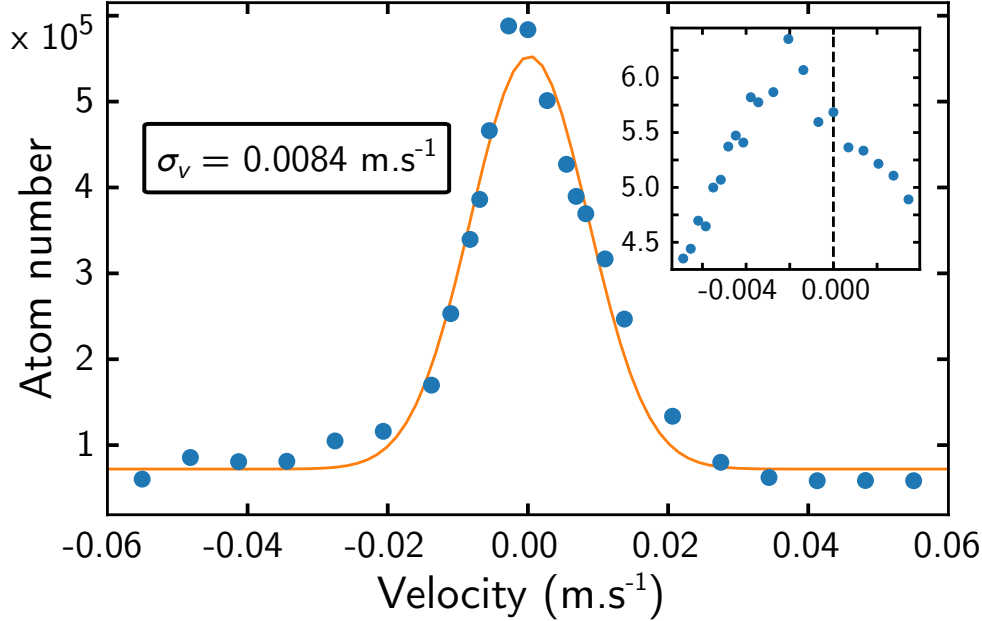
FIGURE 5.7: Velocity selectivity of the reservoir loading, measured by varying the lattice velocity. The line is a Gaussian fit of the data with width σ_v. The inset shows the same type of measurement on a much narrower velocity range, highlighting the center velocity of about $v_R \sim -0.002 \, \text{m.s}^{-1}$.

with m and v_0 being respectively the mass and the initial velocity of the atom. U_{lat} is the lattice depth and $k_{\text{lat}} = \frac{2\pi}{\lambda_{\text{lat}}}$ is the wave vector of the lattice light with wavelength λ_{lat}. The solution of this equation can be written in terms of the Jacobi amplitude J_A:

$$z(t) = \frac{1}{k_{\text{lat}}} J_A \left(k_{\text{lat}} v_0 \, t, \frac{2U_{\text{lat}}}{m v_0^2} \right). \tag{5.3}$$

Since the process relies on spontaneous emission towards $^1\text{S}_0$, we determine the average energy lost $E_{\text{lost}}(U_{\text{lat}}, v_0)$ by integrating the lattice height explored for a duration set by the natural linewidth Γ of the $^1\text{S}_0 - {}^3\text{P}_1$ transition,

$$E_{\text{lost}} = \Gamma \int_0^\infty e^{-\Gamma t} \, U_{\text{lat}} \sin^2(k_{\text{lat}} z(t)) \, dt. \tag{5.4}$$

In Fig. 5.4, we show the evolution of E_{lost} for several lattice heights and depending on the incoming velocity. We observe that for high incoming kinetic energies compared to the lattice height $\frac{1}{2} m v_0^2 \gg U_{\text{lat}}$, the energy lost E_{lost} saturates. In this case, atoms travel through several lattice sites, and their propagation tends to $z(t) \rightarrow \frac{1}{k_{\text{lat}}} J_A (k_{\text{lat}} v_0 \, t, 0) = v_0 \, t$. Equation (5.4) gives the relation

$E_{\text{lost}} \to \frac{U_{\text{lat}}}{2} / \left(1 + \left(\frac{\Gamma}{2k_{\text{lat}}v_0}\right)^2\right)$. In our experiment $v_0 \gg \lambda_{\text{lat}}\Gamma$, so the average energy lost saturates to $U_{\text{lat}}/2$. One striking feature of Fig. 5.4(a) is that the energy lost exhibits a sharp resonance for $\frac{1}{2}mv_0^2 = U_{\text{lat}}$, where cooling is the most efficient. In this case, atoms have just enough energy to climb on top of the first lattice hill, so they spend most of their time at this location, which makes them more likely to spontaneously emit there and therefore to lose most of their kinetic energy. Indeed, the explored lattice height becomes $U(t) \to U_{\text{lat}} \tanh^2(k_{\text{lat}}v_0 t)$, which for $v_0 \gg \lambda_{\text{lat}}\Gamma$ gives an average energy lost reaching asymptotically $E_{\text{lost}} \to U_{\text{lat}}$. Let us note that, in contrast to Ref. [34], which relies also on a spatial modulation of Γ, the effective rate of spontaneous emission in our case is higher on lattice hills only because of the increased time atoms spend there.

Pumping rate

We now examine the pumping rate in dependence of the incoming velocity and lattice height. We solve the optical Bloch equation for a two-level system corresponding to the $^1S_0$ and $^3P_1$ states, coupled by the pumping laser with Rabi frequency Ω. The time-dependent Schrödinger - von Neumann equation for the density operator ρ is

$$\frac{d\rho}{dt} = -\frac{i}{\hbar}[H, \rho] + L,\qquad(5.5)$$

with $\hbar$ the reduced Planck constant, L the usual term to account for the spontaneous emission due to Γ, and with the Hamiltonian H written as:

$$H = \begin{pmatrix} 0 & \Omega/2 \\ \Omega/2 & U_{\text{lat}} \sin^2(k_{\text{lat}}v_0 t) \end{pmatrix}.\qquad(5.6)$$

We numerically solve eq. (5.5) with time, starting with all the population in $^1S_0$ at $t = 0$. For this calculation, we assume a constant velocity v_0, which is valid for $\frac{1}{2}mv_0^2 \gg U_{\text{lat}}$. After a variable time, the $(\Omega, U_{\text{lat}}, v_0)$-dependent solution for the excited population reaches a steady-state only slightly perturbed by the time-dependent detuning produced by travelling within the lattice. Averaging over this small perturbation, we get the population in the $^3P_1$ state shown in Fig. 5.5.

The remarkable feature in this figure is the presence of sharp lines where the excited population is the highest. These can be simply explained by looking at the evolution of the Bloch vector associated with ρ, displayed in Fig. 5.8. When the atoms
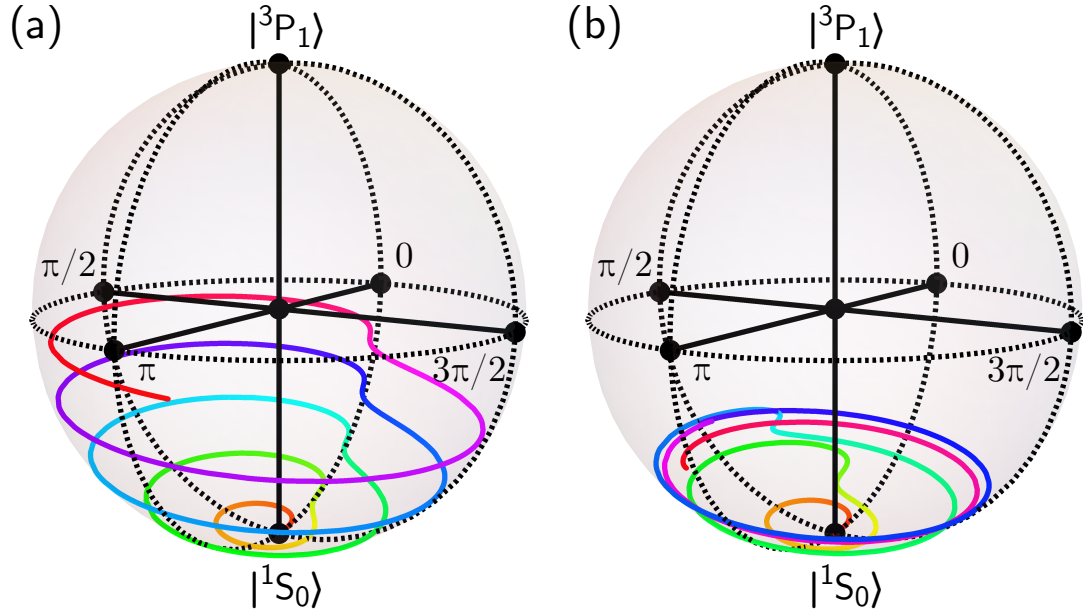
FIGURE 5.8: Evolution of the Bloch vector on the Poincaré sphere, shortly after the application of the SOLD. Atoms begin in the $^1\mathrm{S}_0$ state at the location of a lattice site. The saturation parameter of the pumping to $^3\mathrm{P}_1$ is set for clarity to about 60, and the lattice height is $h \times 600\,\mathrm{kHz}$. The velocity in (a) $v_0 = 0.1035\,\mathrm{m.s}^{-1}$ is such that the accumulated phase during the travel time between two sites is close to $\Phi = 2\pi$, while in (b) where $v_0 = 0.09\,\mathrm{m.s}^{-1}$ this condition is not met.

are not located at the bottom of a lattice site, the detuning is so strong that effectively the scattering rate vanishes, so the population distribution remains roughly constant for timescales short relative to Γ. Due to the dephasing between both states, the Bloch vector then evolves mainly horizontally, until the atoms reach the location of the bottom of the next lattice site. If at that moment the dephasing amounts to a multiple of 2π, then the effective pumping pulses add constructively, and the steady-state excited population is high. This leads to the resonance lines in Fig. 5.5.

We can give a simple quantitative criterion for the positions of these lines. The phase accumulated during the propagation through one lattice period is $\Phi = \Delta T$, with $T = \frac{\lambda_{\text{lat}}}{2v_0}$ the propagation time and Δ the dephasing, taken as the average detuning due to the lattice, giving $\Delta = 2\pi \frac{1}{h} \frac{U_{\text{lat}}}{2}$, with h the Planck constant. The condition $\Phi = m \times 2\pi$ (with $m \in \mathbb{N}$) gives the relation:

$$\frac{U_{\text{lat}}}{h} = m \times \frac{4v_0}{\lambda_{\text{lat}}}. \tag{5.7}$$

This criterion is shown as dashed red lines for $m \in \{1, ..., 7\}$ in Fig. 5.5.

Overall evolution

In order to model the complete behavior of the SOLD, we solve classically the evolution of the atoms' velocity v with time, under an effective force $F(U_{\text{lat}}, v) = -\Gamma \times \rho_{^3P_1}(U_{\text{lat}}, v) E_{\text{lost}}(U_{\text{lat}}, v)$. We carry out this calculation for a packet of atoms whose velocity distribution follows a (1D) Boltzmann distribution corresponding to the temperature of our MOT of $6\,\mu$K summed with an offset corresponding to the measured mean velocity given by the launch beam. The capture probability in our reservoir is determined by the velocity-dependent efficiency extracted from the measurement shown in Fig. 5.7, corresponding to a Gaussian function with a width $\sigma_v = 0.0084\,\text{m.s}^{-1}$. We thus simulate the time evolution of the loaded population in the reservoir depending on the lattice height, for the four mean starting velocities shown in Fig. 5.3. In Fig. 5.9 we compare the results from this model with our experimental data.

We see a good qualitative agreement concerning the overall behavior with both lattice height and starting mean velocity. In particular, the locations of the optimums of loading efficiency are well reproduced by our model. These correspond to the case when the starting mean velocity v_0 verifies the criterion of eq. (5.7) (with $m = 1$). Indeed, in that case atoms are efficiently pumped to the $^3P_1$ state, and lose typically a significant amount of energy $U_{\text{lat}}/2$. After spontaneous emission, their velocity is much lower and atoms are in the (U_{lat}, v) region where the density of lines for $m \geq 2$ is high. They are therefore very likely to keep decelerating efficiently. On the contrary, for high velocity v_0, in the region $0 \ll \frac{U_{\text{lat}}}{h} \ll \frac{4v_0}{\lambda_{\text{lat}}}$, atoms will not get pumped to $^3P_1$. Our model is thus able to estimate the capture velocity v_c of the SOLD, which is given by

$$v_c = \frac{U_{\text{lat}}\lambda_{\text{lat}}}{4h}. \tag{5.8}$$

Let us note that our model makes several approximations. Indeed the results of the calculations shown in Fig. 5.9(b) are given for one particular evolution time $t = 1.4\,\text{ms}$ that has been chosen for best match with the steady-state experimental data. Since no decay mechanism has been added in the model, the final loading would be with unity efficiency. This chosen deceleration time is rather short, because in this case the saturation parameter of the $^1S_0 - ^3P_1$ transition is set to ~ 320, for which the calculations suffer less numerical errors compared to more realistic, lower saturation parameters. Nonetheless, the theory always exhibits the same overall behavior no matter the value of the saturation parameter. Another limitation of our model is that no selection criteria
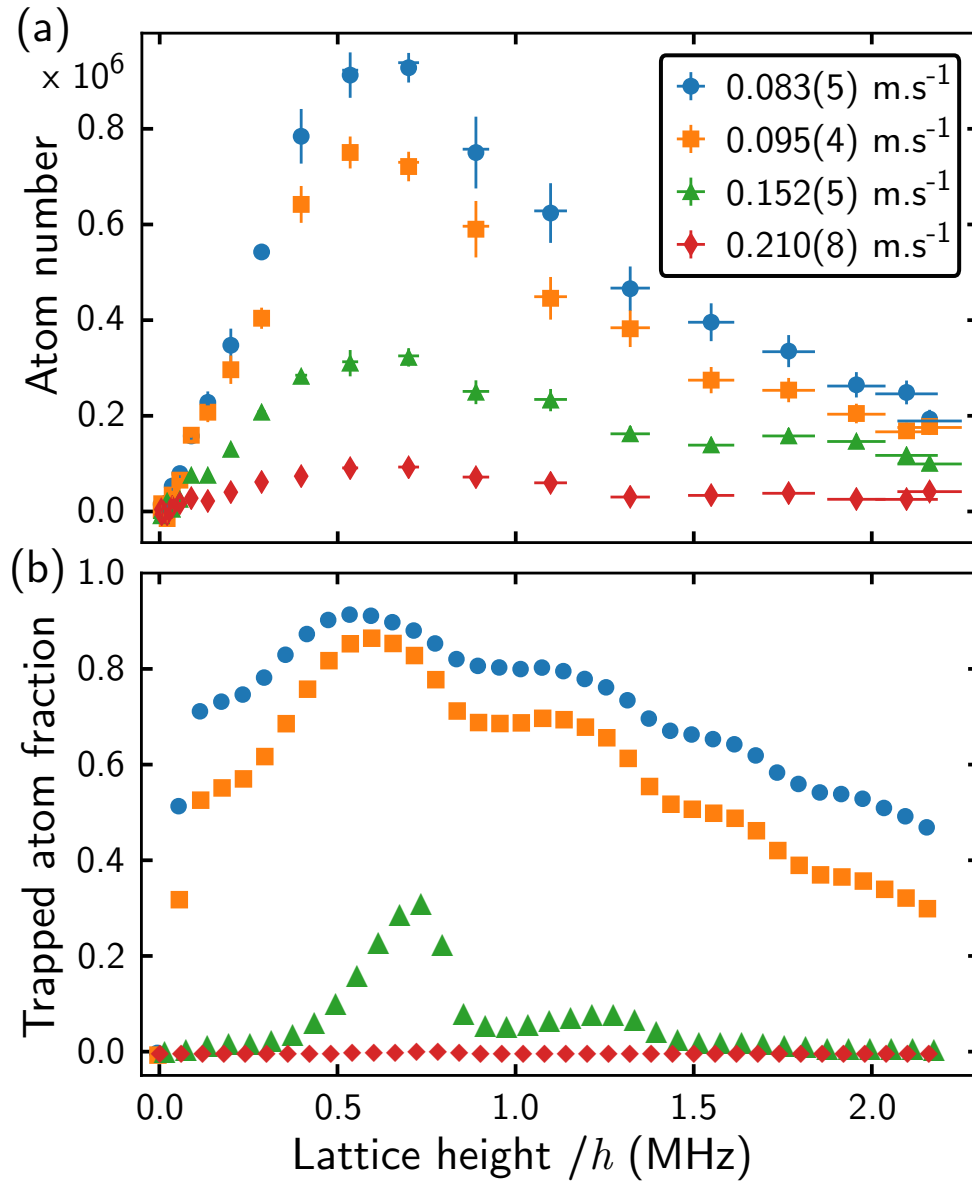
FIGURE 5.9: Comparison between (a) the experimental data already shown in Fig. 5.3 and (b) the results of the theoretical model (see text) for the same initial mean velocities.

have been chosen for the position of atoms, whereas they must be in the vicinity of the crossing between the transport guide and reservoir to be loaded. Similarly, atoms expelled from the guide by the barrier formed by the blue detuned lattice and the effects of the lattice's slight angle with the guide are not taken into account. Finally, the constant velocity approximation made when solving the optical Bloch equations is not valid for $\frac{1}{2}mv_0^2 \leq U_{\text{lat}}$. To obtain a better quantitative agreement, Monte-Carlo simulations could be a straightforward option for further studies.

5.6.3 Atomic beam velocities

In order to characterize the dependence of the SOLD efficiency with incoming atom velocity, we need a measurement of the mean atom velocity within the transport guide before entering the lattice region. In the absence of the SOLD, we will assume the mean velocity to be constant throughout the lattice region, as the potential provided by the transport guide in this location is engineered to be flat in the axial direction.

We measure the atom velocity arriving at the location of the lattice by two methods. The first is to eject a burst of atoms out of the transport guide using a pulse of light resonant with the $^1\text{S}_0 - {}^1\text{P}_1$ transition. The pulse lasts $1\,\text{ms}$ and the laser beam propagates horizontally perpendicular to the atomic beam. We assume that spontaneously emitted photons are equally distributed in all directions during the ejection process, so that the on-axis mean velocity is not affected by the light absorption. By examining the propagation of the packet of ejected atoms, we can infer the mean velocity, see Fig. 5.10. We were only able to measure the mean velocity with high accuracy, as measurements of the axial distribution or temperatures of these ejected clouds were limited by low signal to noise. Rough estimates were however consistent with the measured MOT temperature of $6\,\mu\text{K}$.

We use a second method as a cross-check for our determination of the atom mean velocity. It relies on the measurement of the loading in the transport guide region. Without the SOLD applied, we measure the steady-state atom number in the transport guide in the region corresponding to the extent of the lattice. We can extract the linear density ρ_{lin} in this region, if assumed to be homogeneous. By also assuming the mean velocity v_0 to be constant, we have the following relation for the steady-state incoming and outgoing flux:

$$F_{\text{lat,out}} = F_{\text{lat,in}} = \rho_{\text{lin}} \times v_0. \tag{5.9}$$
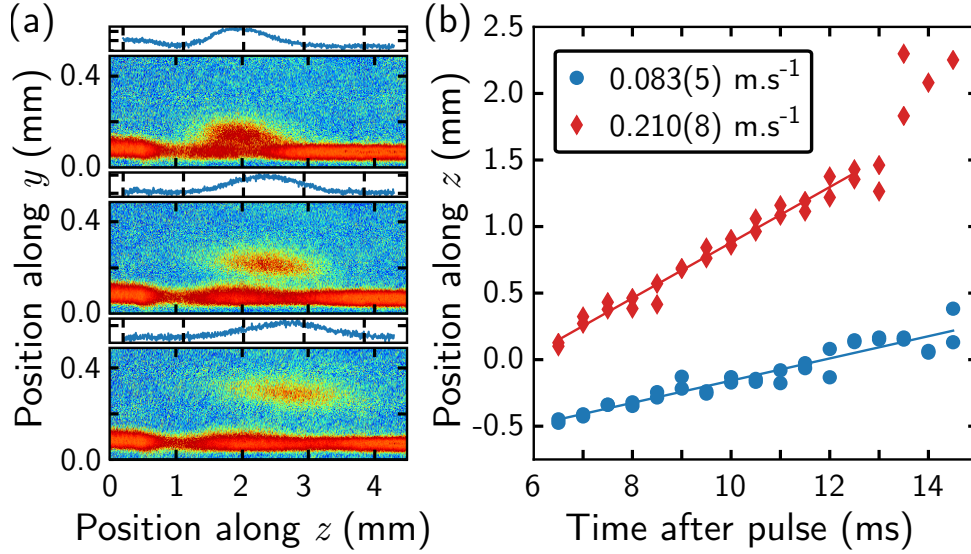
FIGURE 5.10:   Measure of the atom beam velocity. (a) Absorption images and respective density profiles of clouds of atoms ejected from the transport guide, taken $5\,\mathrm{ms}$ (top), $8\,\mathrm{ms}$ (middle) and $10\,\mathrm{ms}$ (bottom) after the ejection pulse. The pulse is applied at $z \approx 1\,\mathrm{mm}$. (b) Evolution of the position along the z axis of two ejected clouds with different mean velocities. The lines are fits from which we extract the velocities.

We thus need to measure $F_{\mathrm{lat,out}} = F_{\mathrm{lat,in}}$, which we get from the loading curves of the MOT and the transport guide. The rate equations for both MOT and transport guide atom numbers, N_{MOT} and N_{TG}, are

$$\begin{cases} \frac{dN_{\mathrm{MOT}}}{dt} = F_{\mathrm{in}} - \beta_{\mathrm{TG,in}}\, N_{\mathrm{MOT}} - \beta_{\mathrm{MOT,loss}}\, N_{\mathrm{MOT}} \\[2em] \frac{dN_{\mathrm{TG}}}{dt} = \eta_{\mathrm{TG}}\, \beta_{\mathrm{TG,in}}\, N_{\mathrm{MOT}} - \beta_{\mathrm{TG,out}}\, N_{\mathrm{TG}} \end{cases}, \qquad (5.10)$$

where F_{in} is the flux coming into the MOT, see Ref. [68]. The loss rate $\beta_{\mathrm{MOT,loss}}$ describes atoms lost from the MOT, while $\beta_{\mathrm{TG,in}}$ describes the rate of atoms coupled into the beginning of the transport guide. The efficiency η_{TG} accounts for the losses between the start and the end of the guide. Last, the rate $\beta_{\mathrm{TG,out}}$ describes atoms leaving the lattice region. We thus have $\beta_{\mathrm{TG,out}}\, N_{\mathrm{TG}}(t = \infty) = F_{\mathrm{lat,out}} = F_{\mathrm{lat,in}}$. From fitting the loading curves of both MOT and transport guide with the solutions of eq. (5.10), we extract the values of each β, F and η parameters, and ultimately get the value of v_0. We found a good agreement between the velocities derived from both methods, and we use the first one to determine the values provided in the main text.
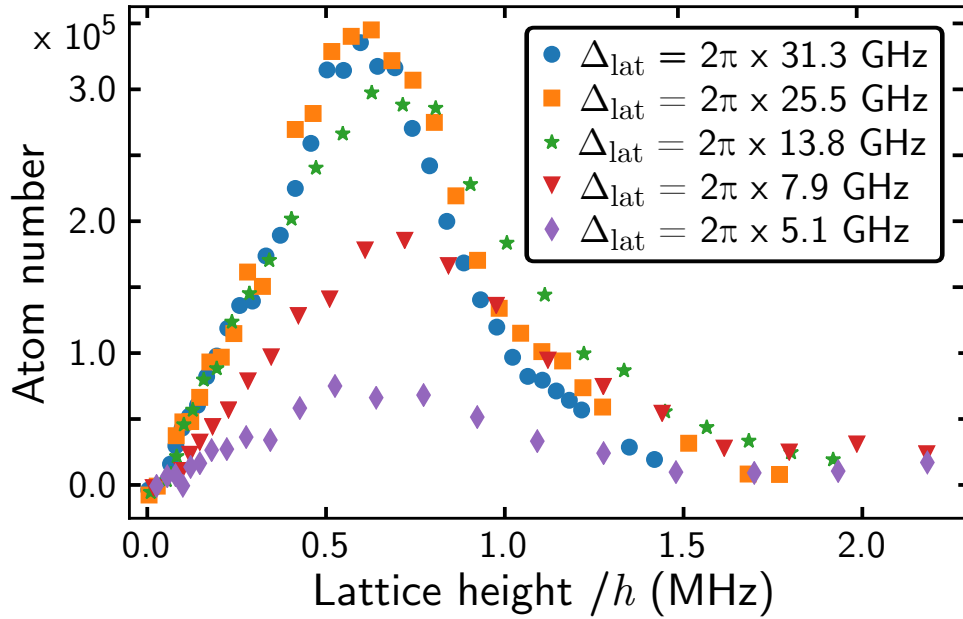
FIGURE 5.11: Effect of optical pumping by the lattice light to the $^3S_1$ state. The data show the number of atoms loaded into the reservoir as a function of the lattice height for various detunings of the lattice laser from the $^3P_1 - {}^3S_1$ transition.

5.6.4 Losses toward $^3S_1$

One limitation of our decelerator is the optical pumping by the lattice light of atoms in the $^3P_1$ state to the $^3S_1$ state. If such optical pumping occurs, atoms can decay from $^3S_1$ to the metastable $^3P_0$ and $^3P_2$ states and exit the cooling cycle. Fig. 5.11 shows, for several lattice laser detunings Δ_{lat}, the effect of optical pumping to $^3S_1$ depending on the lattice height. For detunings a few GHz away from the $^3P_1 - {}^3S_1$ transition we see a clear reduction of the atom number slowed and captured in the reservoir. For detunings above $20\,\mathrm{GHz}$, the efficiency seems to converge toward a unique curve, indicating no significant optical pumping.

A repumping scheme such as the one used in Ref. [160] can optically pump atoms back to $^3P_1$. Apart from a few additional photon recoils, this method should not significantly affect the slowing process, providing the repumping time is short compared to the propagation of the atoms along the lattice. Another simple method is to detune the lattice laser frequency further away from the $^3P_1 - {}^3S_1$ transition, while adapting its power to keep the same lattice height. Aside from the data of Fig. 5.11, we operate at a lattice detuning of $\Delta_{lat} \approx 2\pi \times 30\,\mathrm{GHz}$, for which optical pumping is negligible.

TABLE 5.2: Relative uncertainties on the relevant parameters used to calculate the lattice height for the ^{3}P$_1$ state.

	uncertainty
Lattice beam power P	$\pm 3.0\,\%$
Lattice beam waist w_0	$\pm 1.4\,\%$
Lattice frequency detuning Δ_{lat}	$\pm 0.1\,\%$
Total transition rate $A_{^3\mathrm{P_J}-^3\mathrm{S_1}}$	$\pm 1.0\,\%$
Total uncertainty	$\pm 4.2\,\%$

5.6.5 Lattice height determination

An accurate determination of the lattice height is essential for the characterization of the SOLD. The potential of a 1D lattice acting on the ^{3}P$_1$ state is given by

$$U(z) = -\frac{1}{2\epsilon_0 c}\,\alpha_i\,I(z) = -\frac{4P}{\pi\epsilon_0 c\,w_0^2}\,\alpha_i\,\sin^2 k_{\mathrm{lat}}\,z, \qquad (5.11)$$

where α_i is the dynamic dipole polarizability of the ^{3}P$_1$ state, P is the power of each lattice beam, and w_0 is their waist. In the two-level approximation,

$$\alpha_i \approx \frac{3\epsilon_0\lambda_{\mathrm{lat}}^3}{8\pi^2}\frac{\Gamma_{\mathrm{eff}}}{\Delta_{\mathrm{lat}}}, \qquad (5.12)$$

where ϵ_0 is the vacuum permittivity. The approximation is valid because the lattice laser detuning Δ_{lat} is only a few tens of GHz. The effective rate $\Gamma_{\mathrm{eff}} = \eta\,A_{^3\mathrm{P_1}-^3\mathrm{S_1}}$ is the effective transition rate for the $5s5p\,^3\mathrm{P_1} - 5s6s\,^3\mathrm{S_1}$ transition, with $\eta = 1/2$ due to the lattice laser polarization. The relative uncertainties of the parameters contributing to the determination of the lattice height are listed in Tab. 5.2. All parameters and their uncertainties are determined experimentally, except for the transition rate, which we derive from literature in the following manner.

The $^3\mathrm{P_J} -^3 \mathrm{S_1}$ manifold transition rates are known accurately to the percent level. In Ref. [62], *ab-initio* calculated matrix elements for the relevant contributing transitions, together with experimental transition energies, are used to evaluate the ^{3}P$_0$ polarizability. Constraints from both the measurement of the magic wavelength at $813\,\mathrm{nm}$ and the dc polarizability are then imposed to fine-tune the dominant matrix element terms, in order to agree with the experimental values. The fine-tuning of these matrix elements does not exceed $1.1\,\%$, and the theoretical transition rate for $^3\mathrm{P_1} - ^3\mathrm{D_1}$ calculated from these matrix elements agrees with the measured value [161]

to within $0.2\,\%$.

From the dipole matrix elements of $5s5p\,^3\mathrm{P}_0 - 5s6s\,^3\mathrm{S}_1$ calculated in Ref. [62], we determine the value of $A_{^3\mathrm{P}_1-^3\mathrm{S}_1}$. To this end, we calculate the branching ratios of the $^3\mathrm{S}_1$ state to the three $5s5p\,^3\mathrm{P}_\mathrm{J}$ fine structure states using Wigner 6-j symbols. We take into account the fine structure splitting of the states, which is on the order of a few $100\,\mathrm{cm}^{-1}$, and apply the frequency dependent correction factors to the branching ratios. The resulting branching ratios are from $^3\mathrm{S}_1$ to $(^3\mathrm{P}_0,\,^3\mathrm{P}_1,\,^3\mathrm{P}_2) = (12.02\,\%,\,34.71\,\%,\,53.27\,\%)$. Using these ratios, we derive the transition rate $A_{^3\mathrm{P}_1-^3\mathrm{S}_1} = 2.394(0.024) \times 10^7\,\mathrm{s}^{-1}$.

Chapter 6

Outlook

During the course of this thesis, we went from an empty lab to a steady-state high-PSD Sr MOT, and shortly afterwards demonstrated another three orders of magnitude improvement in PSD, producing a steady-state ultracold Sr gas cloud near quantum degeneracy. A new type of deceleration mechanism employing an excited state Sisyphus cooling scheme is also demonstrated using Sr. Although our work was mainly focused on realizing a steady-state BEC, SrPAL project developments also open up broader prospects, in particular for future metrology and precision measurement schemes using Sr. We list in the following some of these prospects.

- In the steady-state high-PSD MOT experiment, we demonstrate the capability of producing a Sr sample continuously laser-cooled down to μK temperature, using a narrow-line transition. Combining our work with recent experimental work on Rydberg-dressed Sr atoms from the Durham group [162], a steady-state hybrid magneto-electro-optical trapped atomic cloud controllable by electric and magnetic fields is technologically achievable through off-resonantly coupling the ground state to a Rydberg state. This provides the means to combine the outstanding steady-state high-PSD Sr MOT performance with controllable coupling to strongly interacting states, suitable for metrological applications.

- In Chapter 4 we show a steady-state ^{88}Sr atomic beam with a high PSD of $\sim 1 \times 10^{-5}$ and demonstrate continuous loading of Sr atoms into a reservoir trap. This architecture or variations of it can be used to improve precision measurement, especially optical lattice clocks, in several ways. Firstly, the reservoir could serve as high-flux source of atoms for multiple clock ensembles that are interrogated in an interlaced manner. This could be done by moving atoms out of the reservoir into two interrogation regions using two moving

lattices. Since the two ensembles can be quite close to each other and use the same laser sources for manipulation, some common noise sources can be reduced compared to interrogating atomic ensembles in two different vacuum chambers. Secondly, the reservoir could serve as source of atoms to replenish the lasing ensemble in a superradiant clock [79]. Successful replenishment requires the transfer of dense, μK-cold atomic ensembles into the lasing ensemble with very little disturbing near-resonant light. This should be possible using SrPAL technology and we are currently adapting it to this task within the iqClock consortium[1]. Finally, if fermionic Sr atoms are used, such a reservoir can be used as a starting point to quickly produce large ensembles of quantum degenerate Sr for degenerate gas optical lattice clock. Beyond clocks, the atomic beam or reservoir could also be used as a source of atoms for atom interferometry, which can serve to detect accelerations and rotations as required for navigation [163], or even to detect gravitational waves and dark matter [115, 83, 164, 165].

- Our proof-of-principle experiment on Sisyphus cooling calls for a validation on hydrogen before applying it to antihydrogen in the antihydrogen apparatus at CERN. Laser cooling antihydrogen is the next milestone for these experiments, see the conclusion of Ref. [127]. Furthermore our implementation encourages the application of Sisyphus cooling to many ultracold experiments where laser cooling is challenging, such as laser cooling molecules, especially molecules with more than two atoms.

- In single atom optical tweezer experiments, techniques have matured into a powerful toolset for synthesising defect free atomic arrays. For alkaline-earth(-like) atoms, cooling during single-atom resolved imaging has been performed on the $^1S_0$ - $^3P_1$ intercombination line and therefore it was initially thought that the wavelength of the tweezer trapping light should be chosen to induce negligible differential light shifts on the laser cooling transition in order not to destroy the capacity for laser cooling. This constraint precludes the possibility to manipulate clock states using the optical clock transition ($^1S_0$ - $^3P_0$) because of the polarizability mismatch of the clock states. A recent result from the Caltech group [166] combined their independently developed Sisyphus cooling scheme with our Sisyphus scheme and applied it to cool Sr atoms in

---

[1]iqClock consortium: https://www.iqclock.eu

tweezers that do not induce a differential light shift on the clock transition. More generally this cooling scheme enables the use of a larger range of wavelengths for tweezers.

- For our team it is especially encouraging that the new deceleration method demonstrated in Chapter 5 results in better reservoir conditions, which is crucial to gain the missing factor of 2.6 in phase-space density on our way to a steady-state BEC and ultimately a continuous atom laser.

Bibliography

[1] T. H. Maiman, "Stimulated Optical Radiation in Ruby", *Nature* **187,** 493 (1960).

[2] A. Javan, W. R. Bennett, and D. R. Herriott, "Population Inversion and Continuous Optical Maser Oscillation in a Gas Discharge Containing a He-Ne Mixture", *Phys. Rev. Lett.* **6,** 106 (1961).

[3] B. P. Abbott et al., "Observation of Gravitational Waves from a Binary Black Hole Merger", *Phys. Rev. Lett.* **116,** 61102 (2016).

[4] A. Ashkin, "Acceleration and Trapping of Particles by Radiation Pressure", *Phys. Rev. Lett.* **24,** 156 (1970).

[5] D. Strickland and G. Mourou, "Compression of amplified chirped optical pulses", *Optics Communications* **56,** 219 (1985).

[6] M. H. Anderson, J. R. Ensher, M. R. Matthews, C. E. Wieman, and E. A. Cornell, "Observation of Bose-Einstein Condensation in a Dilute Atomic Vapor", *Science* **269,** 198 (1995).

[7] I. Bloch, J. Dalibard, and W. Zwerger, "Many-body physics with ultracold gases", *Rev. Mod. Phys.* **80,** 885 (2008).

[8] M. R. Andrews, C. G. Townsend, H.-J. Miesner, D. S. Durfee, D. M. Kurn, and W Ketterle, "Observation of Interference Between Two Bose Condensates", *Science* **275,** 637 (1997).

[9] M.-O. Mewes, M. R. Andrews, D. M. Kurn, D. S. Durfee, C. G. Townsend, and W Ketterle, "Output Coupler for Bose-Einstein Condensed Atoms", *Phys. Rev. Lett.* **78,** 582 (1997).

[10] D. M. Stamper-Kurn, H.-J. Miesner, A. P. Chikkatur, S Inouye, J Stenger, and W Ketterle, "Reversible Formation of a Bose-Einstein Condensate", *Phys. Rev. Lett.* **81,** 2194 (1998).

[11] S. Stellmer, B. Pasquiou, R. Grimm, and F. Schreck, "Laser Cooling to Quantum Degeneracy", *Phys. Rev. Lett.* **110,** 263003 (2013).

[12]   J. Hu, A. Urvoy, Z. Vendeiro, V. Crépel, W. Chen, and V. Vuletić, "Creation of a Bose-condensed gas of 87Rb by laser cooling.", *Science* **358**, 1078 (2017).

[13]   A. J. Kerman, V. Vuletić, C. Chin, and S. Chu, "Beyond Optical Molasses: 3D Raman Sideband Cooling of Atomic Cesium to High Phase-Space Density", *Phys. Rev. Lett.* **84**, 439 (2000).

[14]   J Dalibard and C Cohen-Tannoudji, "Laser cooling below the Doppler limit by polarization gradients: simple theoretical models", *J. Opt. Soc. Am. B* **6**, 2023 (1989).

[15]   A. T. Grier, I. Ferrier-Barbut, B. S. Rem, M. Delehaye, L. Khaykovich, F. Chevy, and C. Salomon, "Λ-enhanced sub-Doppler cooling of lithium atoms in D_1 gray molasses", *Phys. Rev. A* **87**, 63411 (2013).

[16]   R. Dum, P. Marte, T. Pellizzari, and P. Zoller, "Laser Cooling to a Single Quantum State in a Trap", *Phys. Rev. Lett.* **73**, 2829 (1994).

[17]   J. I. Cirac, M Lewenstein, and P. Zoller, "Collective laser cooling of trapped atoms", *Eur. Lett.* **35**, 647 (1996).

[18]   G. Morigi, J. I. Cirac, K. Ellinger, and P. Zoller, "Laser cooling of trapped atoms to the ground state: A dark state in position space", *Phys. Rev. A* **57**, 2909 (1998).

[19]   Y. Castin, J. I. Cirac, and M. Lewenstein, "Reabsorption of Light by Trapped Atoms", *Phys. Rev. Lett.* **80**, 5305 (1998).

[20]   L. Santos and M. Lewenstein, "Dynamical cooling of trapped gases. II: Many-atom problem", *Phys. Rev. A* **60**, 3851 (1999).

[21]   K. B. Davis, M. O. Mewes, M. R. Andrews, N. J. van Druten, D. S. Durfee, D. M. Kurn, and W. Ketterle, "Bose-Einstein Condensation in a Gas of Sodium Atoms", *Phys. Rev. Lett.* **75**, 3969 (1995).

[22]   C. C. Bradley, C. A. Sackett, J. J. Tollett, and R. G. Hulet, "Evidence of Bose-Einstein Condensation in an Atomic Gas with Attractive Interactions", *Phys. Rev. Lett.* **75**, 1687 (1995).

[23]   C. S. Adams, H. J. Lee, N. Davidson, M. Kasevich, and S. Chu, "Evaporative Cooling in a Crossed Dipole Trap", *Phys. Rev. Lett.* **74**, 3577 (1995).

[24]   T. Ido, Y. Isoya, and H. Katori, "Optical-dipole trapping of Sr atoms at a high phase-space density", *Phys. Rev. A* **61**, 61403 (2000).

[25] S. Kraft, F. Vogt, O. Appel, F. Riehle, and U. Sterr, "Bose-Einstein Condensation of Alkaline Earth Atoms: ^{40}Ca", *Phys. Rev. Lett.* **103**, 130401 (2009).

[26] M. Lu, N. Q. Burdick, S. H. Youn, and B. L. Lev, "Strongly Dipolar Bose-Einstein Condensate of Dysprosium", *Phys. Rev. Lett.* **107**, 190401 (2011).

[27] K. Aikawa, A. Frisch, M. Mark, S. Baier, A. Rietzler, R. Grimm, and F. Ferlaino, "Bose-Einstein Condensation of Erbium", *Phys. Rev. Lett.* **108**, 210401 (2012).

[28] D.-J. Han, S. Wolf, S. Oliver, C. McCormick, M. T. DePue, and D. S. Weiss, "3D Raman Sideband Cooling of Cesium Atoms at High Density", *Phys. Rev. Lett.* **85**, 724 (2000).

[29] W. Ketterle, D. S. Durfee, and S. D. M. Kurn. "Making, probing and understanding Bose-Einstein condensates", *Bose-Einstein Condensation in Atomic Gases (Proceedings of the International School of Physics "Enrico Fermi," Course CXL)*, ed. by M. Inguscio, S. Stringari, and C. E. Wieman. IOS Press, 1999.

[30] D. Lahaye, T. and Vogels, J. M. and Günter, K. J. and Wang, Z. and Dalibard, J. and Guéry-Odelin, "Realization of a Magnetically Guided Atomic Beam in the Collisional Regime", *Phys. Rev. Lett.* **93**, 93003 (2004).

[31] M. Falkenau, V. V. Volchkov, J. Rührig, A. Griesmaier, and T. Pfau, "Continuous Loading of a Conservative Potential Trap from an Atomic Beam", *Phys. Rev. Lett.* **106**, 163002 (2011).

[32] V. V. Volchkov, J. Rührig, T. Pfau, and A. Griesmaier, "Sisyphus cooling in a continuously loaded trap", *New Journal of Physics* **15**, 093012 (2013).

[33] R. Taïeb, R. Dum, J. I. Cirac, P. Marte, and P. Zoller, "Cooling and localization of atoms in laser-induced potential wells", *Phys. Rev. A* **49**, 4876 (1994).

[34] S. Wu, R. C. Brown, W. D. Phillips, and J. V. Porto, "Pulsed Sisyphus Scheme for Laser Cooling of Atomic (Anti)Hydrogen", *Phys. Rev. Lett.* **106**, 213001 (2011).

[35] K Bongs et al., "The UK National Quantum Technologies Hub in sensors and metrology (Keynote Paper)", ed. by J. Stuhler and A. J. Shields, vol. 9900, International Society for Optics and Photonics, 2016.

[36] E. S. Polzik and H. J. Kimble, "Frequency doubling with $KNbO_3$ in an external cavity", *Opt. Lett.* **16**, 1400 (1991).

[37] L. S. Cruz and F. C. Cruz, "External power-enhancement cavity versus intracavity frequency doubling of Ti:sapphire lasers using BIBO", *Opt. Express* **15**, 11913 (2007).

[38] R. L. Targat, J.-J. Zondy, and P. Lemonde, "75%-Efficiency blue generation from an intracavity PPKTP frequency doubler", *Opt. Commun.* **247**, 471 (2005).

[39] D. Akamatsu, M. Yasuda, T. Kohno, A. Onae, and F.-L. Hong, "A compact light source at 461-nm using a periodically poled $LiNbO_3$ waveguide for strontium magneto-optical trapping", *Opt. Express* **19**, 2046 (2011).

[40] H. Leinen, D. Glässner, H. Metcalf, R. Wynands, D. Haubrich, and D. Meschede, "GaN blue diode lasers: a spectroscopist's view", *Appl. Phys. B* **70**, 567 (2000).

[41] S. Stellmer, "Degenerate quantum gases of strontium dissertation", PhD thesis, Innsbruck: University of Innsbruck, 2012.

[42] T. Nazarova, "Towards the Quantum Noise Limit in Ramsey-Bordé Atom Interferometry", PhD thesis, PTB: Leibniz University Hannover, 2007.

[43] N. Akerman, N. Navon, S. Kotler, Y. Glickman, and R. Ozeri, "Universal gate-set for trapped-ion qubits using a narrow linewidth diode laser", *New J. Phys.* **17** (2015).

[44] A. Thobe, "Ultracold Yb Gases with Control over Spin and Orbital Degrees of Freedom", PhD thesis, Hamburg: University of Hamburg, 2012.

[45] B. J. Reschovsky, B. P. Ruzic, H. Miyake, N. C. Pisenti, P. S. Julienne, and G. K. Campbell, "Narrow-line photoassociation spectroscopy and mass-scaling of bosonic strontium", *arXiv:1808.06507* (2018).

[46] M. Borkowski, R. Ciuryło, P. S. Julienne, M. Yan, B. J. DeSalvo, and T. C. Killian, "Mass scaling and nonadiabatic effects in photoassociation spectroscopy of ultracold strontium atoms", *Phys. Rev. A* **90**, 032713 (2014).

[47] T. Kurosu and F. Shimizu, "Laser Cooling and Trapping of Alkaline Earth Atoms", *Jpn. J. Appl. Phys.* **31**, 908 (1992).

[48] P. G. Mickelson, Y. N. M. de Escobar, P Anzel, B. J. DeSalvo, S. B. Nagel, A. J. Traverso, M Yan, and T. C. Killian, "Repumping and spectroscopy of laser-cooled Sr atoms using the $(5s5p)^3P_2$–$(5s4d)^3D_2$ transition", *J. Phys. B At. Mol. Opt. Phys.* **42**, 235001 (2009).

[49] S. Stellmer and F. Schreck, "Reservoir spectroscopy of $5s5p\ ^3P_2$–$5snd\ ^3D_{1,2,3}$ transitions in strontium", *Phys. Rev. A* **90**, 22512 (2014).

[50] J. E. Sansonetti and G. Nave, "Wavelengths, transition probabilities, and energy levels for the spectrum of neutral strontium (SrI)", *J. Phys. Chem. Ref. Data* **39**, 033103 (2010).

[51] P. Wongwaitayakornkul, "A Tellurium Frequency Reference For Re-pumping During Lasercooling of Strontium", Bachelor's Thesis, Rice University, Texus, USA, 2013.

[52] F. Hu, I. Nosske, L. Couturier, C. Tan, C. Qiao, P. Chen, Y. H. Jiang, and M. Weidemüller, "Analyzing a single-laser repumping scheme for efficient loading of a strontium magneto-optical trap", *Phys. Rev. A (to be published)* (2019).

[53] K. R. Vogel, "Laser Cooling on a narrow atomic transition and measurement of the two-body cold collision loss rate in a strontium magneto-optical trap", PhD thesis, University of Colorado, Boulder, USA, 1999.

[54] Y. Bidel, "Piégeage et refroidissement laser du strontium; Etude de l'effet des interférences en diffusion multiple", PhD thesis, Université de Nice, Nice, France, 2002.

[55] H. G. C. Werij, C. H. Greene, C. E. Theodosiou, and A. Gallagher, "Oscillator strengths and radiative branching ratios in atomic Sr", *Phys. Rev. A* **46**, 1248 (1992).

[56] J. Samland, "Repumping a strontium Zeeman slower", (in press), Master's Thesis, University of Amsterdam, Amsterdam, The Netherlands, 2019.

[57] M. Cooper, Alexandre and Covey, Jacob P. and Madjarov, Ivaylo S. and Porsev, Sergey G. and Safronova, Marianna S. and Endres, "Alkaline-Earth Atoms in Optical Tweezers", *Phys. Rev. X* **8**, 041055 (2018).

[58] R. W. P. Drever, J. L. Hall, F. V. Kowalski, J Hough, G. M. Ford, A. J. Munley, and H. Ward, "Laser phase and frequency stabilization using an optical resonator", *Appl. Phys. B* **31**, 97 (1983).

[59] E. D. Black, "An introduction to Pound–Drever–Hall laser frequency stabilization", *Am. J. Phys.* **69**, 79 (2001).

[60] R. Grimm, M. Weidemüller, and Y. B. Ovchinnikov, "Optical Dipole Traps for Neutral Atoms", *Adv. At., Mol., Opt. Phys.* **42**, 95 (2000).

[61] M. S. Safronova, Z Zuhrianda, U. I. Safronova, and C. W. Clark, "Extracting transition rates from zero-polarizability spectroscopy", *Phys. Rev. A* **92**, 40501 (2015).

[62] M. S. Safronova, S. G. Porsev, U. I. Safronova, M. G. Kozlov, and C. W. Clark, "Blackbody-radiation shift in the Sr optical atomic clock", *Phys. Rev. A* **87**, 12509 (2013).

[63] A. D. Ludlow, "The Strontium Optical Lattice Clock: Optical Spectroscopy with Sub-Hertz Accuracy", PhD thesis, University of Colorado, Boulder, USA, 2008.

[64] S. Bennetts *et al.*, *in preparation*.

[65] S. Schmid, G. Thalhammer, K. Winkler, F. Lang, and J. H. Denschlag, "Long distance transport of ultracold atoms using a 1D optical lattice", *New J. Phys.* **8**, 159 (2006).

[66] J Durnin, J. J. Miceli, and J. H. Eberly, "Comparison of Bessel and Gaussian beams", *Opt. Lett.* **13**, 79 (1988).

[67] Y. Lin, W. Seka, J. H. Eberly, H. Huang, and D. L. Brown, "Experimental investigation of Bessel beam characteristics", *Appl. Opt.* **31**, 2708 (1992).

[68] S. Bennetts, C.-C. Chen, B. Pasquiou, and F. Schreck, "Steady-State Magneto-Optical Trap with 100-Fold Improved Phase-Space Density", *Phys. Rev. Lett.* **119**, 223202 (2017).

[69] A. D. Ludlow, M. M. Boyd, J. Ye, E Peik, and P. O. Schmidt, "Optical atomic clocks", *Rev. Mod. Phys.* **87**, 637 (2015).

[70] A. D. Cronin, J. Schmiedmayer, and D. E. Pritchard, "Optics and interferometry with atoms and molecules", *Rev. Mod. Phys.* **81**, 1051 (2009).

[71] G. J. Dick. "Local oscillator induced instabilities in trapped ion frequency standards", *Proc. Precise Time Time Interval Meet.* Ed. by R. L. Sydnow. U.S. Naval Observatory, Washington, DC, 1987. 133.

[72] P. G. Westergaard, J Lodewyck, and P Lemonde, "Minimizing the dick effect in an optical lattice clock", *IEEE Trans. Ultrason. Ferroelectr. Freq. Control* **57**, 623 (2010).

[73] S. L. Campbell, R. B. Hutson, G. E. Marti, A Goban, N. D. Oppong, R. L. McNally, L Sonderhouse, J. M. Robinson, W Zhang, B. J. Bloom, and J Ye, "A Fermi-degenerate three-dimensional optical lattice clock", *Science* **358**, 90 (2017).

[74] N. P. Robins, P. A. Altin, J. E. Debs, and J. D. Close, "Atom lasers: Production, properties and prospects for precision inertial measurements", *Phys. Rep.* **529**, 637 (2013).

[75] J Chen, "Active optical clock", *Chin. Sci. Bull.* **54**, 348 (2009).

[76] D Meiser, J. Ye, D. R. Carlson, and M. J. Holland, "Prospects for a Millihertz-Linewidth Laser", *Phys. Rev. Lett.* **102**, 163601 (2009).

[77] D Meiser and M. J. Holland, "Steady-state superradiance with alkaline-earth-metal atoms", *Phys. Rev. A* **81**, 33847 (2010).

[78] D. G. Matei, T Legero, S Häfner, C Grebing, R Weyrich, W Zhang, L Sonderhouse, J. M. Robinson, J Ye, F Riehle, and U Sterr, "$1.5\ \mu\mathrm{m}$ Lasers with Sub-10 mHz Linewidth", *Phys. Rev. Lett.* **118**, 263202 (2017).

[79] M. A. Norcia, M. N. Winchester, J. R. K. Cline, and J. K. Thompson, "Superradiance on the millihertz linewidth strontium clock transition", *Sci. Adv.* **2**, e1601231 (2016).

[80] J.-P. Uzan, "The fundamental constants and their variation: observational and theoretical status", *Rev. Mod. Phys.* **75**, 403 (2003).

[81] P. W. Graham, J. M. Hogan, M. A. Kasevich, and S. Rajendran, "New Method for Gravitational Wave Detection with Atomic Sensors", *Phys. Rev. Lett.* **110**, 171102 (2013).

[82] N. Yu and M. Tinto, "Gravitational wave detection with single-laser atom interferometers", *Gen. Relat. Gravit.* **43**, 1943 (2011).

[83] S Kolkowitz, I Pikovski, N Langellier, M. D. Lukin, R. L. Walsworth, and J Ye, "Gravitational wave detection with optical lattice atomic clocks", *Phys. Rev. D* **94**, 124043 (2016).

[84] P. D. Lett, R. N. Watts, C. I. Westbrook, W. D. Phillips, P. L. Gould, and H. J. Metcalf, "Observation of Atoms Laser Cooled below the Doppler Limit", *Phys. Rev. Lett.* **61**, 169 (1988).

[85] G Salomon, L Fouche, P Wang, A Aspect, P Bouyer, and T Bourdel, "Gray-molasses cooling of 39 K to a high phase-space density", *Eur. Lett.* **104**, 63002 (2013).

[86] G. Colzi, G. Durastante, E. Fava, S. Serafini, G. Lamporesi, and G. Ferrari, "Sub-Doppler cooling of sodium atoms in gray molasses", *Phys. Rev. A* **93**, 23421 (2016).

[87] M. Kasevich and S. Chu, "Laser cooling below a photon recoil with three-level atoms", *Phys. Rev. Lett.* **69**, 1741 (1992).

[88] A Aspect, E Arimondo, R Kaiser, N Vansteenkiste, and C Cohen-Tannoudji, "Laser Cooling below the One-Photon Recoil Energy by Velocity-Selective Coherent Population Trapping", *Phys. Rev. Lett.* **61**, 826 (1988).

[89] J. Rührig, T. Bäuerle, A. Griesmaier, and T. Pfau, "High efficiency demagnetization cooling by suppression of light-assisted collisions", *Opt. Express* **23**, 5596 (2015).

[90] S. E. Hamann, D. L. Haycock, G Klose, P. H. Pax, I. H. Deutsch, and P. S. Jessen, "Resolved-Sideband Raman Cooling to the Ground State of an Optical Lattice", *Phys. Rev. Lett.* **80**, 4149 (1998).

[91] C. Y. Yang, P Halder, O Appel, D Hansen, and A Hemmerich, "Continuous loading of $^1S_0$ calcium atoms into an optical dipole trap", *Phys. Rev. A* **76**, 33418 (2007).

[92] N Radwell, G Walker, and S Franke-Arnold, "Cold-atom densities of more than 10^{12} cm^{-3} in a holographically shaped dark spontaneous-force optical trap", *Phys. Rev. A* **88**, 43409 (2013).

[93] H. Katori, T. Ido, Y. Isoya, and M. Kuwata-Gonokami, "Magneto-Optical Trapping and Cooling of Strontium Atoms down to the Photon Recoil Temperature", *Phys. Rev. Lett.* **82**, 1116 (1999).

[94] A. Kawasaki, B. Braverman, Q. Yu, and V. Vuletić, "Two-color magneto-optical trap with small magnetic field for ytterbium", *J. Phys. B* **48**, 155302 (2015).

[95] J. Lee, J. H. Lee, J. Noh, and J. Mun, "Core-shell magneto-optical trap for alkaline-earth-metal-like atoms", *Phys. Rev. A* **91**, 53405 (2015).

[96] J. Grünert and A. Hemmerich, "Sub-Doppler magneto-optical trap for calcium", *Phys. Rev. A* **65**, 41401 (2002).

[97] S. Dörscher, A. Thobe, B. Hundt, A. Kochanke, R. L. Targat, P. Windpassinger, C. Becker, and K. Sengstock, "Creation of quantum-degenerate gases of ytterbium in a compact 2D-/3D-magneto-optical trap setup", *Rev. Sci. Instrum.* **84**, 43109 (2013).

[98] A Frisch, K Aikawa, M Mark, A Rietzler, J Schindler, E Zupanič, R Grimm, and F Ferlaino, "Narrow-line magneto-optical trap for erbium", *Phys. Rev. A* **85**, 51401 (2012).

[99] W. Ketterle, K. B. Davis, M. A. Joffe, A. Martin, and D. E. Pritchard, "High densities of cold atoms in a dark spontaneous-force optical trap", *Phys. Rev. Lett.* **70**, 2253 (1993).

[100] J Mahnke, I Kruse, A Hüper, S Jöllenbeck, W Ertmer, J Arlt, and C Klempt, "A continuously pumped reservoir of ultracold atoms", *J. Phys. B* **48**, 165301 (2015).

[101] A. P. Chikkatur, Y Shin, A. E. Leanhardt, D Kielpinski, E Tsikata, T. L. Gustavson, D. E. Pritchard, and W Ketterle, "A Continuous Source of Bose-Einstein Condensed Atoms", *Science* **296**, 2193 (2002).

[102] N. P. Robins, C Figl, M Jeppesen, G. R. Dennis, and J. D. Close, "A pumped atom laser", *Nat. Phys.* **4**, 731 (2008).

[103] S. Stellmer, M. K. Tey, B. Huang, R. Grimm, and F. Schreck, "Bose-Einstein Condensation of Strontium", *Phys. Rev. Lett.* **103**, 200401 (2009).

[104] R. Senaratne, S. V. Rajagopal, Z. A. Geiger, K. M. Fujiwara, V. Lebedev, and D. M. Weld, "Effusive atomic oven nozzle design using an aligned microcapillary array", *Rev. Sci. Instrum.* **86**, 23105 (2015).

[105] K Dieckmann, R. J. C. Spreeuw, M Weidemüller, and J. T. M. Walraven, "Two-dimensional magneto-optical trap as a source of slow atoms", *Phys. Rev. A* **58**, 3891 (1998).

[106] T. Yang, K. Pandey, M. S. Pramod, F. Leroux, C. C. Kwong, E. Hajiyev, Z. Y. Chia, B. Fang, and D. Wilkowski, "A high flux source of cold strontium atoms", *Eur. Phys. J. D* **69**, 226 (2015).

[107] M. Nosske, Ingo and Couturier, Luc and Hu, Fachao and Tan, Canzhu and Qiao, Chang and Blume, Jan and Jiang, Y. H. and Chen, Peng and Weidemüller, "Two-dimensional magneto-optical trap as a source for cold strontium atoms", *Phys. Rev. A* **96**, 53415 (2017).

[108] M. K. Tey, S. Stellmer, R. Grimm, and F. Schreck, "Double-degenerate Bose-Fermi mixture of strontium", *Phys. Rev. A* **82**, 11608 (2010).

[109] J. V. Prodan, W. D. Phillips, and H. Metcalf, "Laser Production of a Very Slow Monoenergetic Atomic Beam", *Phys. Rev. Lett.* **49**, 1149 (1982).

[110] M Zhu, C. W. Oates, and J. L. Hall, "Continuous high-flux monovelocity atomic beam based on a broadband laser-cooling technique", *Phys. Rev. Lett.* **67**, 46 (1991).

[111] A. J. Berglund, J. L. Hanssen, and J. J. McClelland, "Narrow-Line Magneto-Optical Cooling and Trapping of Strongly Magnetic Atoms", *Phys. Rev. Lett.* **100**, 113002 (2008).

[112] T Kuwamoto, K Honda, Y Takahashi, and T Yabuzaki, "Magneto-optical trapping of Yb atoms using an intercombination transition", *Phys. Rev. A* **60**, R745 (1999).

[113] J. J. McClelland, A. V. Steele, B. Knuffman, K. A. Twedt, A. Schwarzkopf, and T. M. Wilson, "Bright focused ion beam sources based on laser-cooled atoms", *Appl. Phys. Rev.* **3**, 011302 (2016).

[114] A. J. McCulloch, R. W. Speirs, J Grimmel, B. M. Sparkes, D Comparat, and R. E. Scholten, "Field ionization of Rydberg atoms for high-brightness electron and ion beams", *Phys. Rev. A* **95**, 63845 (2017).

[115] L. Hu, N. Poli, L. Salvi, and G. M. Tino, "Atom Interferometry with the Sr Optical Clock Transition", *Phys. Rev. Lett.* **119**, 263601 (2017).

[116] R. H. Parker, C. Yu, W. Zhong, B. Estey, and H. Müller, "Measurement of the fine-structure constant as a test of the Standard Model", *Science* **360**, 191 (2018).

[117] E. Narevicius and M. G. Raizen, "Toward Cold Chemistry with Magnetically Decelerated Supersonic Beams", *Chem. Rev.* **112**, 4879 (2012).

[118] N. Balakrishnan, "Perspective: Ultracold molecules and the dawn of cold controlled chemistry", *The Journal of Chemical Physics* **145**, 150901 (2016).

[119] E. P. Power, L. George, B. Vanderelzen, P. Herrera-Fierro, R. Murphy, S. M. Yalisove, and G. Raithel, "Design and Fabrication of a Chip-based Continuous-wave Atom Laser", *arXiv:1202.0479v1* (2012).

[120] W. D. Phillips and H. Metcalf, "Laser Deceleration of an Atomic Beam", *Phys. Rev. Lett.* **48**, 596 (1982).

[121] G. ten Haaf, T. C. H. de Raadt, G. P. Offermans, J. F. M. van Rens, P. H. A. Mutsaers, E. J. D. Vredenbregt, and S. H. W. Wouters, "Direct Magneto-Optical Compression of an Effusive Atomic Beam for Application in a High-Resolution Focused Ion Beam", *Phys. Rev. Appl.* **7**, 054013 (2017).

[122] A Aghajani-Talesh, M Falkenau, V. V. Volchkov, L. E. Trafford, T Pfau, and A Griesmaier, "Laser cooling of a magnetically guided ultracold atom beam", *New J. Phys.* **12**, 65018 (2010).

[123] G. B. Andresen et al., "Trapped antihydrogen", *Nature* **468**, 673 (2010).

[124] G. Gabrielse et al., "Trapped Antihydrogen in Its Ground State", *Phys. Rev. Lett.* **108**, 113002 (2012).

[125] M. Ahmadi et al., "Observation of the 1S-2S transition in trapped antihydrogen", *Nature* **541**, 506 (2017).

[126] M. Ahmadi et al., "Observation of the hyperfine spectrum of antihydrogen", *Nature* **548**, 66 (2017).

[127] M. Ahmadi et al., "Observation of the 1S-2P Lyman-α transition in antihydrogen", *Nature* **561**, 211 (2018).

[128] N. Masuhara, J. M. Doyle, J. C. Sandberg, D. Kleppner, T. J. Greytak, H. F. Hess, and G. P. Kochanski, "Evaporative Cooling of Spin-Polarized Atomic Hydrogen", *Phys. Rev. Lett.* **61**, 935 (1988).

[129] G. Gabrielse et al., "Lyman-α source for laser cooling antihydrogen", *Opt. Lett.* **43**, 2905 (2018).

[130] K. S. E. Eikema, J. Walz, and T. W. Hänsch, "Continuous Coherent Lyman-α Excitation of Atomic Hydrogen", *Phys. Rev. Lett.* **86**, 5679 (2001).

[131] I. D. Setija, H. G. C. Werij, O. J. Luiten, M. W. Reynolds, T. W. Hijmans, and J. T. M. Walraven, "Optical cooling of atomic hydrogen in a magnetic trap", *Phys. Rev. Lett.* **70**, 2257 (1993).

[132] P. H. Donnan, M. C. Fujiwara, and F. Robicheaux, "A proposal for laser cooling antihydrogen atoms", *J. Phys. B: At., Mol. Opt. Phys.* **46**, 025302 (2013).

[133] V. V. Ivanov and S. Gupta, "Laser-driven Sisyphus cooling in an optical dipole trap", *Phys. Rev. A* **84**, 063417 (2011).

[134] V. V. Ivanov, "Continuous loading of an atom beam into an optical lattice", *Opt. Commun.* **324**, 258 (2014).

[135] L. De Marco, G. Valtolina, K. Matsuda, W. G. Tobias, J. P. Covey, and J. Ye, "A degenerate Fermi gas of polar molecules", *Science* **363**, 853 (2019).

[136] B. K. Stuhl, B. C. Sawyer, D. Wang, and J. Ye, "Magneto-optical Trap for Polar Molecules", *Phys. Rev. Lett.* **101**, 243002 (2008).

[137] T. Isaev and R. Berger, "Polyatomic Candidates for Cooling of Molecules with Lasers from Simple Theoretical Concepts", *Phys. Rev. Lett.* **116**, 063006 (2016).

[138] J. F. Barry, D. J. McCarron, E. B. Norrgard, M. H. Steinecker, and D. DeMille, "Magneto-optical trapping of a diatomic molecule", *Nature* **512**, 286 (2014).

[139] L. Anderegg, B. L. Augenbraun, E. Chae, B. Hemmerling, N. R. Hutzler, A. Ravi, A. Collopy, J. Ye, W. Ketterle, and J. M. Doyle, "Radio Frequency Magneto-Optical Trapping of CaF with High Density", *Phys. Rev. Lett.* **119** (2017).

[140] A. L. Collopy, S. Ding, Y. Wu, I. A. Finneran, L. Anderegg, B. L. Augenbraun, J. M. Doyle, and J. Ye, "3D Magneto-Optical Trap of Yttrium Monoxide", *Phys. Rev. Lett.* **121**, 213201 (2018).

[141] I. Kozyryev, L. Baum, L. Aldridge, P. Yu, E. E. Eyler, and J. M. Doyle, "Coherent Bichromatic Force Deflection of Molecules", *Phys. Rev. Lett.* **120**, 063205 (2018).

[142] S. Truppe, H. J. Williams, M. Hambach, L. Caldwell, N. J. Fitch, E. A. Hinds, B. E. Sauer, and M. R. Tarbutt, "Molecules cooled below the Doppler limit", *Nat. Phys.* **13**, 1173 (2017).

[143] M. S. Safronova, D. Budker, D. DeMille, D. F. J. Kimball, A. Derevianko, and C. W. Clark, "Search for new physics with atoms and molecules", *Rev. Mod. Phys.* **90**, 025008 (2017).

[144] D. DeMille, "Diatomic molecules, a window onto fundamental physics", *Phys. Today* **68**, 34 (2015).

[145] I. Kozyryev and N. R. Hutzler, "Precision Measurement of Time-Reversal Symmetry Violation with Laser-Cooled Polyatomic Molecules", *Phys. Rev. Lett.* **119**, 133002 (2017).

[146] S. K. Tokunaga, C. Stoeffler, F. Auguste, A. Shelkovnikov, C. Daussy, A. Amy-Klein, C. Chardonnet, and B. Darquié, "Probing weak force-induced parity violation by high-resolution mid-infrared molecular spectroscopy", *Mol. Phys.* **111**, 2363 (2013).

[147] S. B. Cahn, J. Ammon, E. Kirilov, Y. V. Gurevich, D. Murphree, R. Paolino, D. A. Rahmlow, M. G. Kozlov, and D. DeMille, "Zeeman-Tuned Rotational Level-Crossing Spectroscopy in a Diatomic Free Radical", *Phys. Rev. Lett.* **112**, 163002 (2014).

[148] J. J. Hudson, D. M. Kara, I. J. Smallman, B. E. Sauer, M. R. Tarbutt, and E. A. Hinds, "Improved measurement of the shape of the electron", *Nature* **473**, 493 (2011).

[149] J. Baron et al., "Order of Magnitude Smaller Limit on the Electric Dipole Moment of the Electron", *Science* **343**, 269 (2013).

[150] W. B. Cairncross, D. N. Gresh, M. Grau, K. C. Cossel, T. S. Roussy, Y. Ni, Y. Zhou, J. Ye, and E. A. Cornell, "Precision Measurement of the Electron's Electric Dipole Moment Using Trapped Molecular Ions", *Phys. Rev. Lett.* **119**, 153001 (2017).

[151] J. Söding, R. Grimm, Y. B. Ovchinnikov, P. Bouyer, and C. Salomon, "Short-Distance Atomic Beam Deceleration with a Stimulated Light Force", *Phys. Rev. Lett.* **78**, 1420 (1997).

[152] X. Miao, E. Wertz, M. G. Cohen, and H. Metcalf, "Strong optical forces from adiabatic rapid passage", *Phys. Rev. A* **75**, 011402 (2007).

[153] M. A. Norcia, J. R. K. Cline, J. P. Bartolotta, M. J. Holland, and J. K. Thompson, "Narrow-line laser cooling by adiabatic transfer", *New J. Phys.* **20**, 023021 (2018).

[154] N. J. Fitch and M. R. Tarbutt, "Principles and Design of a Zeeman-Sisyphus Decelerator for Molecular Beams", *ChemPhysChem* **17**, 3609 (2016).

[155] S. D. Hogan and F. Merkt, "Demonstration of Three-Dimensional Electrostatic Trapping of State-Selected Rydberg Atoms", *Phys. Rev. Lett.* **100**, 043001 (2008).

[156] S. D. Hogan, C. Seiler, and F. Merkt, "Rydberg-State-Enabled Deceleration and Trapping of Cold Molecules", *Phys. Rev. Lett.* **103**, 123001 (2009).

[157] C. Chen *et al.*, *in preparation*.

[158] M. Ben Dahan, E. Peik, J. Reichel, Y. Castin, and C. Salomon, "Bloch Oscillations of Atoms in an Optical Potential", *Phys. Rev. Lett.* **76**, 4508 (1996).

[159] S. R. Wilkinson, C. F. Bharucha, K. W. Madison, Q. Niu, and M. G. Raizen, "Observation of Atomic Wannier-Stark Ladders in an Accelerating Optical Potential", *Phys. Rev. Lett.* **76**, 4512 (1996).

[160] T. P. Dinneen, K. R. Vogel, E. Arimondo, J. L. Hall, and A. Gallagher, "Cold collisions of $Sr^* - Sr$ in a magneto-optical trap", *Phys. Rev. A* **59**, 1216 (1999).

[161] T. Nicholson, S. Campbell, R. Hutson, G. Marti, B. Bloom, R. McNally, W. Zhang, M. Barrett, M. Safronova, G. Strouse, W. Tew, and J. Ye, "Systematic evaluation of an atomic clock at 2×10^{-18} total uncertainty", *Nat. Commun.* **6**, 6896 (2015).

[162] A. D. Bounds, N. C. Jackson, R. K. Hanley, R. Faoro, E. M. Bridge, P. Huillery, and M. P. A. Jones, "Rydberg-Dressed Magneto-optical Trap", *Phys. Rev. Lett.* **120**, 183401 (2018).

[163] B. Battelier, B. Barrett, L. Fouché, L. Chichet, L. Antoni-Micollier, H. Porte, F. Napolitano, J. Lautier, A. Landragin, and P. Bouyer, "Development of compact cold-atom sensors for inertial navigation", ed. by J. Stuhler and A. J. Shields, vol. 9900, International Society for Optics and Photonics, 2016, 990004.

[164] W. F. McGrew, X. Zhang, R. J. Fasano, S. A. Schäffer, K. Beloy, D. Nicolodi, R. C. Brown, N. Hinkley, G. Milani, M. Schioppo, T. H. Yoon, and A. D. Ludlow, "Atomic clock performance enabling geodesy below the centimetre level", *Nature* **564**, 87 (2018).

[165] A. Arvanitaki, P. W. Graham, J. M. Hogan, S. Rajendran, and K. Van Tilburg, "Search for light scalar dark matter with atomic gravitational wave detectors", *Phys. Rev. D* **97**, 75020 (2018).

[166] J. P. Covey, I. S. Madjarov, A. Cooper, and M. Endres, "2000-times repeated imaging of strontium atoms in clock-magic tweezer arrays", *arXiv:1811.06014v3* (2018).

Summary

This thesis describes an experimental setup for expanding the Sr "laser cooling to Bose-Einstein condensate (BEC)" experiment into a steady-state system. The apparatus was designed to explore the possibility of realizing a long-awaited holy grail for ultracold atoms, a steady-state BEC to feed a steady-state atom laser. At the beginning of my thesis, the experiment was started from scratch with an empty table. Four and a half years later we have achieved a steady-state ultracold Sr sample with a unity phase-space density (PSD), of the same order of magnitude as a quantum degenerate gas. Our first attempt to make a steady-state Bose-Einstein condensate was unsuccessful, but from this we have come up with an alternative deceleration scheme in order to load efficiently the reservoir, which so far was the experiment's main bottleneck. We will soon implement this solution in a second attempt to reach steady-state BEC. In the following I summarize the results of my thesis work.

In our work on a steady-state high-PSD magneto-optical trap (MOT), we have demonstrated a proof of principle "atomic marble run" experiment, a cooling architecture in which laser cooling modules employing two different wavelengths are implemented successively. The modules consist of an atomic beam source, a transversal cooling, beam deceleration and trapping. The first module starts with the Sr oven beam source and ends in a 2D broad-line MOT. This MOT feeds the second module, which ends in a narrow-line "capture" MOT. This last MOT is the source of the third and final module, which ends in a steady-state reservoir of atoms. Atoms are continuously decelerated and cooled from a few hundred Kelvin to about $1\,\mu$K. The two cooling transitions (broad-line, blue cooling at 461-nm wavelength and narrow-line, red cooling at 689 nm), which in conventional Sr quantum gas experiments are used in time-sequential cooling steps, are in our machine implemented sequentially in space. In the steady-state "capture" red MOT, we show slowing of an atomic beam with a starting velocity of 6 m/s and followed by trapping in a MOT using the 689-nm intercombination transition with a natural linewidth of 7.4 kHz. In the high-PSD MOT configuration, we demonstrate a steady-state red MOT with a PSD of 10^{-3}, two orders of magnitude better than reported in previous

steady-state MOTs. The experiment illustrates the concept of an "atomic marble run" and shows that it is compatible with future experiments on the creation of a continuously existing quantum degenerate gas and dead-time free atom interferometers or clocks.

In our work on steady-state ultracold Sr near quantum degeneracy, the experiments were carried out by extending the steady-state high-PSD MOT work and adding another cooling module. We realized an ultracold beam with a 10^{-5} PSD, an ideal source for future steady-state superradiant laser applications. We also took a first attempt at expanding the "laser cooling to BEC" experiment into a steady-state experiment. We showed a method that can continuously fill atoms into the reservoir trap of the "laser cooling to BEC" scheme. We achieved a steady-state ultracold Sr sample with a unity phase-space density, only a factor of 2.6 away from steady-state quantum degeneracy. This experiment ultimately was limited by the reservoir temperature.

To circumvent this temperature bottleneck, we developed a new and more efficient method to decelerate the atomic beam in our last cooling step before loading atoms into the reservoir trap. Inspired by a theoretical paper of Peter Zoller from 1994 and a cooling proposal originally formulated for cooling anti-hydrogen, we demonstrated a new deceleration scheme using a Sisyphus cooling mechanism in an optical lattice instead of a radiation pressure force commonly used in laser cooling. The optical lattice induces a periodic ac Stark shift on atoms' excited state, creating a spatially varying potential landscape. Thanks to selective excitation to the lattice potential minimums, an atom loses energy via repeatedly "climbing uphill" through multiple cycles of excitation and spontaneous emission. We characterized the performance of this deceleration method and developed a semi-classical model describing its various working regimes, which depends on the relative magnitude of atoms kinetic energy with respect to the lattice height. Such a method not only provides a new deceleration scheme for our future attempts to reach steady-state BEC, but it can also bring laser cooling to a broad range of atomic and molecular species.

Samenvatting

Dit proefschrift beschrijft de experimentele setup om het Sr "laser koeling naar Bose-Einstein condensaat (BEC)" experiment uit te breiden naar een steady-state systeem. Het apparaat is ontworpen om de mogelijkheid te onderzoeken om een langverwachte heilige graal op het gebied van ultrakoude atomen te realiseren: een steady-state BEC als bron voor een steady-state atoomlaser. Aan het begin van mijn proefschrift zijn we dit experiment gestart uit het niets, op een lege tafel. Vierenhalf jaar later hebben we een steady-state, ultrakoud Sr sample met een faseruimtedichtheid in dezelfde orde van grootte als een ontaard quantumgas. Onze eerste poging om een BEC te genereren bleek niet succesvol. Echter, hierdoor hebben we een alternatief vertragingsschema bedacht om het reservoir efficiënt te vullen, iets wat tot dusver het knelpunt van het experiment was. We zullen deze oplossing spoedig implementeren in een tweede poging om een steady-state BEC te bereiken. In de onderstaande tekst vat ik de resultaten van mijn proefschrift samen.

Gedurende ons werk aan een steady-state magneto-optische val (MOT) met hoge faseruimtedichtheid, demonstreerden we het principe van een "atomische knikkerbaan": een koelingsarchitectuur waarin laserkoelingsmodules met twee verschillende golflengtes achtereenvolgend worden geïmplementeerd. De modules bestaan uit een atomische stralingsbron, transversale koeling, vertraging van de straal, en invanging. De eerste module begint met de stralingsbron uit de Sr oven en eindigt in een 2D brede-lijn MOT. Deze MOT voedt de tweede module, welke eindigt in een smalle-lijn "vang" MOT. Deze laatste MOT is de bron van de derde en laatste module, eindigend in een steady-state reservoir van atomen. Atomen worden continu afgeremd en gekoeld van een paar honderd Kelvin tot ongeveer $1\,\mu$K. De twee koelingstransities (brede-lijn, "blauwe" koeling, bij een golflengte van 461 nm, en smalle-lijn "rode" koeling bij 689 nm, welke worden gebruikt in conventionele Sr quantumgasexperimenten bij achtereenvolgende koelingsstappen in de tijd. In onze machine worden deze achterinvolgend geïmplementeerd in de ruimte. In de steady-state rode "vang" MOT laten we het vertragen van een atomische straal zien, met een startsnelheid van 6 m/s, gevolgd door invanging in een MOT, hierbij

gebruikmakend van de 689 nm intercombinatietransitie met een natuurlijke lijnbreedte van 7,4 kHz. In de MOT-configuratie met hoge faseruimtedichtheid demonstreren we een steady-state rode MOT met een faseruimtedichtheid van 10^{-3}: twee ordes van grootte beter dan beschreven in vorige steady-state MOTs. Het experiment illustreert het concept van een "atomische knikkerbaan" en laat zien dat het compatibel is met toekomstige experimenten waarin continu bestaande ontaarde quantumgassen, evenals atoominterferometers en klokken vrij van dode tijd.

In ons werk aan steady-state, ultrakoud Sr dichtbij quantumontaarding, werden de experimenten uitgevoerd door het werk aan de steady-state MOT met hoge faseruimtedichtheid uit te breiden, en nog een koelingsmodule toe te voegen. We realiseerden een ultrakoude straal met een faseruimtedichtheid van 10^{-5}, een ideale bron van toepassingsmogelijkheden voor toekomstige steady-state superluminiscente lasers. We hebben ook een eerste poging gedaan om het "laserkoeling tot BEC" experiment uit te breiden naar een steady-state experiment. We demonstreren een methode om continu atomen in de reservoirval van het "laserkoeling tot BEC" schema te voeden. Hiermee hebben we een steady-state, ultrakoud Sr sample met een faseruimtedichtheid gelijk aan 1 bereikt, slechts een factor van 2,6 verwijderd van steady-state quantumontaarding. Uiteindelijk bleek dit experiment gelimiteerd door de temperatuur in het reservoir.

Om dit temperatuurknelpunt te omzeilen hebben we een nieuwe en efficiëntere methode ontworpen om de atomische straal af te remmen in onze laatste koelingsstap, voordat de atomen in de reservoirval worden geladen. We demonstreren een nieuw vertragingsschema, geïnspireerd door een theoretisch paper van Peter Zoller uit 1994 en een voorstel voor een koelingsmethode, oorspronkelijk bedoeld om anti-waterstof te koelen. Dit schema maakt gebruik van een Sisyphus koelingsmechanisme in een optisch rooster, in tegenstelling tot stralingsdruk, wat normaliter gebruikt wordt bij laserkoeling. Het optisch rooster induceert een periodieke AC Stark-verschuiving op de geëxciteerde staat van de atomen. Hiermee wordt een ruimtelijk variërend potentieel landschap gecreëerd. Een atoom verliest energie door middel van selectieve excitatie naar de potentiele minima van het rooster, gevolgd door "de heuvel op te klimmen" en dan spontane emissie. Dit proces herhaalt zich in meerdere cycli. We hebben het vermogen van deze vertragingsmethode gekarakteriseerd, en een semiklassiek model ontwikkeld wat de variërende werkregimes hiervan beschrijft. Deze regimes zijn afhankelijk van de relatieve grootte van de kinetische energie van de atomen, relatief tot de hoogte van

het rooster. Een dergelijke methode verschaft niet alleen een nieuw vertragingsschema voor onze toekomstige pogingen om een steady-state BEC te bereiken, maar ook om een grote verscheidenheid aan atomische en moleculaire deeltjes te laserkoelen.

List of publications

Published papers:

- Shayne Bennetts*, **Chun-Chia Chen***, Benjamin Pasquiou, and Florian Schreck, "Steady-State Magneto-Optical Trap with 100-Fold Improved Phase-Space Density", Phys. Rev. Lett. 119, 223202 (2017). *These authors contributed equally to this work.

  Contributions: Designing and implementation of the laser system and optics set-up. Conceiving an idea on characterizing steady-state PSD. Preparation of a high-PSD Sr atomic sample. Taking experimental data.

- Alessio Ciamei, Alex Bayerle, **Chun-Chia Chen**, Benjamin Pasquiou, and Florian Schreck, "Efficient production of long-lived ultracold Sr_2 molecules", Phys. Rev. A 96, 013406 (2017).

  Contributions: Setting up 1064-nm optical lattices.

- Alessio Ciamei, Jacek Szczepkowski, Alex Bayerle, Vincent Barbé, Lukas Reichsöllner, Slava M. Tzanova, **Chun-Chia Chen** , Benjamin Pasquiou, Anna Grochola, Pawel Kowalczyk, Wlodzimierz Jastrzebski and Florian Schreck, "The RbSr $^2\Sigma^+$ ground state investigated via spectroscopy of hot and ultracold molecules", Phys. Chem. Chem. Phys.,
  DOI: 10.1039/C8CP03919D(2018).

  Contributions: Rebuilding and optimizing the RbSr experiment.

Papers submitted for publication:

- **Chun-Chia Chen***, Shayne Bennetts*, Rodrigo González Escudero, Florian Schreck, Benjamin Pasquiou, "Sisyphus Optical Lattice Decelerator",
  preprint:arXiv:1810.07157. *These authors contributed equally to this work.

  Contributions: Implementation of the laser system and optics set-up. Proposing moving lattice for reservoir loading characterization.   Data analysis of

deceleration characterization and atomic beam velocity characterization and lattice height determination. The paper was written by C.C. Chen. and B.P., with input from all authors.

- Oleksiy Onishchenko, Sergey Pyatchenkov, Alexander Urech, **Chun-Chia Chen**, Shayne Bennetts, Georgios A. Siviloglou, Florian Schreck, "The frequency of the ultranarrow $^1S_0$ - $^3P_2$ transition in ^{87}Sr",
  preprint: arXiv:1812.02115.

  Contributions: Setting up 707-nm laser system for $^1S_0$ - $^3P_2$ frequency estimation by reservoir spectroscopy.

Acknowledgments

I vividly remember my parents' and sister's confused faces when I first mentioned the idea of applying for a PhD position in Innsbruck, a place they had never heard of. I will be forever grateful for your unconditional support and a firm belief in me. Thank you.

My passion for Bose-Einstein condensate (BEC) began with my diploma thesis work. For a master student, the idea of manipulating atoms with just light was an exotic concept. When the opportunity arose to build a new all optical Rubidium BEC experiment in Prof. Ming-Shien Chang's group in IAMS, Taiwan I was excited and over the next 18 months I built my first quantum gas machine. I then had 11 months of mandatary military service to think about possible opportunities and challenges to pursue as a PhD student in this field. When I read the paper about "laser cooling Sr to quantum degeneracy", I was immediately attracted to the idea of realizing a steady-state BEC and a steady-state atom laser. Pondering that one day a continuous quantum gas device might exist, I made up my mind that I wanted to be a part of the first prototype experiment and the pioneering development efforts. I still recall the day I sent the e-mail to Florian to ask about the possibility of joining his group. It was a typical one day a week off. I sent the e-mail from an internet café on Kinmen island, the place I served my military service, still wearing my military uniform and so began this journey. We started this adventure towards realizing a prototype steady-state quantum degenerate gas five years ago. Thank you Florian for your vision and efforts to make this project possible. Together with Shayne Bennetts and Benjamin Pasquiou as well as Rodrigo Gonzalez Escudero who later joined the team, we have knocked on the door of a holy grail, a steady-state quantum gas. It took 'blood, sweat and tears' and the full five years to advance the experiment to where it is today. This would never have been possible were it not for the grit and uncompromising determination shared among the team members. If I consider my PhD as a plant in the prospective PhD garden, Florian and Benjamin are both green thumbs. They helped me learn to present my work clearly and professionally. From thesis and paper writing to conference presentations, I benefited greatly from their critical perspectives. Shayne

and I are both workaholics and were easily satisfied by the dubious foods we found at a supermarket near the university. Creativity and inspiration often reached a climax during late nights working on the experiment – along with the consumption of junk food. Shayne and I came up with many experimental tricks which we later implemented on the experiment, tricks that I am still very proud of. From Shayne, I also learnt a lot about lasers. An experimental apparatus is more than just a drawing on a paper, it is a setup in real life. From this perspective, I would also like to thank all the people from the UvA mechanical and electronics workshops for all your help. Without you, our experiment would never have progressed the way it did. I would also thank the administrative staff of the IoP, especially Joost van Mameren and Anne-Marieke Crommentuijn, who helped me so many times over these years.

Looking back over this time, it was quite an adventure with highs and lows. Highs, as Innsbruck is about 600 meters above sea level and a brief trip to Aiguille du Midi near Mont Blanc reached 3842m. Lows, as our lab in Amsterdam is 2 meters below sea level. Moving to Amsterdam was not in my life plan until the day I interviewed for a PhD position in Florian's group in Innsbruck. It was then that Florian mentioned the possibility of moving the strontium team to Amsterdam. Turns out it was a wonderful experience and I would like to thank everyone who took part in my PhD life. I had my first Innsbruck insanely scary mountain hiking experience with Marko and Alex. With Alex, Alessio, and Benjamin, we rebuilt the Rb-Sr mixture machine after moving to Amsterdam. It was then that I learned the nuts and bolts of strontium and also the fact that Dragon ball is also famous in Italy. Arthur, Carla, Natalie, Graham, Vincent, David, Severin, Lukas and Rodrigo helped me check off my bucket list by experiencing Amsterdam city life and enjoying afternoon coffee breaks. I enjoyed lovely day long weekend cycling trips across the Netherlands' cycling routes with Shayne and Sergey. I also enjoyed presenting our work to Georgios's two years old son, and getting the request to help him to build a cold-atom experiment in the near future. Chia-Ching, who joined the neighbouring lab in 2016, helped start a tradition of exploring Chinese restaurants across Amsterdam with friends and colleagues. Thank you Denis, Alex Urech and Oleksiy for being nice officemates, especially Denis for the good balcony chats during my thesis writing phase. Thank you Henning, Julius, Andira, Pound, Tim, Arthur, Cesar, and Bo for good times in Barcelona during the ICAP conference. Thank you Cheng-An, Fu-Yuan for the hospitality during my DAMOP conference in the US.

I dedicate this thesis to my family and friends from IAMS.